Measurement of the Proton Structure Function F_2 at low x and low Q^2 with the H1 Detector at HERA

Von der Fakultät für Mathematik, Informatik und Naturwissenschaften
der Rheinisch-Westfälischen Technischen Hochschule Aachen
zur Erlangung des akademischen Grades eines Doktors
der Naturwissenschaften genehmigte Dissertation

vorgelegt von

Diplom-Physiker
Carlo Duprel

aus Ernster, Luxemburg

Berichter: Universitätsprofessor Dr. G. Flügge
Universitätsprofessor Dr. Ch. Berger

Tag der mündlichen Prüfung: 07.03.2003

Abstract

A measurement of the proton structure function $F_2(x,Q^2)$ with four-momentum transfer squared Q^2 between 0.08 GeV^2 and 0.35 GeV^2 and with Bjorken x in the range of $1.2 \cdot 10^{-6} < x < 5.8 \cdot 10^{-5}$ is presented. The analysis is based on data recorded in the end of 1999 by the H1 detector at the HERA ep collider with a center-of-mass energy $\sqrt{s} = 318$ GeV^2. A detailed description of the measurement of inclusive cross sections is given. Special emphasis will be placed on the understanding of the performance of the VLQ spectrometer which covers the kinematic range of low Q^2 in the H1 experiment.

Kurzfassung

Die Messung der Proton-Strukturfunktion $F_2(x,Q^2)$ für Werte des negativen Vierer-Impuls-Übertragsquadrates Q^2 zwischen 0.08 GeV^2 und 0.35 GeV^2 und Bjorken-x im Bereich $1.2 \cdot 10^{-6} < x < 5.8 \cdot 10^{-5}$ wird präsentiert. Die Analyse basiert auf einem Datensatz, der Ende 1999 mit dem H1-Detektor am HERA ep-Speicherring mit einer Schwerpunktsenergie von $\sqrt{s} = 318$ GeV^2 aufgenommen wurde. Eine detaillierte Beschreibung der Messung von inklusiven Wirkungsquerschnitten wird vorgestellt. Ein Schwerpunkt der Arbeit bilden die Studien zum Verständnis des VLQ-Spektrometers, das den kinematischen Bereich kleiner Werte von Q^2 im H1-Experiment abdeckt.

Kuerzfaassong

D'Miessung vun der Proton Structurfunctioun $F_2(x,Q^2)$ fir Wäerter vum negativen Veierer-Impuls-Transfer Q^2 zwëschen 0.08 GeV^2 an 0.35 GeV^2 an Bjorken-x am Beraich $1.2 \cdot 10^{-6} < x < 5.8 \cdot 10^{-5}$ gët prësentéiert. D'Analyse baséiert op Donnéen déi um Än vun 1999 mat dem H1 Detector um HERA ep-Spaicherrénk mat enger Energie vun $\sqrt{s} = 318$ GeV^2 opgehol gi sin. Eng détailléiert Beschreiwung vun der Miessung vum inclusiven Wiërkungsquerschnëtt gët viergestallt. Ee Schwéierpunkt vun der Aarbecht ass d'Verständnis vun der Performanz vum VLQ-Spectrometer, daat den kinematischen Beraich vu klenge Wäerter vu Q^2 am H1 Experiment ofdeckt.

Contents

Introduction

In the second half of the last century the 'Standard Model' of particle physics was developed and confirmed in numerous experiments. This theory is based on a rather simple picture. Matter is composed of fundamental spin-$\frac{1}{2}$ particles (fermions): quarks and leptons as well as the corresponding anti-particles. Interactions of these constituents are due to three fundamental forces[1]: the electromagnetic, the weak and the strong interaction. The carriers of these interactions are the following bosons (spin-1 particles): γ, $W^{\pm}$, Z^0 and 8 gluons. Whereas the electromagnetic force accounts for most extra-nuclear phenomena and the weak interaction is the fundamental force underlying the β-decay of nuclei, the strong interaction is the binding force between quarks inside protons and also between neutrons and protons inside nuclei.

Since the 1960's deep-inelastic scattering experiments are the predominant tool to investigate the structure of the proton and the fundamental forces underlying the dynamics of the constituents inside the proton. In the long tradition of DIS experiments, the HERA collider allows to explore ep scattering processes with higher resolution power due to the much larger lepton-proton center of mass energy ($\sqrt{s} = 318$ GeV) compared to previous fixed target experiments ($\sqrt{s} \leq 40$ GeV). The multi-purpose detectors H1 and ZEUS at HERA extend the kinematic coverage in the measurement of the inclusive electron-proton scattering cross section to low x and high Q^2. From these measurements the proton structure function F_2 may be extracted assuming the longitudinal structure function F_L. In QCD analyses combining the measured structure functions with results from fixed target experiments, the coupling constant of the strong interaction α_s and the individual parton density functions may be determined.

H1 has published measurements of the proton structure function over a large kinematic range. In the deep-inelastic scattering regime [1] [2] electron-proton cross sections may be predicted based on perturbation theory. On the other hand in the calculation of inclusive cross sections in the photoproduction region one relies on non-perturbative models [3]. The investigation of the transition region between perturbative and non-perturbative concepts and the comparison to existing phenomenological models is of fundamental theoretical interest. Measurements of the proton structure function F_2 in the region of very low Q^2 were

[1] The fourth fundamental interaction, gravity, is negligible on the scales of mass and distance involved in particle physics at present collider experiments.

published by the ZEUS collaboration [4],[5].

The H1 collaboration decided in 1996 to modify the existing experiment to increase the kinematic acceptance in the transition region. Finally in 1998 the VLQ spectrometer was installed in the backward region of the H1 detector which provided a coverage of the kinematic region $0.08\ \mathrm{GeV}^2 < Q^2 < 0.35\ \mathrm{GeV}^2$. After a successful commissioning of the new detector components, a large data set with an integrated luminosity of $\mathcal{L}_{\mathrm{int}} \approx 1\ \mathrm{pb}^{-1}$ was recorded in the end of 1999. This data sample constitutes the basis in the measurement of the proton structure function F_2 in the low Q^2 region presented in this thesis. The data taking of the VLQ spectrometer ended with the removal of the detector components in the luminosity upgrade in 2000.

The aim of this thesis is to extend the measurement of the proton structure function $F_2(x,Q^2)$ by the H1 experiment to the low Q^2 region. The experimental device, the VLQ spectrometer, will be presented and the efficiency, calibration and alignment of the detector components will be discussed in detail. The double differential inclusive electron-proton cross section is measured in the kinematic regime covered by the VLQ spectrometer ($0.08\ \mathrm{GeV}^2 < Q^2 < 0.35\ \mathrm{GeV}^2$ and $1.2 \cdot 10^{-6} < x < 5.8 \cdot 10^{-5}$) and the proton structure function F_2 is extracted.

In the first chapter of this thesis a short theoretical overview of inelastic electron-proton scattering is given. Theoretical concepts applicable in the transition region, such as the Vector Dominance Model and Regge Theory, are briefly discussed.

In the second chapter the HERA collider and the H1 experiment will be described. Special emphasis will be placed on the configuration of the VLQ spectrometer. The last section of this chapter is devoted to the reconstruction of the kinematic variables.

Chapter 3 introduces the Monte Carlo event generators used in this analysis.

In the first part of chapter 4 the performance of the VLQ tracking device will be outlined. Thereafter the calibration and the alignment of the VLQ calorimeters will be described.

The fifth chapter is concerned with the determination of the inclusive VLQ trigger efficiencies. Subsequently the efficiencies of the vertex reconstruction will be outlined.

The data sample underlying the detector studies and the measurement of the proton structure function F_2 will be presented in the first part of chapter 6. Subsequently the selection criteria applied to the data and the Monte Carlo sample, including the rejection of background, will be discussed.

In the seventh chapter the method used in the determination of the proton structure function F_2 will be introduced. The bin selection based on purity and stability studies will be outlined. The good description of several observables by the Monte Carlo is the basis of the unfolding of the data and subsequently the influence of radiative corrections will be investigated. Finally the result of the measurement including systematic uncertainties will be presented and discussed in comparison to previous experimental results and theoretical predictions.

1

Theoretical Overview

In this chapter a short overview of the theoretical concepts underlying the measurement of the proton structure function F_2 is given. After the introduction to HERA kinematics, the relation between cross sections and structure functions is explained. A physical interpretation of the structure functions in the Quark Parton Model and in Quantum Chromodynamics is given. Finally several models applicable in the transition region between deep-inelastic scattering and photoproduction are presented. In the following the natural system of units, i.e. $\hbar = 1$ and $c = 1$, will be used.

1.1 Kinematics of Electron-Proton Scattering

Two interaction types contribute to the scattering of electrons on protons at HERA: neutral current interactions (NC, $ep \to eX$, see figure 1.1 left) where the exchanged virtual boson is a neutral particle (γ or Z^0) and charged current interactions (CC, $ep \to \nu X$, see figure 1.1 right) where the virtual boson is a charged particle (W^+ or W^-) and the outgoing lepton is a neutrino. The kinematics of an ep scattering process on Born level are given by the following three Lorentz-invariant variables:

$$
\begin{aligned}
Q^2 &= -q^2 = -(l - l')^2 \\
x &= \frac{Q^2}{2k \cdot q} \qquad 0 \leq x \leq 1 \\
y &= \frac{k \cdot q}{k \cdot l} \qquad 0 \leq y \leq 1
\end{aligned}
\tag{1.1}
$$

where l and l' denote the four-momenta of the ingoing and outgoing lepton and k the four-momentum of the incoming proton. k' represents the four-momentum of the hadronic final state X. Q^2 defined as the negative square of the momentum transfer q is the virtuality of the exchanged boson. x is called the Bjorken scaling variable and represents the proton momentum fraction carried by the struck quark in the infinite momentum frame of the

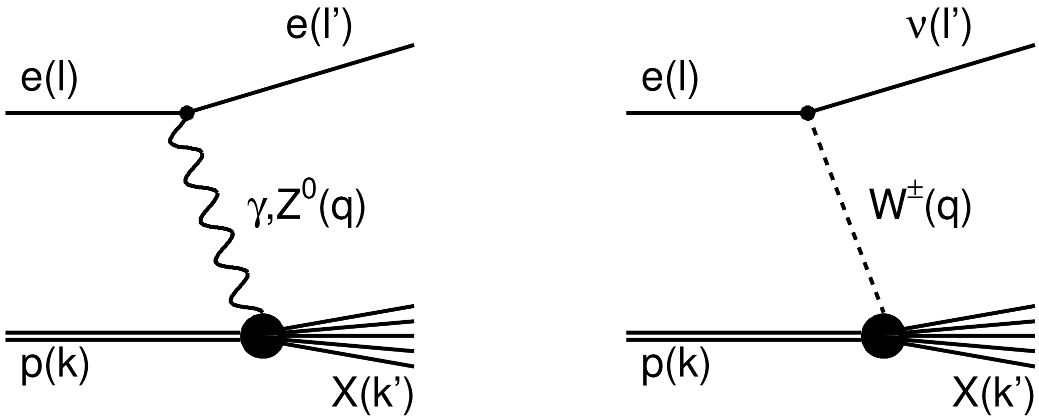

Figure 1.1: *Diagram of the Born process in deep-inelastic ep scattering for the neutral current process (left) and charged current process (right).*

proton. The inelasticity y denotes the fraction of the electron energy carried by the exchanged gauge boson in the proton rest frame. The square of the center-of-mass energy s of the ep system[1] and the square of the invariant mass of the hadronic final state system W^2 are given by the following relation:

$$\begin{aligned} s &= (k+l)^2 \\ W^2 &= (k+q)^2 \end{aligned} \tag{1.2}$$

Neglecting the masses of the electron and the proton the following relations are obtained:

$$Q^2 = sxy \qquad\qquad W^2 = Q^2\,\frac{1-x}{x} \tag{1.3}$$

Thus in the case of fixed center-of-mass energy $\sqrt{s}$ only two of the kinematic variables Q^2, y, W^2 and x are independent. Several methods for the reconstruction of the kinematic variables will be presented in section 2.3.

1.2 Cross Sections and Structure Functions

In this section the relation between cross sections and structure functions will be presented. One determines the inelastic[2] ep cross section differentially in two variables, as only two of the kinematic variables Q^2, y, W^2 and x are independent. At moderate and high Q^2 inclusive

[1] With the beam energies $E_0 = 27.5$ GeV and $E_p = 920$ GeV at HERA, one obtains for the center-of-mass energy $\sqrt{s} = \sqrt{4E_eE_p} \approx 318$ GeV.

[2] An elastic ep scattering process is determined by $x = 1$ and thus $W^2 = M^2$ with M the mass of the proton. Accordingly inelastic scattering is defined by $W^2 > M^2$.

cross sections are usually determined differentially in Q^2 and x. The double differential cross section for inelastic ep scattering can be parameterized in the following functional form [6]:

$$\frac{d^2\sigma^{ep}}{dxdQ^2} \propto \sum_j \epsilon_j L^j_{\mu\nu} W^{\mu\nu}_j \tag{1.4}$$

where j denotes the different contributions: $j = \gamma, Z^0, \gamma Z^0$ for neutral current and $j = W^{\pm}$ for charged current processes[3]. The couplings of the exchanged boson to the particles involved in the scattering process are given by ϵ_j while $L^j_{\mu\nu}$ resp. $W^{\mu\nu}_j$ represent the leptonic resp. hadronic tensor. Whereas the leptonic tensor is calculable in QED, the hadronic tensor which encodes the structure of the proton cannot be calculated at present. Basing on the most general Lorentz-invariant ansatz for $W^{\mu\nu}_j$ and considering certain restrictions, e.g. current conservation, the double differential cross section for unpolarized ep scattering in the NC process is given as follows:

$$\frac{d^2\sigma^{e^\pm p}}{dxdQ^2} = \frac{4\pi\alpha^2}{xQ^4}\left[\frac{1}{2}(1+(1-y)^2)\tilde{F}_2^{NC}(x,Q^2) - \frac{y^2}{2}\tilde{F}_L^{NC}(x,Q^2) \mp (y-\frac{y^2}{2})x\tilde{F}_3^{NC}(x,Q^2)\right] \tag{1.5}$$

where α is the electromagnetic fine structure constant. The generalized structure functions $\tilde{F}_2^{NC}$, $\tilde{F}_L^{NC}$ and $x\tilde{F}_3^{NC}$ are composed of the following structure functions which encode the contributions from the different electroweak gauge bosons:

$$\tilde{F}_2^{NC} = \eta_\gamma F_2^\gamma - g_V \eta_{\gamma Z} F_2^{\gamma Z} + (g_V^2 + g_A^2)\eta_Z F_2^Z \tag{1.6}$$
$$\tilde{F}_L^{NC} = \eta_\gamma F_L^\gamma - g_V \eta_{\gamma Z} F_L^{\gamma Z} + (g_V^2 + g_A^2)\eta_Z F_L^Z \tag{1.7}$$
$$x\tilde{F}_3^{NC} = -g_A \eta_{\gamma Z} x F_3^{\gamma Z} + 2 g_V g_A \eta_Z x F_3^Z \tag{1.8}$$

The structure functions $F^\gamma_{2,L}$ encode the pure γ-exchange, $F^{\gamma Z}_{2,L}$ and $xF_3^{\gamma Z}$ arise due to the γZ interference and $F^Z_{2,L}$ and xF_3^Z due to pure Z-exchange. $F_L(x,Q^2)$ represents the longitudinal structure function while g_V and g_A denote the vector- and axial-vector-couplings of the electron. The corresponding couplings η_γ, $\eta_{\gamma Z}$ and η_Z are defined as follows:

$$\eta_\gamma = 1 \qquad \eta_{\gamma Z} = \frac{G_F M_Z^2}{2\sqrt{2}\pi\alpha}\frac{Q^2}{Q^2+M_Z^2} \qquad \eta_Z = \eta^2_{\gamma Z} \tag{1.9}$$

with G_F the Fermi constant and M_Z the mass of the Z boson.

At low Q^2 ($Q^2 \ll M_Z^2$), the contributions from $F^{\gamma Z}_{2,3,L}$ and $F^Z_{2,3,L}$ are small compared to the contribution from pure γ exchange due to the $Q^2/(Q^2+M^2_{Z,W})$ term in the coupling and will therefore be neglected from now on. The double differential cross sections in Q^2 and x for unpolarized ep scattering in the region of low Q^2 is then expressed by the following relation to the electromagnetic structure function $F_2(x,Q^2)$[4]:

$$\frac{d\sigma^{ep}}{dxdQ^2} = \frac{2\pi\alpha^2}{xQ^4}\left[2(1-y) + \frac{y^2}{1+R}\right] F_2(x,Q^2) \tag{1.10}$$

[3] $j = W^-$ for e^-p scattering and $j = W^+$ for e^+p scattering.

[4] In the following the index γ will be omitted.

with $R = \sigma_L/\sigma_T = F_L/(F_2 - F_L)$ defined as the ratio of the longitudinal to the transverse cross section. The longitudinal structure function is given as follows: $F_L(x,Q^2) = F_2(x,Q^2) - 2xF_1(x,Q^2)$. Double differentially in Q^2 and y the cross section reads:

$$\frac{d^2\sigma^{ep}}{dydQ^2} = \frac{2\pi\alpha^2}{yQ^4}\left[2(1-y) + \frac{y^2}{1+R}\right] F_2(x,Q^2) \tag{1.11}$$

1.3 Virtual Photon-Proton Scattering

In the region of medium and high Q^2 it is widely spread to determine the inelastic *ep* cross section in terms of structure functions depending on the kinematic variables Q^2 and x (see previous section). There exists an equivalent interpretation of the inelastic *ep* scattering cross section, which can be viewed as an absorption by the proton of virtual photons, emitted by the electron [7]:

$$\gamma^*\, p \to X \tag{1.12}$$

The cross section for *ep* scattering is then intuitively given by:

$$\frac{d^2\sigma^{ep}}{dydQ^2} = \Gamma_t\sigma_t(Q^2,W^2) + \Gamma_l\sigma_l(Q^2,W^2) \tag{1.13}$$

$$= \Gamma_t\left[\sigma_t(Q^2,W^2) + \epsilon(y)\,\sigma_l(Q^2,W^2)\right] \tag{1.14}$$

where $\Gamma_t dQ^2dy$ represents the number of transversely polarized photons emitted by the electron in the kinematic interval dQ^2dy and $\Gamma_l dQ^2dy$ defined accordingly for longitudinally polarized photons. $\sigma_t(Q^2,W^2)$ and $\sigma_l(Q^2,W^2)$ are the corresponding transverse and longitudinal γ-absorption cross sections. The photon polarization $\epsilon(y) := \Gamma_l/\Gamma_t$ is given by the ratio of the longitudinal to the transverse photon flux. With the following definitions of the structure functions $F_{1,2,L}$ [7]:

$$2xF_1 := \frac{Q^2}{4\pi^2\alpha}\sigma_t \qquad F_2 := \frac{Q^2}{4\pi^2\alpha}(\sigma_t + \sigma_l) \qquad F_L := \frac{Q^2}{4\pi^2\alpha}\sigma_l \tag{1.15}$$

one may conclude with 1.11 and 1.14:

$$\Gamma_t(y,Q^2) \equiv \frac{1}{\epsilon(y)}\Gamma_l(y,Q^2) = \frac{\alpha}{2\pi Q^2 y}(1+(1-y)^2) \qquad \epsilon(y) := \frac{\Gamma_l}{\Gamma_t} = \frac{2(1-y)}{1+(1-y)^2} \tag{1.16}$$

The total virtual photon-proton cross section $\sigma_{tot}^{\gamma^*p}$ is then given by 1.15:

$$\sigma_{tot}^{\gamma^*p} = \sigma_t + \sigma_l \tag{1.17}$$

$$= \frac{4\pi\alpha^2}{Q^2}F_2(x,Q^2) \tag{1.18}$$

In the framework of virtual photon-proton scattering the transition from regions of moderate and high Q^2 to the region of photoproduction $Q^2 \approx 0$ GeV^2 is possible. In the limit $Q^2 \to 0$ the photon absorbed by the proton is real and the corresponding process is given by:

$$\gamma\, p \to X$$

For this process σ_l vanishes because real photons are only transversely polarized and the transverse cross section σ_t converges to the photoproduction cross section $\sigma^{\gamma p}(W^2)$. In the photoproduction region cross sections are commonly measured in dependence of the kinematic variable W^2. Considering $W^2 = ys$ it is possible to determine the photoproduction cross section in dependence of y. Additionally if one neglects the Q^2 dependence of the transverse cross section $\sigma_t(Q^2, y) \to \sigma_t(y)$ (the so-called Weizsäcker-Williams approximation) the photoproduction cross section in ep scattering is obtained by integrating 1.14 over Q^2:

$$\frac{d\sigma^{ep}}{dy} = \sigma^{\gamma p}(y) \cdot f_{\gamma/e} \qquad (1.19)$$

with $f_{\gamma/e}$ the flux factor, which describes the energy spectrum of the photons emitted by the electron.

The structure functions $F_{1,2,L}$ parameterize the structure of the proton. The physical interpretation of these functions is e.g. possible in the framework of a model of the constituents and the interacting forces inside the proton. The Quark Parton Model and the theory of Quantum Chromodynamics are shortly presented in the following sections.

1.4 Quark Parton Model

The Quark Parton Model (QPM), developed in the 1960's, delivered the first description of the structure of protons and other hadrons. In this model the proton consists of free pointlike spin 1/2 particles.

One of the basic concepts of the QPM is that the ep interaction can be viewed as incoherent scattering of electrons off partons inside the proton. This assumption can be justified by the following short argument. The interaction time t of the probe with the constituents of the proton is inversely proportional to its virtuality Q^2 ($t \propto 1/\sqrt{Q^2}$). Thus at large enough Q^2 the interaction time of the scattering process is much smaller than the lifetime of the fluctuations inside the proton. Therefore the probe sees free (non-self-interacting) constituents of the proton (the so-called partons) and the ep cross section can be formulated as the incoherent sum of elastic electron parton scattering. Introducing the quark density

$q_f(x)$ one obtains the following interpretation of the structure functions:

$$F_1(x) = \frac{1}{2}\sum_f e_f^2 \left(q_f(x) + \bar{q}_f(x)\right) \tag{1.20}$$

$$F_2(x) = \sum_f e_f^2 x \left(q_f(x) + \bar{q}_f(x)\right) \tag{1.21}$$

$$2xF_1(x) = F_2(x) \tag{1.22}$$

The term $q_f(x)dx$ gives the probability of finding a quark q with flavour f and momentum fraction between x and $x + dx$ inside the proton. e_f is the charge of the quark in units of electron charge. By measuring the inelastic ep cross section one is able to determine the structure functions which are interpreted in the QPM in terms of the sum of quark and anti-quark densities inside the proton (equations 1.10 and 1.21).

The relation between $F_1(x)$ and $F_2(x)$ (equation 1.22) is called Callan-Gross relation [8] and implies that $F_L = F_2 - 2xF_1 \equiv 0$. Therefore according to 1.15 the longitudinal cross section σ_L vanishes. This is a consequence of the Parton Model ansatz treating the partons as spin 1/2 particles which are therefore only able to couple to transversely polarized photons.

Further consequences of the Parton Model may be justified by the following argumentation. A probe resolves objects of size Δ, if the wavelength λ of the probe fulfills the following condition:

$$\lambda \propto \frac{1}{\sqrt{Q^2}} \leq \Delta \tag{1.23}$$

If the particles within the proton are indeed pointlike, one would expect the structure of the proton to be independent of the resolution power of the probe and thus on Q^2. This leads to the fact that the above quark densities and structure functions only depend on the kinematic variable x and not on Q^2. This behaviour is known as Bjorken scaling. At fixed x the scaling behaviour leads to a $1/Q^4$ dependence of the inelastic cross section (see equation 1.10). Therefore the inelastic cross section strongly dominates with increasing Q^2 over the elastic cross section which varies with $1/Q^{12}$ [7]. Accordingly ep scattering at high Q^2 ($Q^2 > 5$ GeV^2) is called deep-inelastic scattering (DIS).

Although the experimental observation at SLAC of the Bjorken scaling behaviour and of the Callan-Gross relation in the late 1960's confirmed the Quark Parton Model, contradictions soon arose. If the proton were solely to be constituted of charged quarks, the integration of the parton densities over all partons inside the proton and over the whole kinematic range of x should be equal to unity:

$$\int_0^1 dx\, x \sum_f q_f(x) = 1 \tag{1.24}$$

As the experimental value turned out to be ≈ 0.5 [9], it was concluded that half of the proton momentum was carried by neutral particles. These particles were identified as gluons and directly observed in 3-jet events at PETRA in 1979. Additionally the Quark Parton Model does not predict several other experimental results i.e. quark confinement, logarithmic violation of the scaling behaviour, etc.

1.5 Quantum Chromodynamics

In the 1970's the naive Quark Parton Model was replaced by the field theory of strong interaction, the theory of Quantum Chromodynamics (QCD). QCD is a local non-Abelian gauge theory, based on the $SU(3)$ gauge group. The charge of the strong interaction is a new quantum number called colour with three degrees of freedom (red (r), green (g) and blue (b) and the corresponding anti-colours). Each quark carries, besides its electric and weak charge, a colour charge. The gauge bosons of the strong interactions are eight gluons with no electric charge. As a consequence of the non-Abelian nature of QCD gluons carry colour charge and are therefore able to self-interact, producing three-gluon as well as four-gluon vertices[5]. The coupling constant of the strong interaction α_s depends on the scale (i.e. Q^2) at which the interaction occurs. At small distances (large Q^2) the coupling becomes small and the quarks inside a proton can be treated as quasi-free particles. This behaviour is called 'asymptotic freedom'. However at large distances (low Q^2) the coupling between quarks and gluons becomes large. Therefore quarks and gluons do not appear as free particles but only in colourless hadronic bound states. This behaviour is known as 'colour-confinement'.

Whereas in the Quark Parton Model quarks were the only constituents of the proton, the appearance of gluons in QCD leads to a fundamental change of dynamics inside the proton. The radiation of gluons allows the coupling of quarks to longitudinally polarized photons and therefore the longitudinal cross section can not be neglected anymore ($\sigma_L > 0$). Thus the Callan-Gross relation is violated. Additionally the radiation of gluons results in a violation of the scaling behaviour with a logarithmic dependence on Q^2 which is also experimentally observed. The quarks inside the proton radiate gluons, each gluon can then split into a $q\bar{q}$-pair which themselves radiate gluons with a smaller momentum fraction x and so on. Besides the three valence quarks, the proton consists of gluons and a sea of quarks. The gluons and the sea quarks mainly increase the parton densities at low values of x. Therefore the structure function F_2 rises at low values of x with increasing Q^2 (due to the higher number of radiated gluons) and decreases slightly at high values of x with increasing Q^2. At fixed values of Q^2 F_2 rises with decreasing x due to the increasing parton densities.

In the framework of QCD the concept of factorization allows for the separation of short-distance and long-distance processes. For the calculation of an inclusive ep-scattering cross section this implies that the interaction consists of two components. A short-distance process ($\alpha_s \ll 1$) which describes the interaction between a photon and a quark of momentum

[5]The gauge bosons in Quantum Electrodynamics do not carry electric charge and thus do not couple to themselves.

fraction x and is calculable in perturbative QCD. A long-distance process ($\alpha_s \geq 1$) which encodes the dynamics of the partons inside the proton. As perturbation theory is no longer applicable in this regime, the momentum distribution of partons inside the proton can not be calculated from first principles. Instead one introduces parameterized functions, the parton-density functions, $q_f(x)$ which give the probability of finding a parton f inside the proton carrying fractional momentum x. The free parameters of these functions are then determined by fitting to a large number of experimental results. The factorization procedure introduces a new scale called factorization scale μ_F at which short-distance and long-distance processes are separated. QCD-factorization also allows for the absorption of collinear divergences (which occur from the radiation of gluons with vanishing transverse momentum $k_\perp$ relative to the initial parton) by a redefinition of the parton density functions according to a certain 'scheme'. Requiring that any physical observable is independent of the factorization scale μ_F one obtains the Dokshitzer-Gribov-Lipatov-Altarelli-Parisi (DGLAP) evolution equations [10, 11], a set of coupled integro-differential equations which describe the evolution of the parton density functions with μ_F. A common choice for the factorization scale is $\mu_F = Q^2$. Knowing the parton density functions $q_f(x, \mu_F)$ at a certain scale $\mu_F = Q_0^2$ within the range of applicability of perturbative QCD, the DGLAP equations allow then to evolve these functions to higher values of Q^2.

The relation between the structure function F_2 and the quark densities is given by the following expression:

$$F_2(x, Q^2) = x \sum_f e_f^2 \left(q_f(x, Q^2) + \bar{q}_f(x, Q^2)\right) \tag{1.25}$$

where the sum runs over all quark flavours f, corresponding to equation 1.21.

Figure 1.2 shows the measurement of the proton structure function F_2 obtained by measurements of the H1 collaboration [12], along with measurements from various fixed target experiments (SLAC, NMC and BCDMS). Also shown are measurements from various fixed target experiments. The curve represents a next-to-leading order QCD fit to these data. The violation of the Bjorken scaling behaviour predicted by QCD is visible.

1.6 Transition Region

The kinematic region of inclusive *ep* scattering may be divided into two regimes. In the region of high virtuality of the exchanged gauge boson ($Q^2 > 1-5$ GeV^2) where perturbative QCD is applicable (deep-inelastic scattering (DIS)) and in the region of vanishing $Q^2 \approx 0$ GeV^2 called the photoproduction regime. In this region the relevant scale $\mu = Q^2$ is low and most processes contributing to the total inclusive cross section are not calculable in perturbation theory, due to the large value of the expansion parameter $\alpha_s(\mu) \approx 1$. In order to investigate the photoproduction region an ansatz for the structure functions and the total cross section

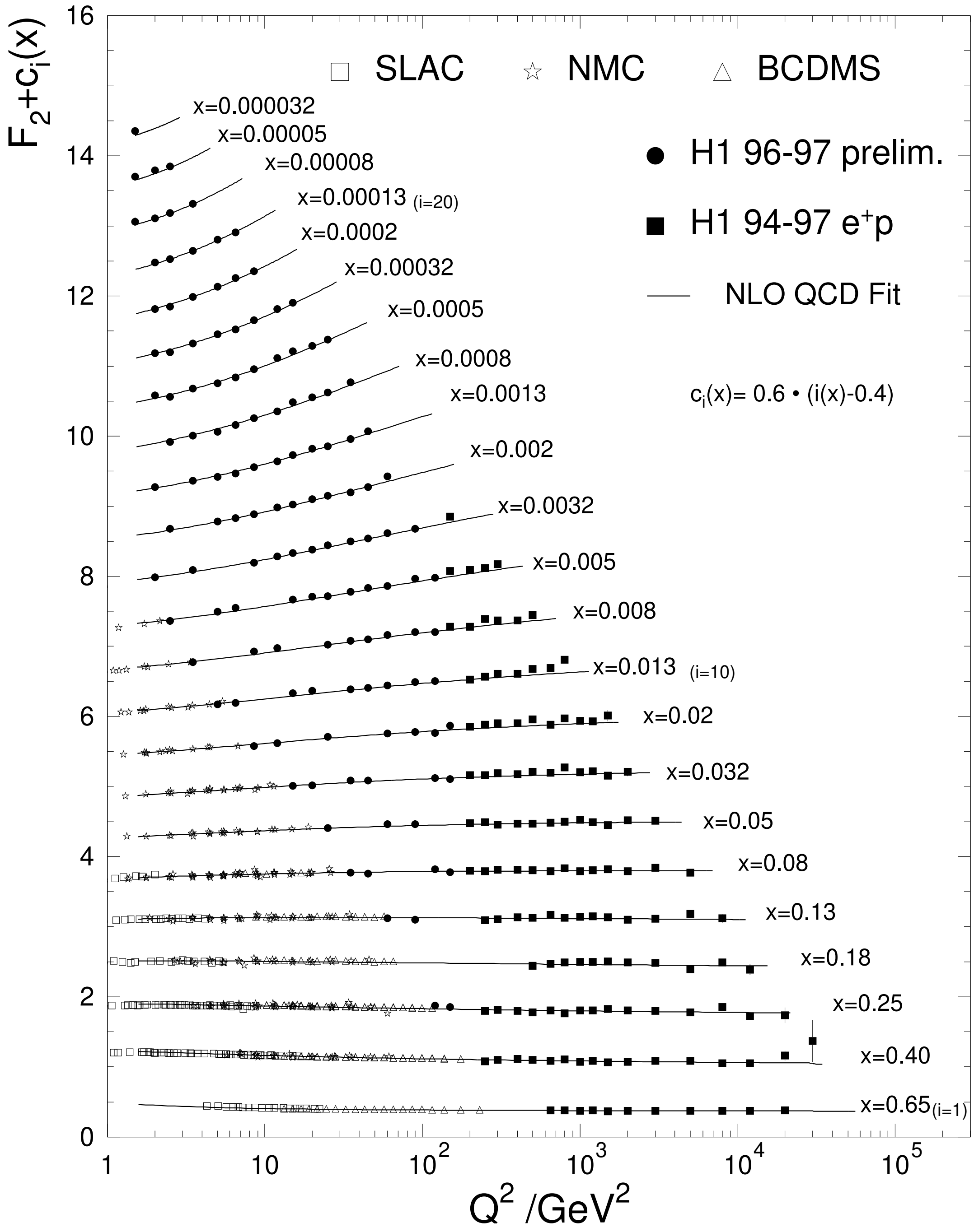

Figure 1.2: *The proton structure function F_2 obtained by measurements of the H1 collaboration, along with measurements from fixed target experiments. The solid curve represents a next-to-leading order QCD fit to these data, from [12].*

has been found in the framework of non-perturbative concepts e.g. Vector Dominance Model (VDM) or Regge theory, which will be shortly presented in this section.

The transition from the perturbative to the non-perturbative region yields several constraints on the structure functions F_1 and F_2 in order to connect both regions. As real photons at $Q^2 = 0$ are transversely polarized, the flux Γ_l vanishes and an upper limit on the total cross section is set by equation(1.18):

$$\sigma_{tot}^{\gamma p} \;=\; \lim_{Q^2 \to 0} \left[\sigma_{tot}^{\gamma^* p} \right] \;=\; \lim_{Q^2 \to 0} \left[\frac{4\pi^2 \alpha}{Q^2} F_2(x, Q^2) \right] \tag{1.26}$$

therefore F_2 has to behave like $\mathcal{O}(Q^2)$ in order to cancel the singularity. In the limit of $Q^2 \to 0$ the hadronic tensor $W_j^{\mu\nu}$ of equation 1.4 gives rise to singularities which are avoided by imposing the following behaviour on the structure functions F_1 and F_2:

$$F_2 \;=\; \mathcal{O}(Q^2) \qquad F_L \;=\; F_2 - 2xF_1 \;=\; \mathcal{O}(Q^4) \tag{1.27}$$

At present the connection of non-perturbative to perturbative concepts is not well understood and the development of a fundamental description of both the photoproduction and the DIS regime requires intensive studies of the transition region. The main motivation of this analysis is to investigate this transition region by measuring the proton structure function $F_2(x,Q^2)$ and the total virtual photon-proton cross section $\sigma_{tot}^{\gamma^* p}$ in the region $0.08\ \mathrm{GeV}^2 < Q^2 < 0.35\ \mathrm{GeV}^2$ with the VLQ spectrometer.

Vector Dominance Model

It is well known since the 1960's that photon-hadron interactions exhibit characteristic similarities to hadron-hadron interactions. This empirical observation leads to the assumption that the photon is a superposition of a bare pointlike photon and a hadronic component. This hadronic component is generated by a fluctuation of the bare photon to a $q\bar{q}$ pair with the same quantum numbers as the photon ($J^{PC} = 1^{--}, Q = B = S = 0$):

$$|\gamma\rangle \;=\; |\gamma\rangle_{bare} + |\gamma\rangle_{hadronic} \tag{1.28}$$

In the VDM the assumption is made that the photon-hadron interaction is only given by the interaction of the hadronic component of the photon with the proton. Fluctuations into the three lightest vector mesons ρ, ω and ϕ are considered if the fluctuation time into a $q\bar{q}$ pair is large compared to the interaction time. As the interaction of the vector meson with the proton is dominated by soft processes, a description of the interaction is not possible in the realm of perturbative QCD. The underlying processes are divided into two contributions. A diffractive contribution where the interaction is described by the exchange of a colourless particle (one distinguishes processes where the photon and/or the proton dissociate: photon dissociation, proton dissociation and double dissociation) and a non-diffractive contribution where the vector meson itself interacts with the proton.

Although measurements confirmed the general validity of the ansatz [13], it was found that the contribution from the three lightest mesons only accounts for 78% of the total cross section. A model developed by G.A. Schuler and T. Sjöstrand [14][15][16] incorporates additional direct and anomalous processes besides the VDM component. In this model the real photon is composed of four contributions:

$$|\gamma\rangle = c_{dir}|\gamma\rangle_{dir} + \sum_{V=\rho,\omega,\phi} c_V|V\rangle + c_q|q\bar{q}\rangle + \sum_{l=e,\mu,\tau} c_l|l\bar{l}\rangle \tag{1.29}$$

$|\gamma\rangle_{dir}$ denotes the direct component. The leptonic component $|l\bar{l}\rangle$ is negligible as leptons do not couple via the strong interaction. The VDM component $|V\rangle$ incorporates the bound $q\bar{q}$ states, while in the quarkonic contribution $|q\bar{q}\rangle$ the quarks have higher transverse momenta.

The total γp cross section is then described by the following expression:

$$\sigma^{\gamma p}_{tot}(y) \;=\; \sigma^{\gamma p}_{dir}(y) + \sigma^{\gamma p}_{VDM}(y) + \sigma^{\gamma p}_{anom}(y) \tag{1.30}$$

$\sigma^{\gamma p}_{dir}$ includes the direct processes between the bare photon and the proton. For scattering processes with a final state particle with high transverse momentum, perturbative QCD is applied. $\sigma^{\gamma p}_{VDM}$ is given by VDM. In the anomalous contribution, given by $\sigma^{\gamma p}_{anom}$, the photon fluctuates into a $q\bar{q}$ pair with high transverse momenta and the cross section is calculated within perturbative QCD.

Regge phenomenology

The ansatz to describe two-particle scattering processes in strong interactions by the exchange of a single particle failed due to the violation of unitarity at high center-of-mass energies s. In the 1960's Regge theory was developed which includes multiple particle exchange and avoids the violation of unitarity. It was found that Regge theory successfully describes the phenomenology of hadron-hadron interactions in the high energy limit [17]. Regge theory is based on the analytic properties of the scattering amplitude A as a function of the angular momentum j. An introduction into Regge theory is given in [18].

It was found that particles of a given strangeness and isospin are connected by a line in a plot of the angular momentum j versus the corresponding mass m_j^2. These lines are the so-called Regge trajectories. The scattering process is now viewed as t-channel exchange of all possible particles of these Regge trajectories. In the high energy limit, $s \to \infty$, the total cross section σ_{tot} in hadron-hadron interactions is then given by the sum over all possible trajectories:

$$\sigma_{tot}(s) \;\propto\; \sum_i A_i(s) s^{\alpha(t=0)-1} \tag{1.31}$$

The intercepts $\alpha(t=0)$ of all known trajectories were found to be less than 1, resulting in a decreasing cross section with increasing center-of-mass energy $\sqrt{s}$. This behaviour is in contrast with the observed slow rise of the total cross section with increasing s. One postulated therefore a new trajectory, called Pomeranchuk trajectory, with $\alpha(t = 0) > 1$ which yields the observed rise at high energies.

As was mentioned in the description of the VDM, hadron-hadron interactions show characteristic similarities to photon-hadron interactions and therefore Regge theory may also be applied to ep interactions. Regge theory is in particular interesting for this analysis as the kinematic region covered by the VLQ spectrometer ($Q^2 \ll s$) corresponds to the high energy limit, where Regge theory is valid.

1.6.1 Low x-Low Q^2 Models

The models which will be discussed in this section are based on the non-perturbative concepts described in the previous section and are suited for the description of the transition region. One model, based on the self-similar properties of the proton structure, will be presented.

DL - Donnachie-Landshoff

In a model proposed by Donnachie and Landshoff [19] the total cross section in hadron-hadron scattering as well as the photoproduction cross section is well described by the sum of two Regge-trajectories:

$$\sigma_{tot} = X s^{\epsilon_1} + Y s^{\epsilon_2} \tag{1.32}$$

where s is the square of the center-of-mass energy. The first term takes into account the Pomeron exchange (with $X = 0.0677$ mb and $\epsilon_1 = \alpha_{I\!P} - 1 = 0.0808$) and the second term the exchange of a Reggeon ($Y = 0.129$ mb and $\epsilon_2 = \alpha_{I\!R} - 1 = -0.4525$). Extending the above ansatz to the region of $Q^2 \neq 0$ GeV^2, the structure function F_2 can be parameterized in the following way:

$$F_2(x, Q^2) = f_1(Q^2)x^{-\epsilon_1} + f_2(Q^2)x^{-\epsilon_2} \quad \text{with} \quad f_i(Q^2) = A_i \left(\frac{Q^2}{Q^2 + a_i}\right)^{1+\epsilon_i} \tag{1.33}$$

The term $f_i(Q^2)$ determines the Q^2-behaviour of the structure function as $Q^2 \to 0$ and goes to 1 for large Q^2. In an extended ansatz [20] Donnachie and Landshoff add a third term to the F_2 parameterization corresponding to a so-called hard pomeron with $\epsilon_0 = 0.44$:

$$F_2(x, Q^2) = \sum_{i=0}^{2} f_i(Q^2)x^{-\epsilon_i} \tag{1.34}$$

ALLM97 - Abramowicz, Levin, Levy, Maor

The ALLM-parameterization [21] is based on a Regge motivated approach, similar to DL, extended into the large Q^2 regime in a way compatible with QCD expectations and covers the whole phase space in Q^2 and x. The proton structure function is assumed to be the sum of the contributions of the Pomeron $I\!P$ and the Reggeon $I\!R$ exchanges:

$$F_2(x,Q^2) \;=\; \frac{Q^2}{Q^2+m_0^2}\left(F_2^{I\!P}(x,Q^2)+F_2^{I\!R}(x,Q^2)\right) \tag{1.35}$$

where m_0 is the effective photon mass. The contributions F_2^i $(i = I\!P, I\!R)$ take the following form:

$$F_2^i(x,Q^2) \;=\; c_i(t)x_i^{a_i(t)}(1-x)^{b_i(t)} \qquad \frac{1}{x_i} \;=\; 1+\frac{W^2-M^2}{Q^2+m_i^2} \qquad t \;=\; \ln\left(\frac{\ln\frac{Q^2+Q_0^2}{\Lambda^2}}{\ln\frac{Q_0^2}{\Lambda^2}}\right) \tag{1.36}$$

where Λ is the QCD scale, M is the proton mass and m_i $(i = I\!P, I\!R)$ are interpreted as effective Pomeron and Reggeon masses. The large number of parameters (23 in all) is determined via a fit to the experimental data including HERA data at low x and low Q^2.

CKMT - Capella, Kaidalov, Merino, Tran-Than-Van

The CKMT model is a theoretical model based on Regge theory and provides a formulation of the proton structure function in the region of small and moderate Q^2. In this model the proton structure function $F_2(x,Q^2)$ is composed of a singlet F_S and a non-singlet F_{NS} term:

$$F_2(x,Q^2) \;=\; F_S(x,Q^2)+F_{NS}(x,Q^2) \tag{1.37}$$

The singlet term corresponds to the Pomeron contribution:

$$F_S(x,Q^2) \;=\; Ax^{-\Delta(Q^2)}(1-x)^{n(Q^2)+4}\left(\frac{Q^2}{Q^2+a}\right)^{1+\Delta(Q^2)} \tag{1.38}$$

where the effective Pomeron intercept Δ and n are depending on Q^2:

$$\Delta(Q^2) \;=\; \Delta_0\left(1+\frac{\Delta_1 Q^2}{Q^2+\Delta_2}\right) \qquad n(Q^2)=\frac{3}{2}\left(1+\frac{Q^2}{Q^2+c}\right)$$

The non-singlet term corresponds to the Reggeon contribution:

$$F_{NS}(x,Q^2) \;=\; Bx^{1-\alpha_{I\!R}}(1-x)^{n(Q^2)}\left(\frac{Q^2}{Q^2+b}\right)^{\alpha_{I\!R}} \tag{1.39}$$

where $\alpha_{I\!R}$ corresponds to the value from Donnachie and Landshoff.

Two sets of constant parameters (A, Δ_0, Δ_1, Δ_2, c, a, B, α_R and b) are considered in this analysis. The first set results from a fit to pre-HERA data [22] while the second set was determined by a fit to an enlarged data sample including measurements from HERA at small and moderate Q^2 [23].

Fractal Fit - T. Laštovička

In the region of low x the concept of self-similarity leads to a simple parameterization of the quark densities $q_f(x)$ within the proton [24]. Using relation 1.21 between quark densities and proton structure function F_2, the following expression is obtained:

$$F_2(x,Q^2) \;=\; \frac{e^{D_0}Q_0^2 x^{-D_2+1}}{1+D_3-D_1\log x}\left(x^{-D_1\log(1+\frac{Q^2}{Q_0^2})}(1+\frac{Q^2}{Q_0^2})^{D_3+1}-1\right)$$

The parameters have been determined using recent data from H1 and ZEUS in the range of $(0.045 \le Q^2 \le 120\ \mathrm{GeV}^2)$.

2
The H1 Detector at HERA

Research work at the Deutsches Elektronen Synchrotron (DESY) began in 1964 with the start of an electron synchrotron in Hamburg. In subsequent years research activities continued at the e^+e^- storage rings DORIS[1] and later PETRA[2]. Among many other physics topics investigations on charm and beauty quarks (DORIS) and the discovery of gluons at PETRA were most important. In the late 1980's a new lepton-proton storage ring HERA[3] was constructed which went into operation in 1992. The construction of a 30 km linear e^+e^- accelerator TESLA[4] is in the planning stage.

After a short overview of the HERA collider the components of the H1 detector relevant to this analysis are presented. Special emphasis will be placed on the the Very Low Q^2 (VLQ) spectrometer of the H1 experiment. Finally the reconstruction of the HERA kinematics using the Electron Method and the Hadron Method will be discussed.

2.1 HERA

In 1992 the HERA collider started operation. It consists of two separate storage rings in a tunnel of 6336 m circumference between 10 and 25 m below ground. Electrons[5] and protons are accelerated to 27.5 GeV and 920 GeV[6] respectively, resulting in a center-of-mass energy $\sqrt{s} = \sqrt{4E_eE_p} \approx 318\text{GeV}$, and stored for several hours. These beams are brought to collision in two interaction points at the center of the multi-purpose detectors H1 and ZEUS (see figure 2.1 left). Additionally there are two fixed target experiments HERA-B and HERMES. In the HERA-B experiment proton-nucleon scattering is investigated by inserting wire targets of various materials in the proton beam tail. The HERMES experiment studies the spin

[1]Doppel-Ring-Speicher

[2]Positron-Elektron-Tandem-Ring-Anlage

[3]Hadron-Elektron-Ring-Anlage

[4]TeV Superconducting Linear Accelerator

[5]The present analysis is based on data from a minimum bias run in 1999, where the accelerated leptons were positrons. As the charge of the lepton is not relevant to this analysis, no discrimination between electrons and positrons is made.

[6]Until 1998 the proton energy was limited to 820 GeV.

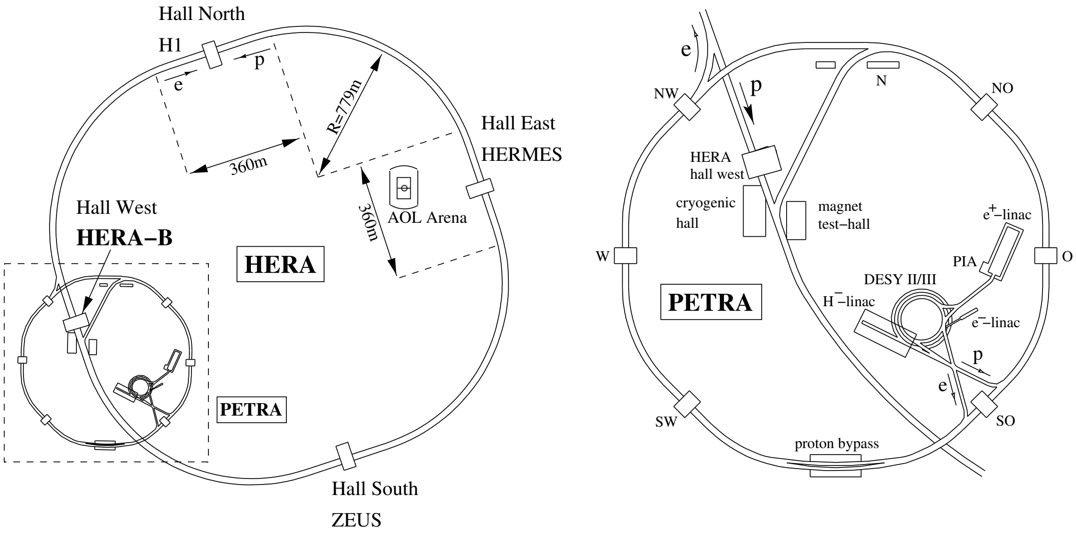

Figure 2.1: *The HERA collider (left) and the preaccelerators at the DESY site (right)*

structure of nucleons by colliding longitudinally polarized electrons on various gaseous targets of polarized atoms.

Before being injected into HERA electrons and protons pass a complex system of preaccelerators (see figure 2.1 right). Electrons are accelerated in a 500 MeV linear accelerator, DESY II and PETRA before they are injected into HERA with an energy of 12 GeV. Protons are produced by passing H^- ions through a stripper foil. The resulting proton bunches are then accelerated in DESY III and PETRA until they are finally injected into HERA with an energy of 40 GeV. Inside HERA electrons and protons are then accelerated to their final energies of 27.5 and 920 GeV respectively. Electrons and protons are stored in ≈ 175 bunches, each consisting of $10^{10} - 10^{11}$ particles, leading to typical currents of 35 mA for electrons and 90 mA for protons. At the interaction points, bunches cross at an interval of 96 ns corresponding to a bunch crossing rate of 10.4 MHz. An average value for the specific luminosity of $\mathcal{L}_{\text{spec.}} \approx 0.6 \cdot 10^{30}\text{cm}^{-2}\text{sec}^{-1}\text{mA}^{-2}$ is reached.

2.2 The H1 Detector

The H1 detector has been designed as a nearly hermetic general purpose detector to investigate various aspects of electron-proton scattering. A detailed description of the H1 detector can be found in [25].

The analysis discussed in this thesis is based on data collected in the end of 1999. This section will describe the structure of the H1 detector at that period of time. Since then the H1 experiment has undergone a major upgrade during the shutdown in 2000/2001.

An isometric view of the H1 detector is shown in figure 2.2. It consists of various subcomponents which measure the energy, momentum and type of the final state particles

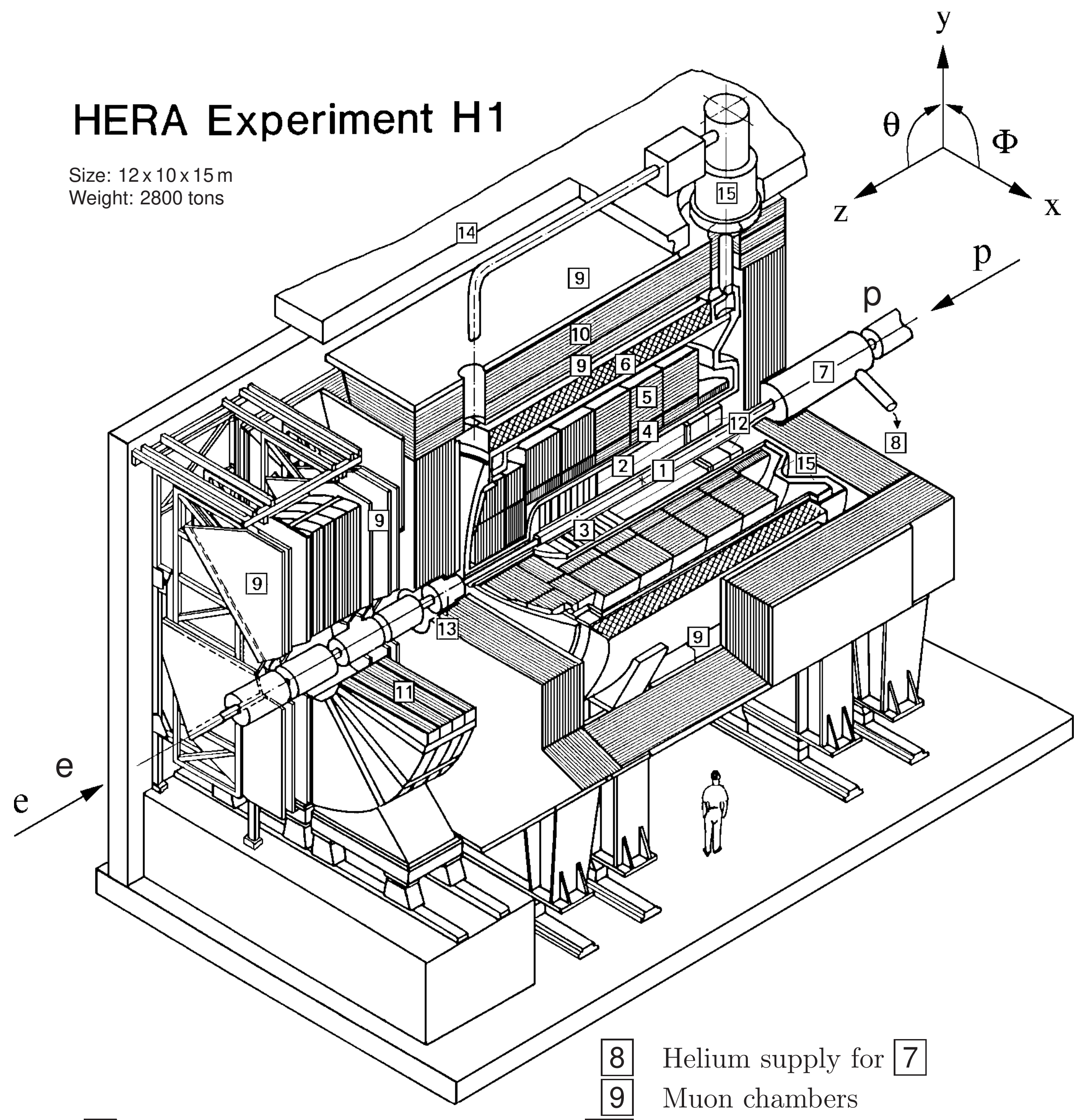

1	Beam pipe and beam magnets
2	Central track detectors
3	Forward track detectors
4	Electromagnetic LAr calorimeter
5	Hadronic LAr calorimeter
6	Superconducting coil (1.15 T)
7	Compensating magnet
8	Helium supply for 7
9	Muon chambers
10	Instrumented iron yoke
11	Forward muon toroid
12	SPACAL and Backward DC
13	PLUG calorimeter
14	Concrete shielding
15	Liquid argon cryostat

Figure 2.2: *The H1 detector*

resulting from the ep interaction. Due to the asymmetry of the energies of the colliding particles the center-of-mass system is moving along the proton flight direction relative to the laboratory frame system. The H1 detector accommodates for this Lorentz Boost and the resulting collimation of the final state particles in proton flight direction with an enhanced instrumentation in the forward direction. In the following all relevant sub-components of the H1 detector will be described. The **V**ery **L**ow Q^2 spectrometer is of particular interest for the measurement of the proton structure function F_2 at very low Q^2 presented in this analysis. It will be described in detail in section 2.2.5.

The H1 coordinate system is defined as a right-handed coordinate system (see figure 2.2) with its origin at the nominal interaction point. The z-axis points to proton flight direction, the y-axis in the upward direction and the x-axis towards the center of the HERA ring. The polar angle θ is defined with respect to the positive z-axis and the azimuthal angle ϕ relative to the positive x-axis.

2.2.1 Tracking

The H1 tracking system, shown in figure 2.3 provides a precision measurement of the momentum of charged particles over a wide range in polar angles ($5° < \theta < 178°$) and with full azimuthal coverage. A superconducting solenoid encloses both tracking and calorimetry and produces a uniform magnetic field of 1.15 T parallel to the beam axis.

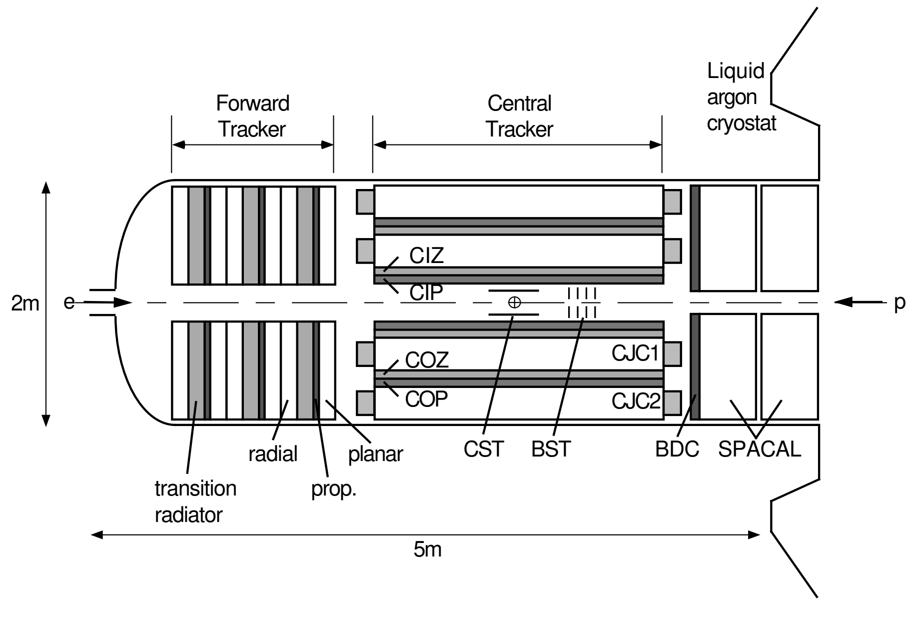

Figure 2.3: *Side view of the tracking system of the H1 detector.*

The interaction point is surrounded by a cylindrical silicon tracking system CST[7] which

[7]Central Silicon Tracker

consists of two layers of semi-conductor strip detectors. The readout strips on both sides of the silicon detectors are perpendicular to each other and thus provide a measurement of tracks in two projections. A second vertex detector BST[8] in the backward direction covers a range of $162° < \theta < 176°$. Due to the high spatial resolution of silicon strip detectors CST and BST considerably improve the resolution of the track reconstruction and allow the determination of secondary vertices. The silicon trackers are enclosed by the central tracking device which mainly consists of two cylindrical drift chambers (CJC1[9] and CJC2) with wires parallel to the beam axis. These chambers cover a range of $-1.5\text{m} < z < 2\text{m}$ in z-direction and measure transverse momenta of charged particles with a resolution of $\delta p_T/p_T < 0.01 \cdot p_T/\text{GeV}$. Particle identification is provided through the measurement of the specific energy loss dE/dx. The CJC1 chamber is surrounded by two drift chambers (CIZ[10] and COZ[11]) whose wires are perpendicular to the beam axis, improving the measurement of the z-coordinate of the interaction vertex (typical resolution 300 μm). These z-chambers are again surrounded by two multi-wire-proportional chambers (CIP[12] and COP[13]) which are able to deliver a fast trigger signal due to their good timing resolution and due to the good vertex resolution in z-direction. In the very forward direction ($5° < \theta < 25°$) tracks are measured with a system of three identical modules. Each of them is composed of a planar drift chamber, a multi-wire-proportional chamber, transition radiators and a radial drift chamber. An additional drift chamber (BDC[14]) in the backward direction of H1 covers a range of polar angles of $153° < \theta < 178°$. In this analysis the central jet chambers of the H1 tracking system are used to determine the event vertex and the momenta of the charged particles of the hadronic final state.

Detection of muons produced in the ep scattering is achieved by the muon system. In the central region muon tracks are detected in the instrumented iron yoke, which consists of limited streamer tubes embedded in the iron yoke of the solenoid. Measurement of muon momenta in the very forward direction is provided by the forward muon system. Muons which are deflected in the magnet field of the forward muon toroid are detected in two drift chambers surrounding this magnet.

The tracking device of the VLQ spectrometer will be discussed in detail in section 2.2.5.

2.2.2 Calorimetry

The calorimetry section of the H1 detector provides a measurement of the energy of the final state particles and is constituted of five sub-components: the liquid argon (LAr) calorimeter,

[8]Backward Silicon Tracker
[9]Central Jet Chamber
[10]Central Inner Z-chamber
[11]Central Outer Z-chamber
[12]Central Inner Proportional chamber
[13]Central Outer Proportional chamber
[14]Backward Drift Chamber

the spaghetti calorimeter (SPACAL), the tail catcher, the plug calorimeters and the VLQ calorimeters. For a detailed description of the tail catcher and the plug calorimeters see [25]. The calorimeters of the VLQ spectrometer will be discussed in detail in section 2.2.5.

The central and forward regions ($4^\circ < \theta < 154^\circ$) of the H1 detector are covered by the LAr calorimeter with full azimuthal coverage. It consists of an electromagnetic part with high granularity surrounded by a hadronic part. Both parts are contained in a single cryostat. Liquid argon at 90° K is used as active material. In the electromagnetic section of the LAr the absorbing material is made of lead while in the hadronic section steel absorber plates are used. The orientation of the absorber plates can be seen in figure 2.4. The LAr calorimeter is embedded in the superconducting solenoid to improve the resolution of the energy measurement by reducing the amount of dead material in front of the calorimeter.

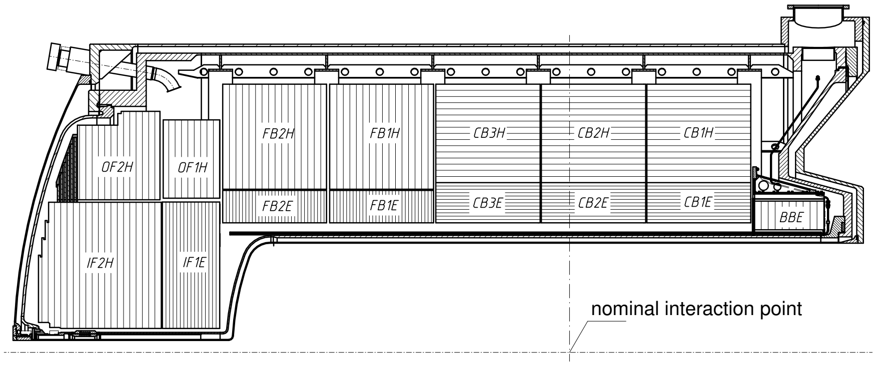

Figure 2.4: *Side view of the upper half of the LAr calorimeter.*

The depth of the electromagnetic section is 20 - 30 radiation lengths, while the depth of the hadronic part is 4 - 6 interaction lengths. A weighting technique is applied to the measured hadronic energies taking into account the non-compensating nature of the LAr calorimeter.

In the backward region the SPACAL calorimeter covers a range of polar angles of $153^\circ < \theta < 177.8^\circ$ with full azimuthal coverage. Like the LAr it consists of an electromagnetic (27.5 radiation lengths) and a hadronic section (1 interaction length). Both sections use scintillator fibers parallel to the z-axis as active material and lead as absorber. The inner part of the SPACAL is called insert and is used to measure the amount of energy leakage out of the electromagnetic section of the SPACAL. The insert shades parts of the VLQ calorimeters and thus reduces the acceptance of the VLQ, see figures 4.7 and 6.2.

2.2.3 Luminosity System

The accurate determination of the luminosity is of major importance for a cross section measurement. For a given physical process the integrated luminosity $\mathcal{L}_{\text{int}}$ gives the relation between cross section σ_{process} and observed number of events N_{observed}:

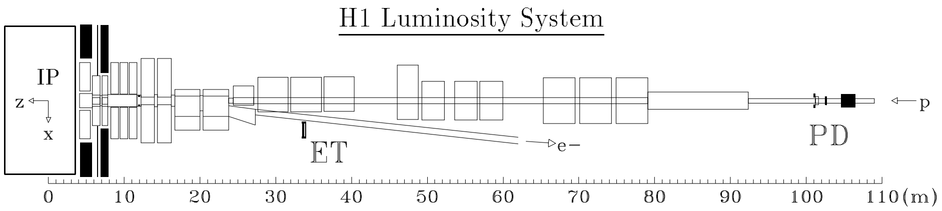

Figure 2.5: *Side view of the luminosity system of the H1 detector.*

$$\sigma_{\text{process}} = \frac{N_{\text{observed}}}{\mathcal{L}_{\text{int}}}$$

The accurate theoretical knowledge of a cross section and a precise measurement of the event rate enable thus the determination of the luminosity. In the HERA case the elastic Bremsstrahlung process, also called Bethe-Heitler process, is used for the luminosity measurement:

$$e\,p \rightarrow e\,p\,\gamma$$

The outgoing e and γ are detected in coincidence in the electron tagger (ET) at a z-position of -33.4 m and the photon detector (PD) at -102.8 m. Figure 2.5 shows a side view of the luminosity system. The uncertainty of the luminosity determination in this analysis amounts to 1.5 %.

2.2.4 Data Acquisition

At HERA proton and electron bunches collide with a frequency of 10.4 MHz, corresponding to a bunch crossing time of 96 ns. In table 2.1 the rates of several physical processes recorded by the H1 detector are illustrated. The highest rates are induced by underground reactions: synchrotron radiation of the electron beam, interactions of the high energy protons with the beampipe (beam-wall events) or with gas atoms remaining inside the beampipe (beam-gas events). As the rates of these reactions (50 kHz) are several orders of magnitude higher than for processes of physical interest ($<$ 25 Hz), it is necessary to implement a triggering system which heavily reduces the recorded amount of background. Additionally this triggering system should provide a possibility to enhance or decrease the rate at which certain event signatures are stored permanently e.g. during certain designated phases events which have been triggered by the VLQ spectrometer are stored with higher priority.

The triggering system consists of four levels. On level 1 (L1) all recorded events are analyzed in a dead time free way. The information delivered by the H1 detector is stored in a pipeline structure on the Front End electronics with a depth of 32 entries. Part of the

Process	Rate
Beam-gas	50 kHz
Photoproduction (e^- in VLQ)	20 Hz
Deep-inelastic scattering (e^- in LAr)	0.04 Hz
W-production	10^{-5} Hz

Table 2.1: *Rates of various physical processes at design luminosity ($\mathcal{L} = 1.5 \cdot 10^{31}\mathrm{cm}^2\,\mathrm{s}^{-1}$) in the H1 detector.*

information of the sub-detectors, e.g. energy sum of adjacent calorimetric cells, vertex information, etc. is subsequently combined to form so-called triggerelements. Triggerelements of various components are then combined to physics subtriggers in order to select processes of particular physical interest from the large number of underground events. On trigger level 1 it is also possible to apply prescales to subtriggers with high rates. The prescaling gives a possibility to increase or decrease the relative weight of subtriggers in the stored data set. For example a W-production subtrigger would in general have a prescale of 1 meaning that every event is accepted by L1 whereas VLQ triggers with a rate of 20 Hz would have a high prescale of 200, so that the rate of events triggered by this subtrigger drops to 0.1 Hz.

If the event is accepted by L1, the continuous readout of the H1 Front End electronics is stopped and the event is further analyzed by the second level trigger (L2) which is composed of two independent systems: L2TT and L2NN[15]. Both systems analyze geometric correlations between the information of different components of the H1 detector. If the event is accepted by L2, the full readout of all channels is started. This procedure takes ≈ 1 ms. At the end of the readout the data taking by the H1 Front End electronics resumes. The duration of the readout is called dead time.

Finally on the trigger level 4 (L4)[16] a nearly full reconstruction of the events is carried out by a processor farm. Selection cuts based on physical quantities are applied, e.g. jet requirements, energy reconstructed in the VLQ calorimeters, and the accepted events are classified according to physical criteria. The information of all the readout channels is then permanently stored on tape. The output rate of the whole trigger system amounts to ≈ 5 Hz in standard data taking, whereas during minimum bias runs rates up to 40 Hz are recorded.

A full offline reconstruction of the event is then provided by the `H1REC` program. The variables of physical interest e.g. calibrated cluster energies, tracks, etc. are then calculated from the raw information of all sub-components (e.g. digitized pulses) and stored on so-called POT's[17]. In the final step the data are compressed and finally made available to the physics working groups under the form of DST's[18].

[15] Level 2 Topological Trigger and Level 2 Neural Network
[16] The third level trigger (L3) has only been implemented in the year 2001 after the luminosity upgrade.
[17] Production Output Tape
[18] Data Summary Tape

2.2.5 VLQ Spectrometer

In order to study the transition region between the non-perturbative region at low Q^2 and the perturbative region at high Q^2 in ep scattering (see section 1.6) an accurate reconstruction of the kinematic variables Q^2, x and y is required. To access the transition region $0.01 < Q^2 < 1\,\mathrm{GeV}^2$ a precise measurement of the scattered electron or hadronic final state under very small angles is necessary. Using the Hadron Method (see section 2.3.2) would require a precise measurement of a low energy hadronic final state which exceeds the acceptance of the H1 detector. On the contrary the Electron Method (section 2.3.1) ensures the optimal reconstruction of the relevant variables through the detection of the scattered electron. The kinematic acceptance of the H1 detector has been extended by the installation of the Very Low Q^2 (VLQ) spectrometer in the year 1998. This device provides the required measurement of the energy and the angle of the scattered electron under very small angles in the backward direction. The kinematic coverage of the H1 detector including the extension due to the VLQ spectrometer and the phase space of several fixed-target experiments are shown in figure 7.2.

In this analysis the measurement of the proton structure function F_2 in the phase space region covered by the VLQ spectrometer is presented. Therefore a detailed description of the detector components of the VLQ spectrometer is given in the following sections.

Design

The design of the VLQ-spectrometer was determined by several constraints [26]. Covering the transition region as described above requires the detection of electrons under very small scattering angles taking into account the increased background near the beampipe. Moreover this new device has to fit into the existing physical structure of the H1 detector. Finally it was decided to insert the VLQ spectrometer at a position of $z = -3077$ mm inside the iron yoke of H1 in front of the end flange of the compensator solenoid, see figure 2.6. Since at these scattering angles the ep cross section is large, a full azimuthal coverage is not necessary. To allow in-situ calibration and alignment via the measurement of QED-Compton events two modules back-to-back in azimuth are required. The two identical modules are mounted above and below the beam pipe which avoids direct exposure to the synchrotron radiation fan in the horizontal plane of the accelerator. To protect the electronics from high background during unstable beam conditions e.g. injection, both modules can be moved out of their data taking position close to the beampipe via precise moving mechanics. Figure 2.7 shows the upper module in data taking position whereas the lower module is protected against radiation behind the iron yoke. Each module consists of a silicon tracking device and a compact tungsten-sandwich calorimeter. A time-of-flight system for vetoing proton induced beam-gas and beam-wall events is also included in the VLQ spectrometer.
In order to reduce the amount of dead material in front of the VLQ spectrometer a new beampipe with two exit windows in front of the modules has been installed, see figure 2.7.

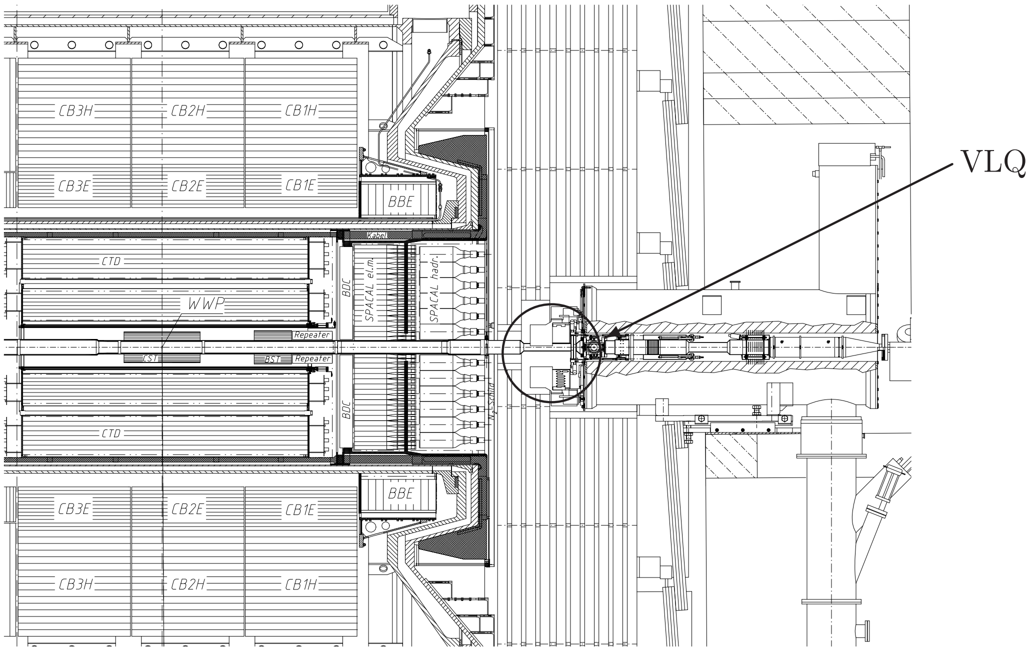

Figure 2.6: *Longitudinal cut of the backward region of the H1 detector including the VLQ spectrometer. The upper module is shown in data taking position close to the beampipe, whereas the lower module is in the parking position behind the instrumented iron. WWP denotes the nominal interaction point.*

The transverse size of the new beampipe is reduced to allow for the detection of electrons under smallest possible scattering angles. The acceptance of the VLQ at large scattering angles is restricted by the insert of the SPACAL.

VLQ Calorimetry

The highest constraints on the design of the VLQ calorimeters were set by the limited space available inside the H1 detector. In order to ensure a satisfactory longitudinal and lateral containment of the electromagnetic shower, compact calorimeters of the energy projection type were built[27], see figure 2.8. They are based on a sandwich structure with alternating layers of active and passive material. One layer of active material is segmented in narrow vertical scintillator bars and the following layer in horizontal scintillator bars and so on. Compactness of the device is achieved by using tungsten plates between the scintillator planes as passive medium. In total each calorimeter is composed of 24 scintillator planes and 23 absorber plates covering a total area of 90×120 mm with a depth of 130 mm. To prevent cross talk between neighbouring bars each scintillator bar is wrapped in paper. The light produced by the energy deposition in the scintillator material is transferred to the front faces of the bars by total reflection. Thereafter the light is coupled into the wavelength shifters (WLS). To ensure a stable optical behaviour scintillator bars and WLS are kept at a fixed distance of 0.2 mm. The WLS extend over the entire length of the calorimeter thus

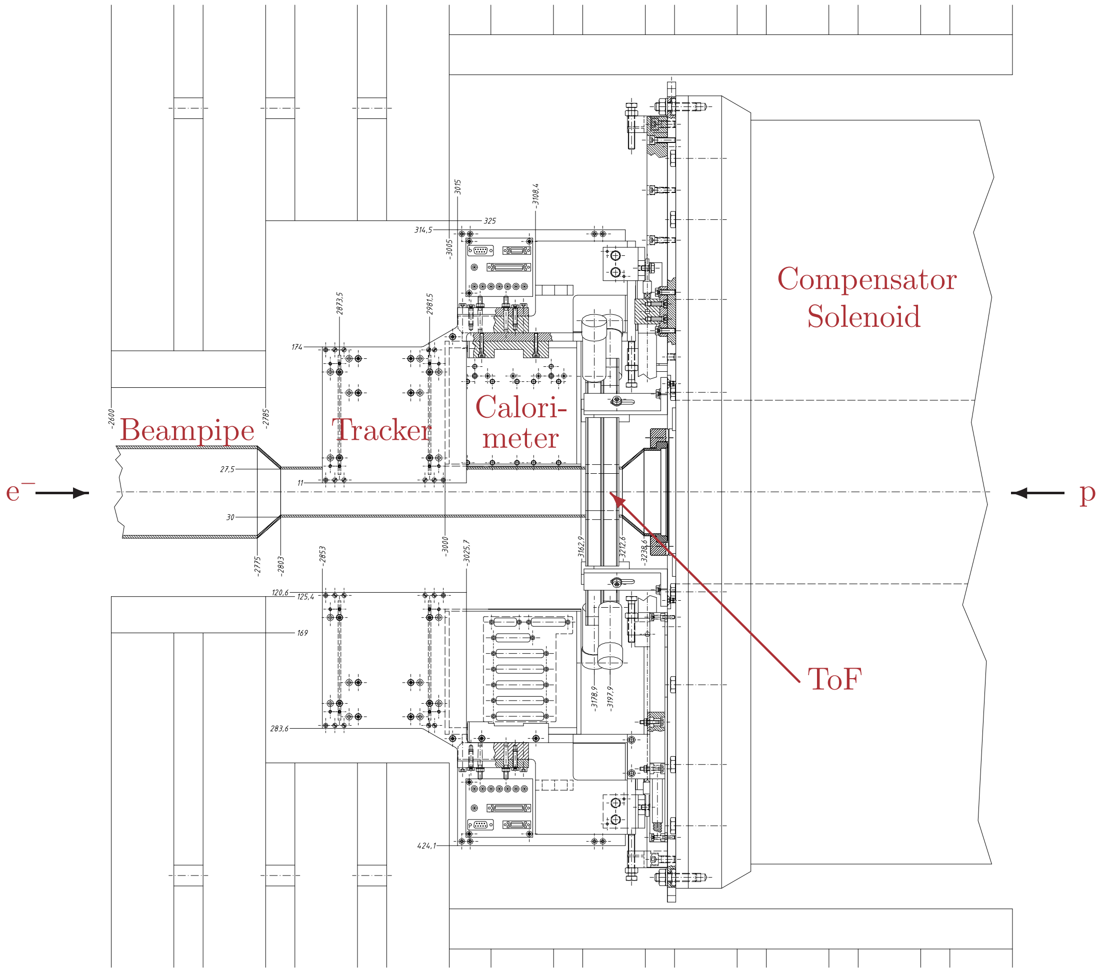

Figure 2.7: *Schematic layout of the VLQ spectrometer. The upper module is shown in the data taking position and the lower module in the parking position.*

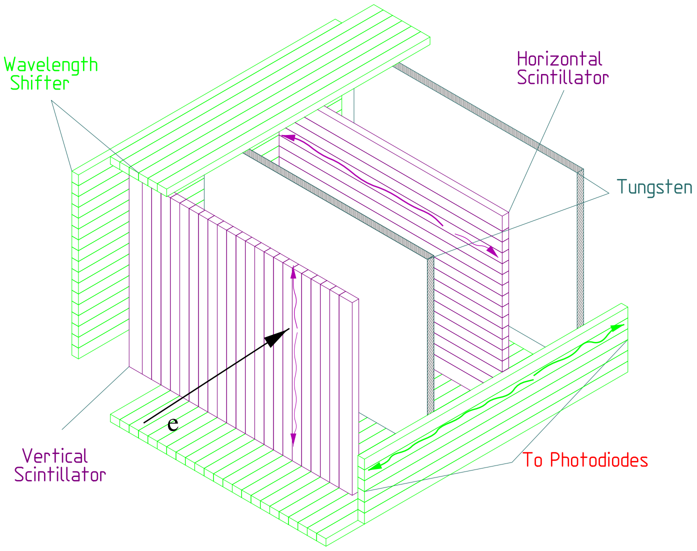

Figure 2.8: *Schematic layout of a VLQ calorimeter.*

adding the light from the horizontal and the vertical bars respectively. Additionally the blue light ($\lambda \approx 420$ nm) emitted by the scintillator bars is shifted to green ($\lambda \approx 500$ nm) by the WLS. The green light is reemitted into the direction of the photodiodes, which are glued to the wavelength shifters at the front and the back of the calorimeters. The wavelength shift is necessary to take advantage of the increased sensitivity of the photodiodes at the wavelength of green light. The photodiodes convert the absorbed light to an electronic signal. The readout of the photodiodes is done by a so-called FroPhoDiChi[19] chip. The amplified signals of both photodiodes of one wavelength shifter are summed up and sent to a standard H1 calorimeter data acquisition [25] located in the trailer of the H1 experiment. On one hand the readout signals are summed up to form trigger signals which are sent to the central trigger and on the other hand the readout signals are sent to the central H1 data acquisition. The trigger scheme of the VLQ calorimeters is discussed in detail in section 5.1.1.

The readout scheme of the VLQ calorimeters delivers four measurements of the shower profile, two horizontal and two vertical projections, see the upper module in figure 4.8. This scheme allows for a redundant reconstruction of the shower properties and thus the energy measurement. Additionally it represents an effective means to suppress so-called single diode hits. They are caused by photo-absorption of a synchrotron radiation photon in the depletion zone of a photodiode resulting in a large signal in one single isolated channel (see figure 4.8). This effect is especially dangerous in the trigger scheme because a single diode hit may fake an energy deposition up to several GeV in one channel which then exceeds the trigger

[19]Front End Photodiode Readout Chip [27]

thresholds causing a trigger signal. Online suppression of these single diode hits is done by comparing the energy deposited in opposite projections. If only one projection registers a signal, the event is identified as a single diode hit and the trigger signal is suppressed.

A description of the offline reconstruction of the VLQ calorimeter information and of the suppression of single diode hits is given in section 4.2, see also [28].

VLQ Tracking Device

The use of a tracking device in addition to a calorimeter improves the resolution of the impact position measurement of the scattered electron and provides an independent measurement of the z-position of the interaction vertex. Additionally a silicon tracker can be used to reduce the amount of background from neutral particles. Traversing charged leptons lead to a substantial primary ionization in silicon detectors in contrast to neutral particles (hadrons and photons) which pass the silicon sensors without depositing a substantial amount of energy. Therefore only tracks are reconstructed for traversing charged particles. Background events induced by neutral hadrons and photons do not yield a track within a silicon tracker and can therefore be rejected by a track requirement.

Each module of the VLQ spectrometer contains a tracking system (see figure 2.7) composed of microstrip silicon detectors each with an active area of 57.6×32 mm^2 and a thickness of 300 μm. They consist of n-type silicon with 1280 implanted p$^+$ strips[20] with a width of 12 μm and a pitch of 25 μm. Figure 2.9 shows the principle of a silicon microstrip detector. When applying a voltage of ≥ 30 V between the n-side and the p$^+$ strips a reverse p-n junction is created. An ionizing particle (e.g. the scattered electron) passing through the detector creates electron-hole pairs in the silicon bulk material. The electrons drift along the electric field towards the n-side while the holes drift to the p$^+$ strips. Every second of these strips is covered by a metallisation and the deposited charge is transferred to the preamplifier of the readout chip. The electric charge collected on the intermediate strips induces signals on the neighbouring readout strips by capacitive charge division, therefore improving the spatial resolution without increasing the number of readout channels. A total of 640 microstrips is read out for each silicon detector and the actual readout pitch corresponds to 50 μm. The spatial resolution is measured to be $\sigma = 10.12$ μm [29].
Wire bonds connect the silicon wafers to a hybrid which collects the Front End electronics, mainly the five readout chips APC128[21] [30]. The signals from the microstrips are amplified and stored in a pipeline. This pipeline consists of 32 buffers which allow to store the data in a dead time free way until the L1 trigger decision is taken. The steering of the Front End

[20] Actually both sides of the wafer are implanted with strips perpendicular to each other and therefore allow a measurement of both impact coordinates. In the VLQ tracker only the p$^+$ side is read out. A two-dimensional measurement of the impact position is realized by placing the silicon detectors perpendicular to each other.

[21] Analog Pipeline Chip

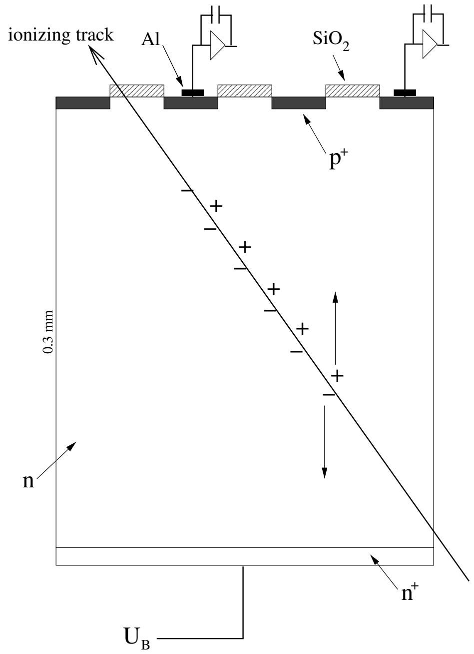

Figure 2.9: *Principle of a silicon microstrip detector.*

electronics is governed by an OnSiRoc[22] [31] [32] controller which is located in the electronics trailer. The readout and the online processing of the microstrip data is performed by a `RIO2 8060` [33] module also located in the electronics trailer.

The performance of the microstrip detectors used in the VLQ tracker was tested in a laser beam setup [34] prior to the insertion into the H1 detector. 2 % of the readout strips were found to be damaged.

Figure 4.1 shows the structure of one module of the VLQ tracking system. A tracker module consists of two double layers composed of 7 silicon strip detectors each. The microstrips of four of these silicon detectors are oriented along the x-axis and thus provide a measurement of the y-coordinate of the intersecting track. The remaining three are oriented along the y-axis to reconstruct the x-coordinate. Each double layer provides thus a measurement in the (x,y)-plane of the impact point of the scattered electron. Tracks are reconstructed by combining the impact points of both double layers in a linear fit.

During the minimum bias run 1999 both modules showed large interferences of the control signals in the readout electronics prohibiting a stable readout of the detectors. This situation improved by disconnecting the two outer most horizontal microstrip detectors in each double layer from the readout and thus reducing the interferences. The acceptance of the VLQ tracker was not reduced by this action, because the insert of the SPACAL shields the outer region of both track detectors[23]. 20 silicon microstrip detectors remained in the readout of

[22] Online Silicon Readout Controller

[23] In the original design of the VLQ spectrometer it was planned to remove the insert of the SPACAL.

the VLQ tracker, resulting in a total of $20 \times 640 = 12800$ readout channels. An area of 33×98 mm in the (x,y)-plane is covered by each tracker module. Unfortunately it will be shown in section 4.1 that the efficiency of the track reconstruction is still heavily reduced due to remaining interferences and bad cable connections.

The information delivered by the Front End electronics of each silicon detector, i.e. the signal amplitude of each channel, is then processed online on the `RIO2 8060` board by a so-called cluster finder. The signal amplitude A_i^k of a channel i for an event k is composed of several contributions [34]. The pedestal P_i originates from leakage currents of the strips which enter the preamplifier of the APC128. As this effect only varies slowly with time, the pedestal contribution is calculated over a large amount of events for each channel separately. The common mode C^k results from short-term variations of the low voltage applied to the preamplifiers or of the depletion voltage of the silicon bulk material. This results in an overall variation of the signal amplitude for all channels. The common mode contribution C^k for an event k is defined as the mean signal amplitude of all channels and is calculated for each APC128 separately. The noise σ_i originates from the electronic noise of the preamplifiers which varies from channel to channel due to the inhomogeneities of the silicon material and the production tolerance of the Front End electronics. Finally the charge deposited by the ionizing particle is distributed over several adjacent strips. In a first step the pedestal and common mode subtracted amplitude S of each channel is calculated: $S = A_i^k - P_i - C^k$. The actual cluster finding algorithm detects then single channels where the so-called signal-to-noise ratio $S/N = (A_i^k - P_i - C^k)/\sigma_i$ exceeds a certain value e.g. $S/N > 2$. The algorithm has detected a cluster if several adjacent channels fulfill the above S/N requirement. Additionally one requires the signal-to-noise ratio $(S/N)_{\mathrm{cluster}}$ of the combined channels to be larger than a cluster criterion ($(S/N)_{\mathrm{cluster}} > 4$). Finally the center-of-gravity of the cluster is calculated. Only the information concerning these clusters (first channel of cluster, cluster width and energy of each channel) is then sent to the data acquisition of the H1 experiment and stored permanently.

A detailed description of the VLQ tracking device and its reconstruction software can be found in [35], [36] and [34]. The performance of the VLQ tracker will be discussed in detail in section 4.1.

VLQ Time-of-Flight

Measuring the time difference between an energy deposition and the crossing of an electron and a proton bunch allows the distinction between *ep* induced events and background events. Whereas background events from beam-gas or beam-wall interactions are randomly distributed in time, energy depositions resulting from *ep* collisions only occur in a narrow time window given by the time of the bunch crossing (every 96 ns) and the flight duration of the scattered particles between the interaction point and the subdetector. Events which are detected outside this time window are subsequently rejected. A device which only delivers this time information is called a Time-of-Flight (ToF) system.

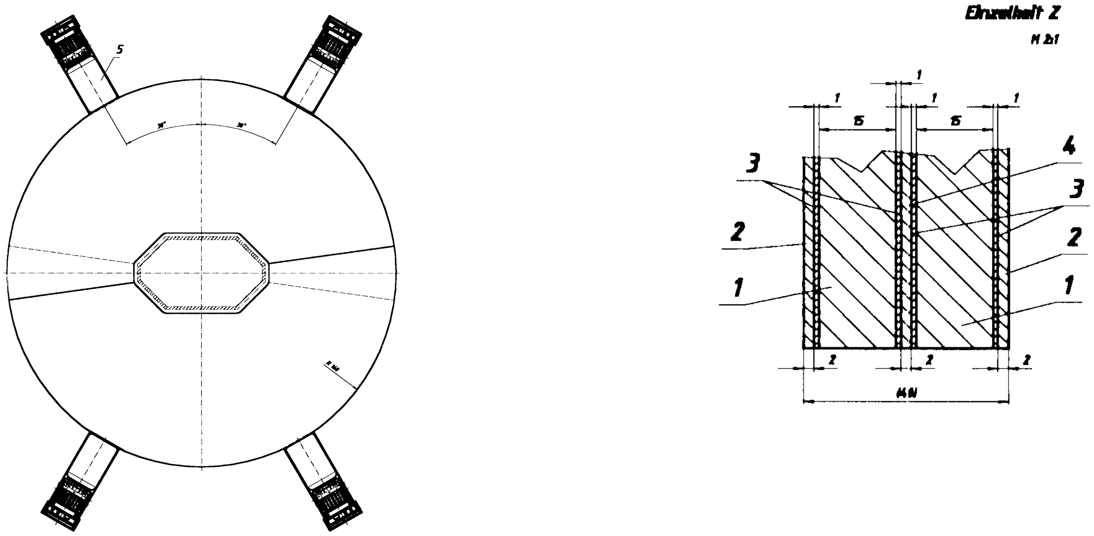

Figure 2.10: *Schematic view of the Time-of-Flight system of the VLQ spectrometer. On the right the front view is shown and the cross section on the left.*

The VLQ Time-of-Flight system is mounted directly to the beampipe between the VLQ spectrometer and the compensator solenoid (figure 2.7) and is composed of four semi-circular modules as shown in figure 2.10. On the right hand side the front view of the ToF system is shown. The cross section on the left depicts the structure of the ToF. It consists of two scintillators (1), wrapped in paper (3) and surrounded by lead absorber plates (2). The readout of the scintillators is performed via photomultipliers which provide a signal with a time resolution in the order of 1 ns.

2.3 Reconstruction of the Kinematics

As given by the relation $Q^2 = sxy$ (equation 1.3) the kinematics of an ep scattering process is determined by two independent variables at a fixed center-of-mass energy $\sqrt{s}$. These Lorentz invariant variables are not subject to a direct measurement by the H1 detector components. Accessible to direct measurement are: the energy and angle of the scattered electron and the energy and angle of all hadronic final state particles detected in H1 subdetector systems. A certain reconstruction method combines at least two of these measurements to determine two independent Lorentz invariant variables. In total 6 methods combine the measurement of the electron and of the hadronic final state to take advantage of the redundancy of the kinematics. Due to the restricted acceptance and the finite resolution of the H1 detector these methods differ in resolution of the kinematic variables and their sensitivity to QED radiative corrections. In the following the Electron Method and the Hadron Method are discussed.

2.3.1 Electron Method

In the Electron Method [37] the measured energy E'_e and angle θ_e of the scattered electron are used to reconstruct the kinematic variables:

$$\begin{aligned}
Q^2_e &= 2E_0E'_e(1+\cos\theta_e) \\
y_e &= 1-\frac{E'_e}{2E_0}(1-\cos\theta_e) \\
x_e &= \frac{Q^2_e}{y_e s}
\end{aligned}$$

where E_0 denotes the electron beam energy. The uncertainties of these variables are given as follows:

$$\begin{aligned}
\frac{\delta Q^2}{Q^2} &= \frac{\delta E'_e}{E'_e}\oplus\tan\frac{\theta_e}{2}\delta\theta_e \\
\frac{\delta y}{y} &= \frac{y-1}{y}\frac{\delta E'_e}{E'_e}\oplus\frac{1-y}{y}\cot\frac{\theta_e}{2}\delta\theta_e \\
\frac{\delta x}{x} &= \frac{1}{y}\frac{\delta E'_e}{E'_e}\oplus\tan\frac{\theta_e}{2}(x\frac{E_P}{E_e}-1)\delta\theta_e
\end{aligned}$$

The Electron Method delivers a good resolution of Q^2 over the full kinematic range, whereas the resolutions of x and y significantly decrease to low values of y (corresponding to high electron energies) due to the y-dependence of the uncertainties. Additionally the Electron Method is sensitive to initial state radiation where the energy of the incoming electron E_0 is reduced by the energy of the radiated photon.

2.3.2 Hadron Method

The Hadron Method [38] also known as Jacquet-Blondel-Method is based on the measurement of the energy and angle of the particles of the hadronic final state:

$$\begin{aligned}
Q^2_{had} &= \frac{(\sum_{had}p_x)^2+(\sum_{had}p_y)^2}{1-y_{had}} \\
y_{had} &= \frac{\sum_{had}(E-p_z)}{2E_0} \\
x_{had} &= \frac{Q^2_{had}}{y_{had}s}
\end{aligned}$$

where E and p_x, p_y and p_z denote the energy and momentum components of a particle (either calorimetric cluster oder track) of the hadronic final state and the sum runs over all particles of the hadronic final state. Due to the inferior energy resolution of hadronic energy measurements, the resolution of the kinematic variables is poor compared to the Electron Method. Only at low values of y a significant improvement relative to the Electron Method is achieved. The Hadron Method is mainly used to reconstruct the kinematics in processes where the outgoing lepton escapes detection by the H1 experiment (CC events or in the photoproduction regime).

3

Monte Carlo Simulation

The basic aim of an analysis in high energy physics is to compare measured observables, e.g. cross sections with theoretical predictions, in order to improve the understanding of the properties of the fundamental forces between elementary particles. The experimental setup has a strong influence on the measured physical observables due to the limited acceptance of detector components, the finite resolution of the position, momentum and energy measurements, etc. It is desirable to disentangle these detector effects from the measurement of the physical observable in order to compare measurements from various experiments. On the other hand one may want to unfold QED radiative corrections from the cross section measurement. As it is difficult to unfold these different effects using data alone, the Monte Carlo unfolding technique is used in this analysis. It is based on two components: Monte Carlo event generators and detector simulation. The MC delivers the particles of the final state for a given scattering process in accordance with theoretical presumptions while the simulation determines the detector response to the final state.

3.1 Monte Carlo Generator

In the following section the Monte Carlo generators (MC) used in this analysis are shortly presented.

3.1.1 PHOJET 10.6

The software package `PHOJET` [39] is used to generate a large inclusive event sample which is used for several purposes. The spatial and energy resolution of the VLQ calorimeters and the efficiency of the vertex determination are investigated with `PHOJET`. Moreover the choice of the binning as well as the unfolding of the data are done with this MC sample.

The calculation of the cross section in `PHOJET` is based on the interpretation of the *ep* scattering as absorption by the proton of virtual photons, emitted by the electron, see section 1.3. Two contributions are implemented in the `PHOJET` generator: diffractive and non-diffractive processes. Non-diffractive processes are divided into direct and resolved con-

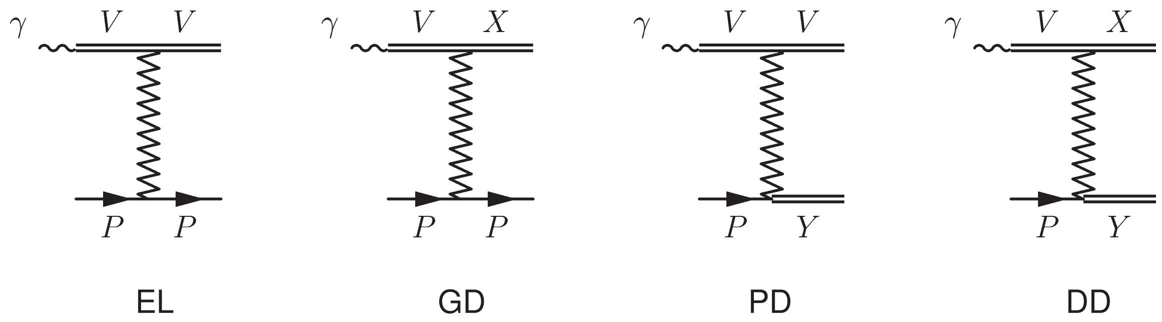

Figure 3.1: *Diffractive subprocesses in* `PHOJET`*: EL elastic vector-meson production, GD diffractive photon dissociation, PD diffractive proton dissociation and DD double diffractive dissociation.*

tributions, while four classes of diffractive subprocesses are included, see figure 3.1:

- elastic vector-meson production EL: $\gamma p \rightarrow Vp$
- diffractive photon dissociation GD: $\gamma p \rightarrow Xp$
- diffractive proton dissociation PD: $\gamma p \rightarrow VY$
- double diffractive dissociation DD: $\gamma p \rightarrow XY$

The relative contributions of the diffractive and non-diffractive subprocesses are weighted according to the scheme developed in [40].

High $p_\perp$ reactions are calculated in perturbative QCD while low $p_\perp$ reactions are modeled on the basis of Regge phenomenology. Initial state parton showers are generated according to a backward-evolution similar to the algorithms described in [41] and [42]. Final state parton radiation and the conversion of final state partons into stable hadrons (hadronization) is modeled according to the Lund string fragmentation [43], implemented in `JETSET` [44].

The total cross section in the generation process is given by the CKMT parameterization described in section 1.6.1. Subsequently the events are reweighted to a parameterization which gives a good description of the cross section measured in this analysis. This parameterization is given by the prediction of the ALLM collaboration (see section 1.6.1). QED radiative processes are not included in the cross section calculation, see also section 7.4.

For the measurement of the proton structure function F_2 in this analysis a total of $13.5 \cdot 10^6$ events were generated in the following phase space: $0.0001 < Q^2 < 1\text{GeV}^2$ and $0.001 < y < 1$. To take into account migrations this phase space has been chosen much larger than the actual VLQ phase space ($0.068 < Q^2 < 0.4\text{GeV}^2$ and $0.02 < y < 0.7$). Due to the strong rise of the cross section for decreasing y a weighting in the generation procedure was applied to reduce the relative amount of events in this region. Taking into account this weighting $16.5 \cdot 10^6$ events were generated corresponding to an integrated luminosity of 2.1

pb^{-1}. This represents approximatively twice the statistics of the data set. Subsequently the whole MC sample is processed by the simulation of the H1 detector.

In order to study the influence of photoproduction background on the cross section measurement a large sample of $8 \cdot 10^6$ events was generated in the photoproduction phase space ($Q^2 < 0.01\text{GeV}^2$ and $0.1 < y < 1$) and afterwards processed by the simulation. In the following this photoproduction MC will be labeled γp MC.

3.1.2 DJANGOH 1.1

In order to check the results of the calibration procedure a sample of 10^5 events is generated with the Monte Carlo event generator DJANGOH and afterwards processed by the simulation of the H1 detector. DJANGOH is an interface of the Monte Carlo programs HERACLES and LEPTO resp. ARIADNE [45]. The electroweak scattering process is calculated by HERACLES [46], including $\mathcal{O}(\alpha)$ electroweak corrections due to photon radiation from both the lepton and the quark as well as the complete one-loop virtual QED corrections. Parton cascades are generated using LEPTO [47] which is an implementation of the parton shower model. The full hadronic final state is generated with the help of JETSET [44] according to the Lund string fragmentation model [43]. The total cross section was calculated for the parton distributions from the MRST parameterization[1]. I addition the DJANGOH event sample is used in the investigations on the influence of radiative corrections on the structure function measurement.

3.1.3 COMPTON 2.00

The alignment procedure of the VLQ calorimeters is based on the Wide Angle Bremsstrahlung process $e\ p \ \rightarrow \ e'\ p\ \gamma$, also called QED Compton process, see section 4.2.2. In order to study the performance of the alignment procedure, the Monte Carlo program COMPTON [48] is used to generate a sample of QED-Compton events. The total cross section of the Wide Angle Bremsstrahlung process implemented in the COMPTON generator is composed of three contributions: elastic, quasi-inelastic and deep-inelastic subprocesses. The according Feynman diagrams are shown in figure 4.17.

A sample of $3 \cdot 10^5$ events was generated for the VLQ phase space and afterwards processed by the simulation of the H1 experiment. A detailed description of the parameter settings during the generation procedure can be found in [49].

3.2 Simulation of the VLQ Spectrometer

The detector response to the particles of the final state for generated events is simulated in detail by using the H1 detector simulation (H1SIM) which is based on the GEANT package

[1] Set 75 from the MRST parameterization was chosen.

[50]. A detailed description of the VLQ simulation and a comparison of simulated events to real data taken in 1999 can be found in [51]. In this section several specific features of the VLQ simulation will be shortly presented.

The alignment procedure, see section 4.2.2, has shown that the electron beam is not centered inside the beampipe at the z-position of the VLQ spectrometer but is located closer to the upper side of the beampipe. The beam is therefore also closer to the upper module of the VLQ spectrometer which sits on top of the beampipe in data taking position. The implementation of an asymmetric beam line was not compatible with the existing structure of the H1 detector simulation. It was decided to implement a beampipe with asymmetric exit windows thus allowing an asymmetric position of the VLQ modules relative to the beam. Figure 3.2 shows a schematic drawing of the geometry of the VLQ in the simulation. The upper exit window of the beampipe is larger than the lower one and thus enables the upper module to sit closer to the beam. Discrepancies in the comparison of data to MC, due to the different size of the exit window in reality and in the simulation, could only arise in the outer part of the VLQ spectrometer. Actually this does not affect the analysis described in this thesis, as the outer part of the VLQ spectrometer is shielded by the insert of the SPACAL, see figures 4.7 and 6.2. Additionally special emphasis has been placed on the correct simulation of the crosstalk effect between adjacent scintillator bars in the calorimeter. It is not necessary to include the effect of single diode hits in the calorimeter as single diode hits are efficiently recognized by the reconstruction of the VLQ calorimeters [28]. The energy depositions caused by single diode hits are removed before the cluster finding algorithm is started. The calibration of the VLQ calorimeters in the simulation is determined according to the procedure described in [40]. In chapter 4 detailed studies show that the simulated events give a good description of the data recorded with the VLQ spectrometer. The control distributions in section 7.3 illustrate the good agreement between the data and simulation, thus guaranteeing an accurate unfolding of the data.

To save computing time during the processing of large event samples, a fast simulation of the development of electromagnetic and hadronic showers inside the H1 experiment (`H1FAST` [52] [53]) was developed. After the simulation of the event sample is complete, the reconstruction of the simulated events is carried out (`H1REC`). This step of the processing is identical to the reconstruction of the data. Finally data and simulated Monte Carlo events are processed by the same analysis code.

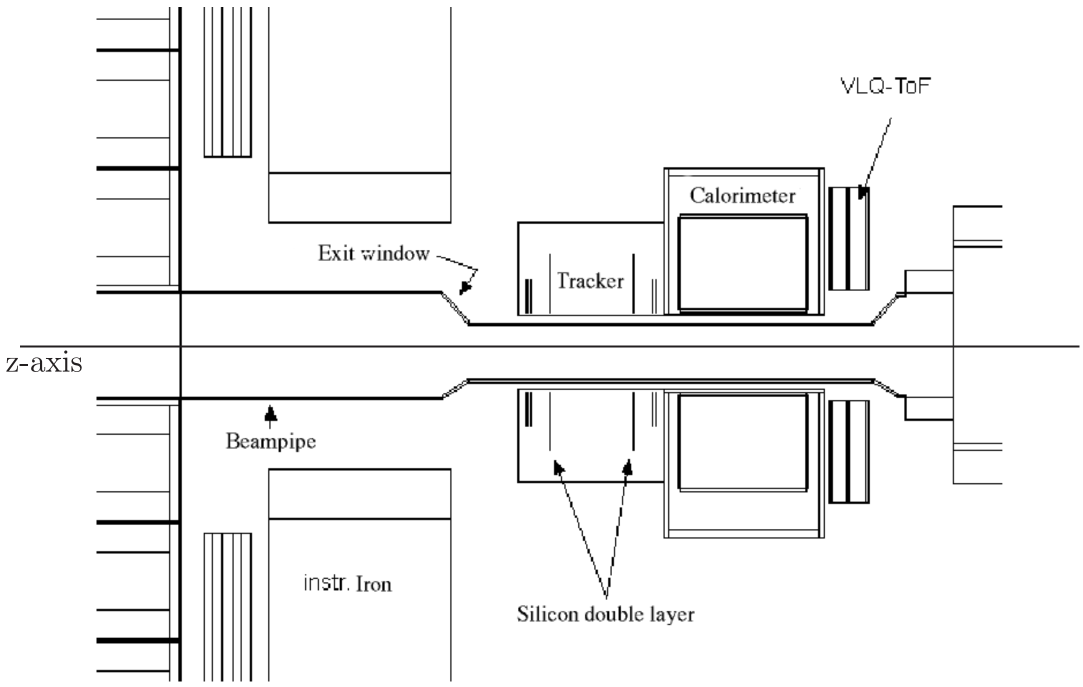

Figure 3.2: *Side view of the VLQ spectrometer and the modified beampipe implemented in the simulation of the H1 experiment.*

4

VLQ Reconstruction and Performance

The measurement of the proton structure function F_2 relies on the accurate determination of the kinematic variables Q^2, y and x. The reconstruction of the kinematic variables with the Electron Method requires a precise measurement of the energy and the polar angle of the scattered electron (see section 2.3.1). This places stringent conditions on the precision of the calibration and the position determination of the VLQ spectrometer. In the first part of the following chapter the track reconstruction and the performance of the VLQ tracker is discussed. It is shown that the efficiency of the VLQ tracker is reduced and therefore prohibits the use of the tracking information for the determination of the inclusive cross-section. The calibration of the calorimeter modules consisting of the channel-to-channel calibration and the determination of the absolute energy scale is outlined. Furthermore the position determination of the VLQ calorimeters via the acoplanarity of QED Compton events is presented in detail.

The studies on the performance of the VLQ spectrometer outlined in the following sections are based on the data set collected during the minimum bias run in 1999, which is described in detail in section 6.1.

4.1 Performance of the VLQ Tracking Device

VLQ Track Reconstruction

The reconstruction of tracks with the information of the VLQ tracker is performed by the software package `VLQTRK` [36] and consists of several steps.

As mentioned in section 2.2.5, the cluster reconstruction is performed online to reduce the amount of data to be stored. Based on these preprocessed data the first step of the VLQ track reconstruction consists in repeating the cluster finding algorithm with slightly stronger requirements. A channel is marked as hit when the signal-to-noise ratio exceeds the value 3. The cluster criterion remains at the value of 4, see section 2.2.5. For each cluster the center-of-gravity in channel units is then calculated.

In the second step the transformation of the position of the silicon clusters from the internal coordinates of the VLQ tracker to the H1-coordinate system is carried out. This transformation is based on the information gained by the alignment of the microstrip detectors to the VLQ calorimeters, described in detail in [36][1]. In this procedure the shift Δx, Δy and tilt $\Delta\alpha$ of every microstrip detector relative to the VLQ calorimeters are determined.

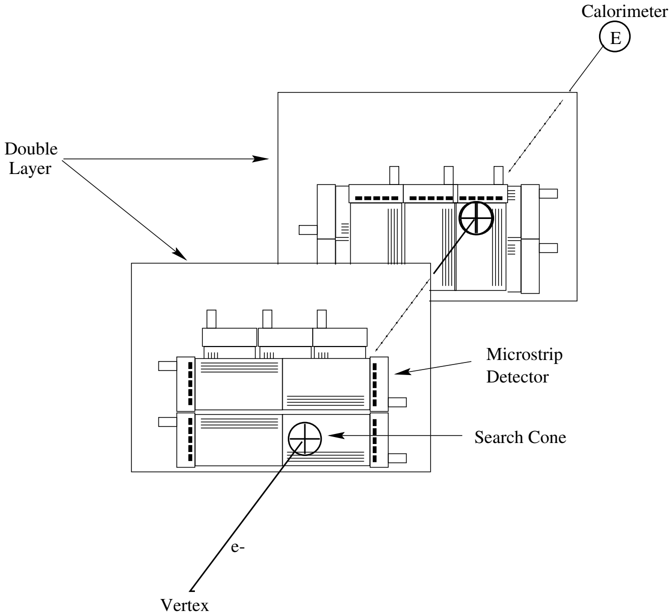

Figure 4.1: *Schematic view of the track reconstruction. The track results from the best fit to the silicon clusters lying inside a search cone around a pretrack connecting the calorimeter cluster and the event vertex.*

In the following step a pretrack is formed by linking the calorimeter cluster to the event vertex by a straight line, see figure 4.1. In case the H1 track chambers do not deliver any vertex information for this particular event, the mean run vertex is taken instead. All silicon clusters inside a radius of 3 mm around this pretrack are then selected. By combining the clusters from the horizontally oriented detectors to the clusters of the vertically oriented detectors for each double layer, all possible impact points in the (x,y)-plane are calculated.

If only one silicon cluster has been found inside the search cone, the reconstruction is not able to provide a VLQ track. If instead two or more silicon clusters are found in the search cone the last step of the track reconstruction is carried out. A linear fit to the impact points and the calorimeter cluster is performed. If several impact points are reconstructed in a double layer, all possible combinations with the impact points of the other double layer are calculated and the track hypothesis with the lowest χ^2 is selected. Subsequently θ and ϕ of the selected track are calculated. In case the y-coordinate of the impact point has been measured in both double layers an independent reconstruction of the z-coordinate of the interaction vertex is performed. The reconstruction of a z-vertex with only one y-coordinate measurement is difficult because the fit is unlikely to converge. For a detailed description of the VLQ track reconstruction see [36].

[1]Beforehand the alignment of the VLQ calorimeters is carried out, see section 4.2.2.

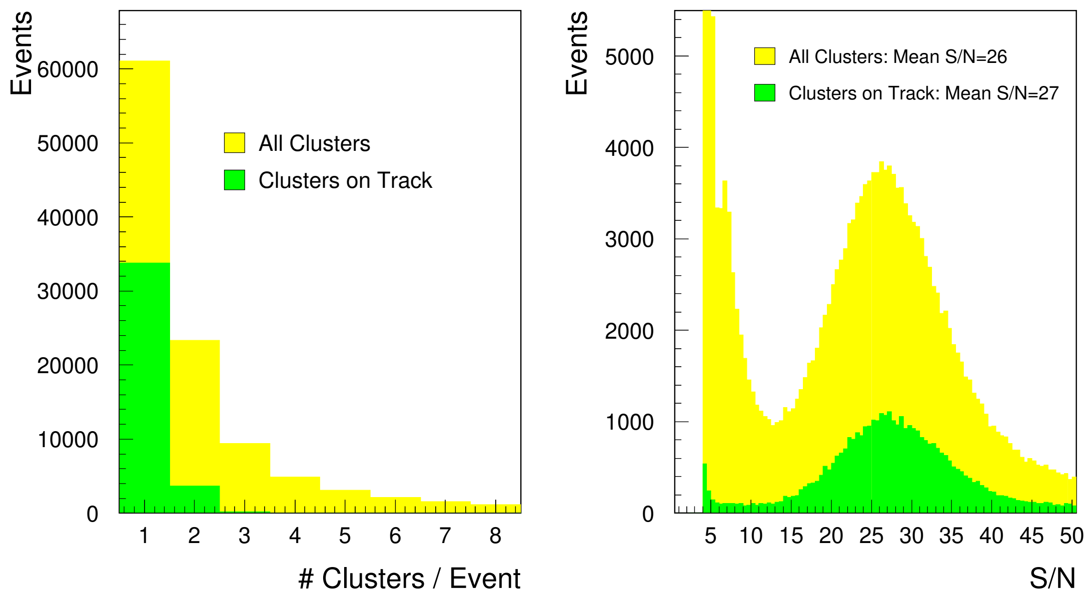

Figure 4.2: *The left diagram shows the number of clusters per event for detector 29. The light distribution depicts all clusters detected, whereas the dark distribution indicates the number of clusters belonging to a reconstructed track. The right diagram shows the signal-to-noise S/N distributions for all clusters (light) and for the clusters inside a track (dark). Additionally the mean S/N value is given.*

Performance of the Microstrip Detectors

In this section the behaviour of the microstrip detectors of the VLQ spectrometer in the HERA environment is studied. Moreover the influence of the track reconstruction is shown.

The light distribution in the left diagram of figure 4.2 depicts the cluster multiplicity distribution for all events in the microstrip detector 29. The tail to large multiplicities is due to fake clusters, caused by noisy channels, synchrotron radiation etc.. The dark distribution gives the number of clusters belonging to a reconstructed track. The number of clusters per event corresponds to the number of reconstructed tracks. The suppression of the tail to large cluster multiplicities is expected due to the fact that usually no more than two tracks are reconstructed per tracker module. The diagram on the right hand side shows the signal-to-noise ratio (S/N) of every detected cluster (light) and the signal-to-noise ratio of the cluster belonging to a track (dark). Both distributions show a peak at $S/N \approx 26$, which corresponds to the expected energy deposition of a minimal ionizing particle in silicon detectors [34]. Fake clusters are expected to show S/N values below 8. The dark distribution shows that these fake clusters are efficiently suppressed by the track requirement. Figure 4.3 shows the width d of the silicon clusters on the left and the hit map on the right side. Both distributions are given in units of microstrips. The light histogram shows the width of all clusters detected in detector 29. The distribution is steeply falling towards large values of d. On the contrary the dark distribution for the clusters belonging to a track peaks at a

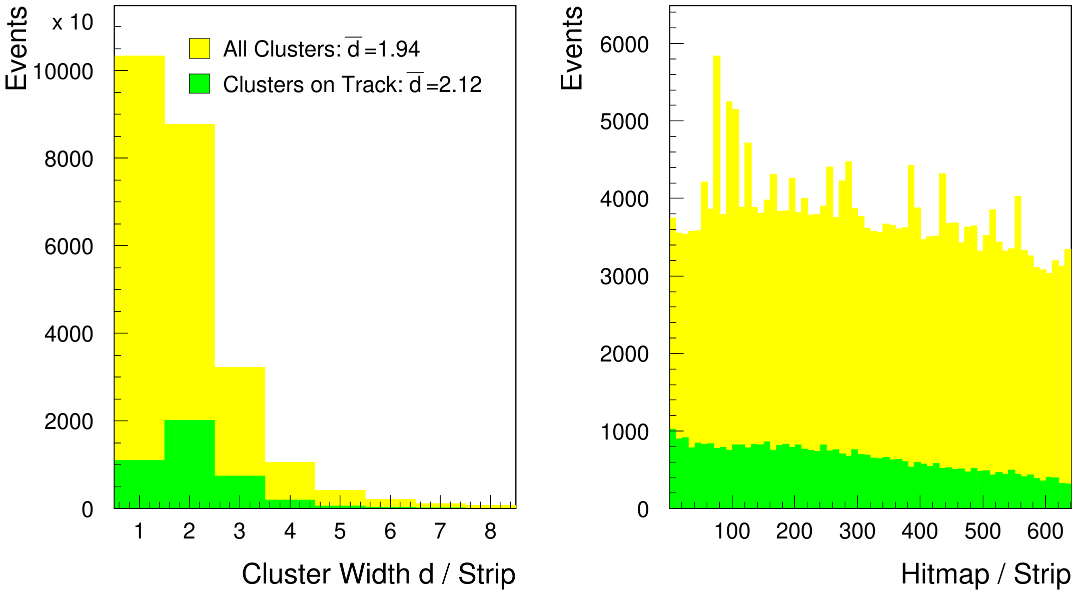

Figure 4.3: *Width (left) and center-of-gravity of the silicon clusters (right) for detector 29. The light distribution shows all clusters detected whereas the dark distribution only shows those clusters belonging to a reconstructed track.*

value of 2 and the tail to large values is suppressed. The peaks in the hitmap distribution are due to noisy channels. One can clearly see, that these noisy channels are suppressed by the track reconstruction, as these peaks do not appear in the dark distribution. Detector 29 shows thus the expected behaviour of a silicon microstrip detector in the environment of a collider experiment. The large amount of fake clusters is efficiently suppressed by the VLQ track reconstruction.

Unfortunately not all silicon detectors show the excellent behaviour of detector 29. In figure 4.4 the mean signal-to-noise S/N is given for all silicon detectors of the VLQ tracker[2]. 15 of the 20 silicon detectors show a mean S/N ratio above 15 for clusters on a track whereas no signals are reconstructed on the remaining five detectors. The malfunctioning of these detectors is explained in the following section. The limited performance of the individual silicon detectors has of course an impact on the performance of the VLQ track reconstruction, which is described in detail in the next section. Nevertheless a reconstruction of tracks, although with a reduced efficiency, is possible.

Figure 4.5 demonstrates the performance of the upper module of the tracker. The number of clusters for all events (shaded histogram) is given. The points represent the distribution for events with a validated track in the upper module. In addition the same distribution is shown for events where a track is reconstructed in the lower module. The solid line indicates thus the number of background clusters per event in the upper module. The expected behaviour

[2]The numbering scheme of the silicon detectors is in the range [1,32].

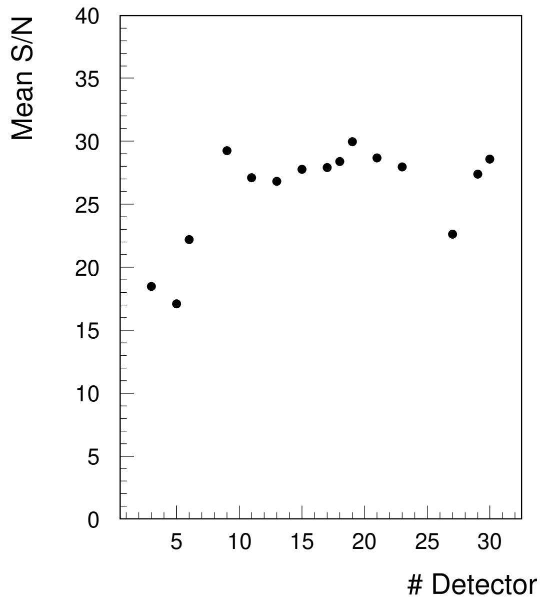

Figure 4.4: *Mean signal-to-noise ratio S/N of all 20 silicon detectors of the VLQ tracker. 15 detectors show a mean S/N above 15. The remaining 5 silicon detectors do not show any clusters.*

is seen, in average there are four clusters more in the distribution of events including a track, corresponding to the clusters in each of the four planes of the tracker module caused by the scattered electron.

Performance of the VLQ Track Reconstruction

The aim of the VLQ track reconstruction is the accurate measurement of the polar and azimuthal angle of the scattered electron. The spatial resolution of a VLQ tracker module has been determined in [36] to $\approx 20\ \mu$m compared to a resolution of $> 200\ \mu$m of the VLQ calorimeters (figure 4.9). The resolution of the z_{vtx}^{VLQ} measurement is determined to ≈ 4 cm. Additionally a silicon tracker may be used to reduce the background due to neutral particles. Neutral hadrons and photons, e.g. in the photoproduction background, do not lead to an energy deposition in the silicon detectors and thus no track will be reconstructed.

To investigate the performance of the VLQ track reconstruction, it is necessary to define a data sample where the amount of background, especially from photoproduction, is reduced. Only events with a single calorimeter cluster in the VLQ spectrometer with an energy above 20 GeV[3] are selected. Additionally an interaction vertex measured by the central tracker is required. Finally to ensure a good reconstruction of the calorimeter cluster the fiducial cuts, described in 6.2, are applied. Figure 4.6 shows the performance of the VLQ track reconstruction for the upper (left diagram) and the lower module (right diagram). For

[3]The relative contribution from photoproduction increases towards low energy depositions in the VLQ.

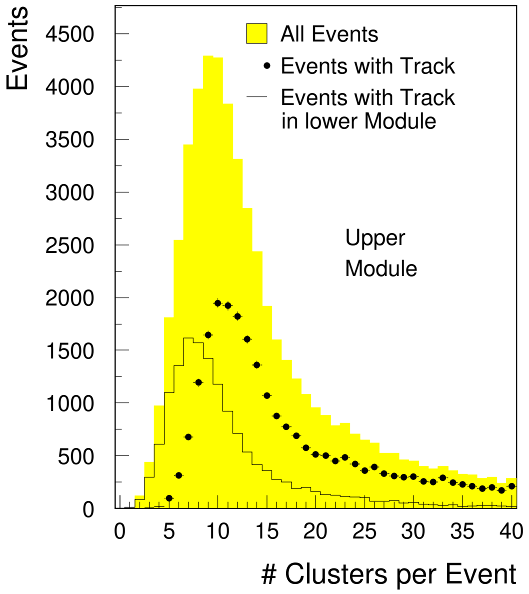

Figure 4.5: *Number of silicon clusters in the upper tracker module for all events (shaded histogram), for events with a track in the upper module (points) and for events with a track in the lower module (empty histogram).*

$\approx$ 10% of the events no VLQ track is reconstructed. Either no cluster or only a single silicon cluster is found in the search cone around the pretrack. In both cases the VLQ track reconstruction does not provide a track. In the remaining $\approx$ 90% of the events at least two silicon cluster have been found in the search cone and the VLQ track reconstruction provides a track. Only 50% (30%) of the events have clusters in each silicon layer of the upper (lower) module. In the dark distribution only events with a hit in both y-layers of the tracker are shown. For these events the track reconstruction provides an independent measurement of the z-component of the interaction vertex. If furthermore additional requirements on the track quality have to be fulfilled, the efficiency of the track reconstruction (points in figure 4.6) is even more reduced. The criteria applied to the individual tracks are listed below:

- An independent measurement of the z-component of the interaction vertex z_{vtx}^{VLQ}, thus requiring a hit in each y-layer of the tracker for the fitting procedure to be converging [36].
- -35 cm < z_{vtx}^{VLQ} < 35 cm: a standard cut on the z-vertex value provided by the track reconstruction.
- $R = \sqrt{(x_t - x_c)^2 + (y_t - y_c)^2} < 0.3$ cm: the distance between the impact points reconstructed with the tracker (x_t, y_t) and with the calorimeter (x_c, y_c) is required to be less than 0.3 cm.

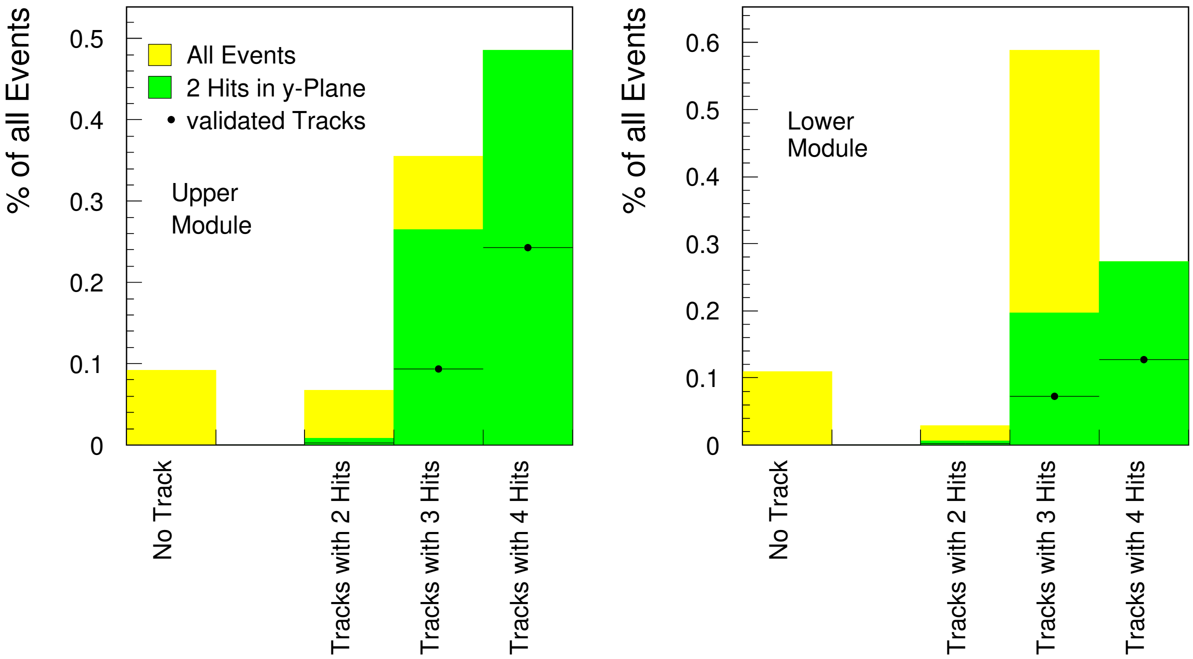

Figure 4.6: *Fraction of events fulfilling the requirements described in the text in dependence of the number of silicon clusters for the upper (left) and the lower module (right). The light diagram shows the distribution for each event. The dark distribution depicts the fraction of events with at least 2 clusters in the y-plane. The points represent the fraction of events with a validated track.*

For only ≈ 34% (20%) of the events for the upper (lower) module a so-called validated track fulfilling the above requirements is provided.

The low efficiency of the VLQ tracker modules is due to two reasons. Five microstrip detectors could not be correctly read out (see figure 4.4) because of bad cable connections in the readout chain resulting in dead areas in the tracking modules. Figure 4.7 shows the impact position of the scattered electron reconstructed with the VLQ tracker. Only tracks with two clusters in the y-layers are included allowing the independent measurement of the z coordinate of the interaction vertex. For the upper module the fiducial area (delimited by the gray lines) is continuously populated. Impact positions are even reconstructed outside the fiducial area, due to faulty combinations of silicon clusters during the track finding procedure. For the lower module only the right half of the fiducial area is populated with tracks. It can be seen that the horizontal microstrip detector on the left side of the lower tracker module was broken and therefore no tracks with two clusters in the y-layer could be reconstructed. As was mentioned in section 2.2.5, interferences of the control signals on the sub-repeater motherboard[4] in the readout electronics prohibited a stable readout of the detectors. The disconnection of two silicon detectors in each tracker module improved the

[4]On a sub-repeater motherboard the control signals provided by the OnSiRoC are duplicated and subsequently sent to the microstrip detectors.

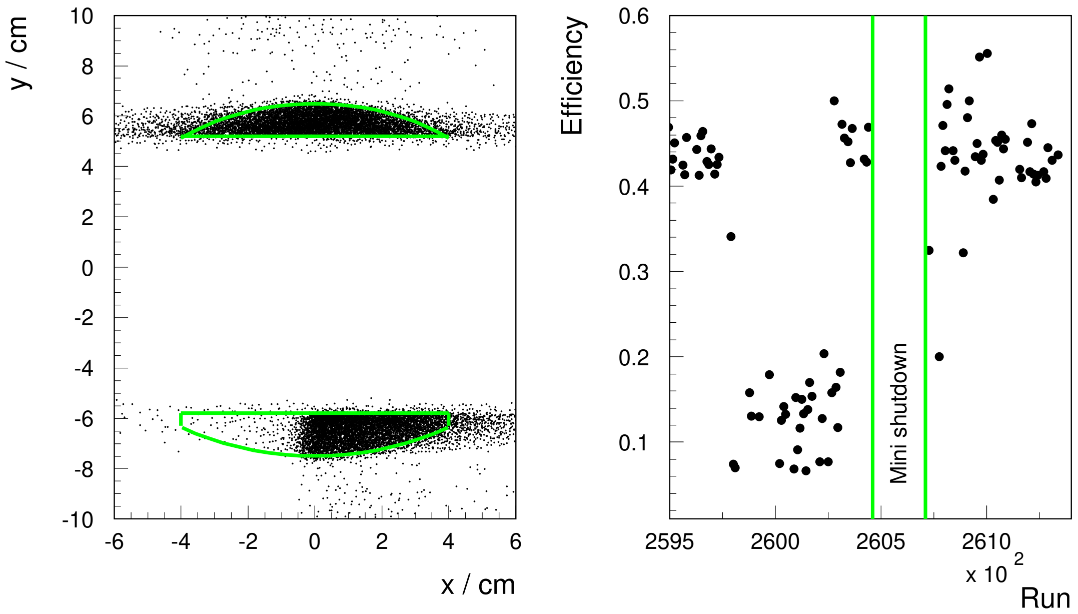

Figure 4.7: *Impact position of the scattered electron reconstructed with the VLQ tracker (left). Only tracks with two clusters in the y-layers are shown. The lines indicate the fiducial cuts described in 6.2. The shielding of the SPACAL insert can be clearly seen. Run dependence of the efficiency of the upper module (right).*

situation. Unfortunately the remaining interferences were still large enough to distort the shape of the control signals resulting in a malfunctioning of the whole module during certain periods of time. The time dependence of the VLQ track reconstruction efficiency for the upper module is shown in the right diagram of figure 4.7. Over the whole run range the efficiency has an average value of 45% except for a period of 500 runs where the efficiency is reduced to $\approx$ 15% due to the interferences described above. The minimum bias run was interrupted for maintenance during 3 days, a so-called mini-shutdown. During this period no data were recorded.

As a result of the investigations on the efficiency of the VLQ tracker, the decision was taken that the VLQ tracker modules were not to be used in the measurement of the proton structure function F_2. On the other hand, the tracker modules were used to suppress the amount of background in several phases of the detector studies (i.e. trigger efficiency calculation, determination of spatial resolution of the calorimeters) where the overall efficiency of the tracking was not relevant.

4.2 Performance of the VLQ Calorimeters

A VLQ calorimeter delivers four measurements of the lateral shower profile, two horizontal and two vertical projections. The advantages of this four-projections readout are redundant

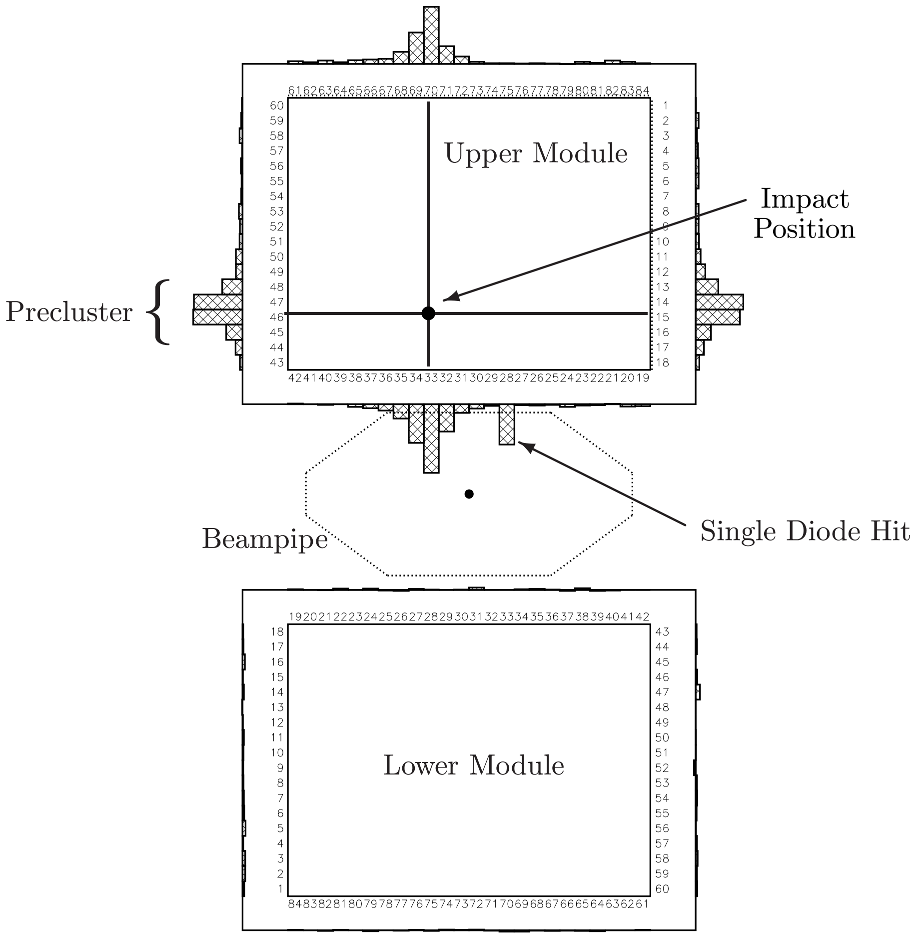

Figure 4.8: *VLQ event display with an energy deposition in the upper module. Preclusters as well as a single diode hit are shown.*

information for shower reconstruction and energy measurement as well as an effective way to suppress the single diode hits, described in section 2.2.5. Before the reconstruction of the energy cluster starts all single diode hits have to be removed. The event display in figure 4.8 shows a single diode hit in channel 28. Using the redundancy of the calorimeter readout the identification of single diode hits is achieved by comparing the energy in one channel (in this case channel number 28) with the channel on the opposite side of the calorimeter (in this case channel number 75). If the ratio of the channel energies exceeds a certain limit the energy in the channel is identified as resulting from a single diode hit and set to zero. If the single diode hit is located inside a cluster, the channel energy is set to the mean energy of the neighbouring channels. For a detailed account of the reconstruction of the VLQ calorimeter information see [28].

The first step of the reconstruction consists of finding preclusters in all four projections. The precluster finder searches channels with a local energy maximum by calculating the first and second derivative of the neighbouring channel energies. If a single precluster is found in a projection a common mode subtraction is performed. The so-called common mode consists of coherent fluctuations of the readout signals for all channels caused by e.g. variations of the voltage supplied to the preamplifiers or interferences by other detector components. To determine the common mode the mean of the energy response of all channels outside a radius of 2.5 cm of the energy maximum is calculated on an event-by-event basis for each projection. This common mode is then subtracted from all channels of the projection. Subsequently the original algorithm described in [28] sums up all common mode subtracted channel energies in a fixed radius around the maximum, the radius only depending on the energy of the most energetic channel. In this analysis the algorithm was altered to improve the linearity of the energy measurement, see section 4.2.1. The cluster radius is not fixed anymore and all the channel energies with an energy above noise level are summed up in the energy measurement. If multiple preclusters are found in one projection, it is not possible to perform a common mode subtraction because the number of channels outside the preclusters is too low to calculate a reasonable mean value. In this case the clustering of the channel energies is done with a fixed radius according to [28].

The center-of-gravity n_{Cl} of each precluster is then calculated according to a logarithmic weighting of the channel energies:

$$n_{Cl} = \frac{\sum_{i=1}^{N} w_i n_i}{\sum_{i=1}^{N} w_i} \qquad \text{with} \qquad w_i = \begin{cases} W_0 + \ln\left(\frac{E_i}{E_{cl}}\right) & \left(\frac{E_i}{E_{cl}}\right) > e^{-W_0} \\ 0 & \left(\frac{E_i}{E_{cl}}\right) < e^{-W_0} \end{cases}$$

with n_i the coordinate of channel i in x resp. y direction and $E_{cl} = \sum_{i=1}^{N} E_i$ the energy sum over the entire cluster composed of N channels. Only channels above a W_0 dependent energy threshold are used in the center-of-gravity determination. The dimensionless cut-off parameter is set to $W_0 = 3$ according to an analysis done in [35].

In the last step the preclusters are combined to the final clusters. In the case of one precluster in each projection, the cluster energy is the sum of all precluster energies. The x-(y)-coordinate corresponds to the mean of the center-of-gravity of the preclusters in the two horizontal (vertical) projections. In a small fraction of the events, several clusters occur in one projection. If in this case the number of clusters in one projection do not match the number of clusters in the opposite projection, a consistent combination of the preclusters is not possible and the event is rejected. If instead the number of preclusters is equal in opposite projections, then all possible combinations of the horizontal to the vertical preclusters are constructed and the cluster properties are determined in an analogous way to the single cluster case.

With its high spatial resolution of $\approx 20\ \mu$m the VLQ tracking device allows to determine the spatial resolution of the calorimeters which is then given by:

$$\delta_x = x_{track} - x_{calo} \qquad \delta_y = y_{track} - y_{calo}$$

Figure 4.9 shows the spatial resolution of the upper (left) and the lower (right) VLQ calorimeter. The resolutions of the y-coordinate are shown in the upper diagrams whereas the resolutions of the x-coordinate are shown at the bottom. The data distributions (points) are well described by the simulation (shaded histogram). The parameters of a gaussian distribution fitted to the data distributions are also shown in the plots. The resolution of the y-coordinate is ≈ 0.2 mm and of the x-coordinate 0.8 mm.

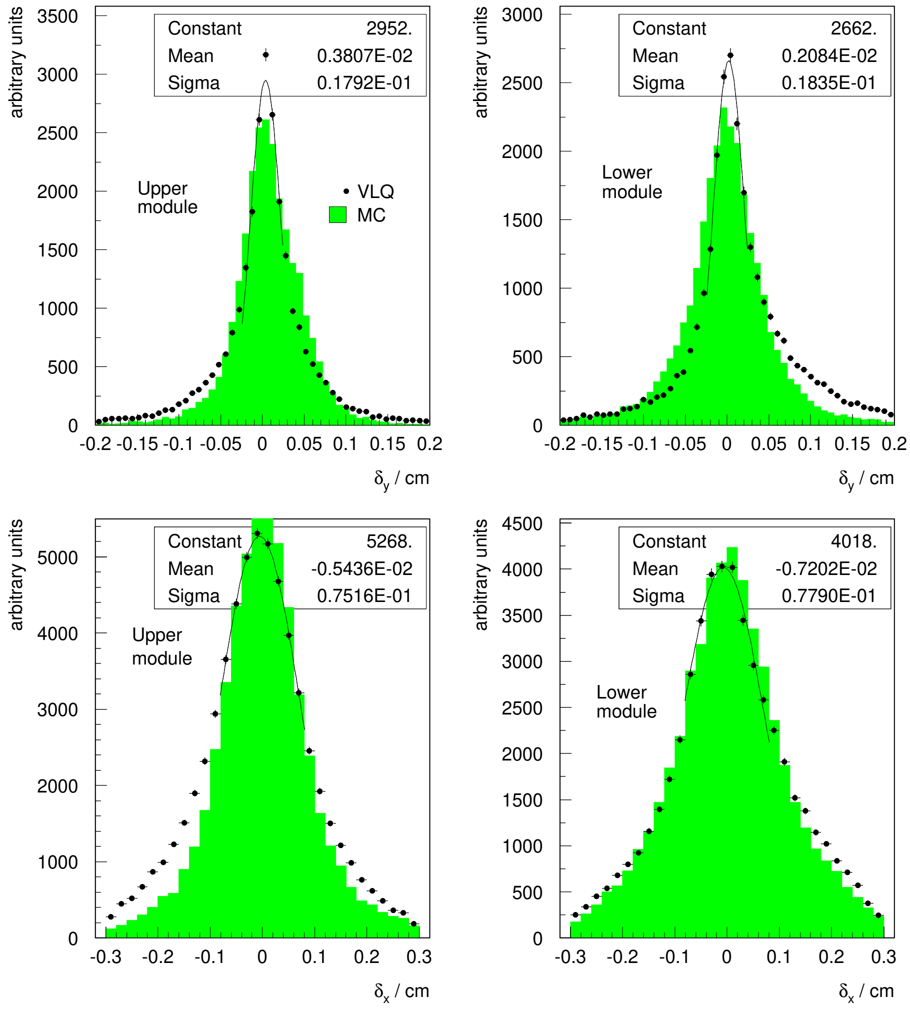

Figure 4.9: *The resolution of the y-coordinate (top) and for the x-coordinate (bottom) for the upper calorimeter (left) and for the lower calorimeter (right) are shown in data (points) and MC (shaded histogram).*

4.2.1 Energy Calibration

A calibration of the calorimetric response is needed in order to match the amplitude of the readout signals in units of ADC[5] counts to the energy of the detected particle in units of GeV. The relation between readout signal S and particle energy E would be linear for a "perfect" detector: $E = C \cdot S$ with C the so-called calibration factor. Due to detector effects e.g. leakage, aging etc. this calibration factor may depend on several parameters:

$$E \;=\; C(c_i, x, y, t) \cdot S$$

- c_i: the response to a certain energy deposition may vary from channel to channel due to the production tolerance of the scintillator material and of the preamplifiers or the optic coupling between scintillator and wavelength shifter.
- x, y: the calibration factor depends on the impact position of the detected particle. At the edges of the calorimeter part of the electromagnetic shower is lost (leakage). Additionally the scintillation light produced in the active material at the impact position of the particle is attenuated on the way to the wavelength shifter (so-called light attenuation).
- t: the calibration may be time dependent due to aging effects of the scintillator material under the intense synchrotron radiation of the e beam. As this analysis is carried out with data from a short period of four weeks at the end of 1999, no large variation of the calibration is expected. On a longer time scale the time dependence of the calibration has to be taken into account.

Furthermore the calibration factors should be independent of the energy of the detected particle. This behaviour will be verified in independent calibration tests with ρ^0 mesons and QED Compton events.

A preliminary calibration was performed with data taken in a test beam setup at the DESY III synchrotron at the end of 1997. Both calorimeters were tested with an electron beam in an energy range of 1-6 GeV. Additionally the impact position of the electrons on the surface of the calorimeters could be varied in order to scan both devices. The calibration procedure and the results of these measurements are presented in [27]. As the energy of the electron beam was limited to 6 GeV the accuracy of this preliminary calibration is restricted to the region of low electron energies in ep scattering at HERA. The final calibration factors are determined in situ in H1. The calibration procedure is based on the data set described in 6.1 and is divided into two steps.

Channel-to-channel Calibration

The first step of the calibration corrects for channel dependent effects. One selects events in a restricted energy range and varies the response of each channel in an iterative procedure

[5] Analog to Digital Converter

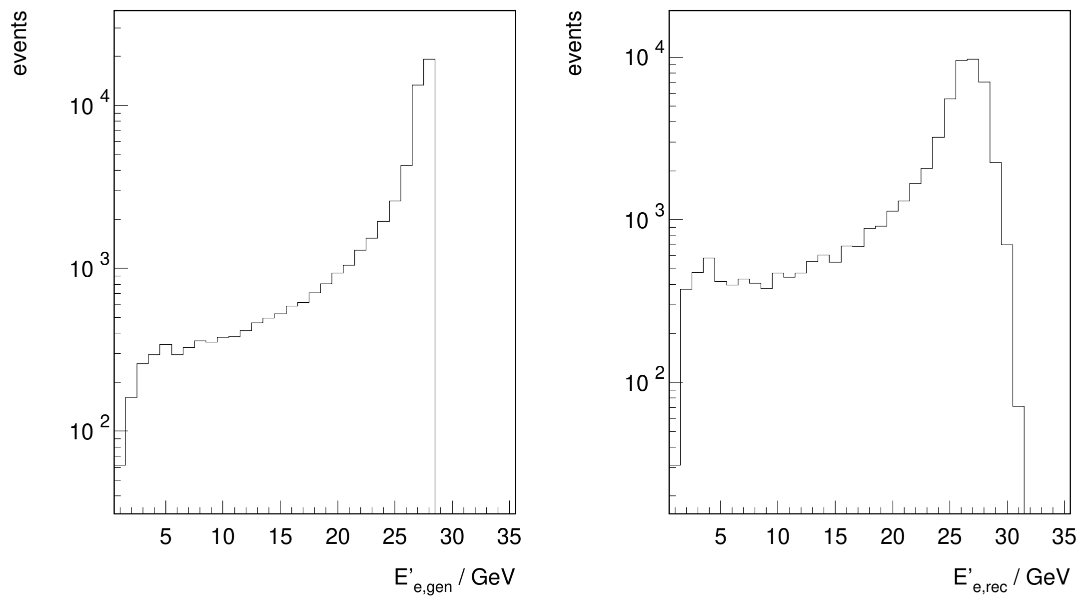

Figure 4.10: *Energy distribution of the scattered electron in the Monte Carlo* `PHOJET` *before the simulation of the detector response $E_{e,gen}$ (left) and after the simulation $E_{e,rec}$ (right). Both distributions show a maximum at large energy values for the scattered electron, the so-called kinematic peak.*

until a uniform response of all channels is reached.

So-called kinematic peak events are best suited for this procedure due to several reasons: the cross section reaches its maximum value at low y (therefore kinematic peak) and thus guarantees a large data sample. Low y corresponds to high electron energies at very large scattering angles (see section 2.3) and therefore the energy deposition in the calorimeter is large. Figure 4.10 shows the energy distribution of the scattered electron before (left) and after (right) the simulation of the detector response. One sees the kinematic peak at large values of the electron energy in both distributions. Finally a kinematic peak data set is practically free of photoproduction background[6]. The following selection criteria for kinematic peak events are applied to the data set:

- exactly one cluster with an energy above 20 GeV is reconstructed in the calorimeter
- in the VLQ phase space events at the kinematic peak show very low hadronic energy in the main calorimeters of the H1 detector. Therefore a cut on the inelasticity of the hadronic final state is done: $y_{had} < 0.05$
- no single diode hit was found in the calorimeter
- the impact position of the electron is in the following range:

[6]The contribution from photoproduction background becomes relevant at high y.

– $|x| < 0.5$ cm relative to the middle of the calorimeter for the calibration of the vertical channels

– $2 \text{ cm} < y < 3$ cm relative to the edge of the calorimeter nearest to the beam for the calibration of the horizontal channels

Figure 4.11 shows the principle of the channel-to-channel calibration procedure. The procedure is carried out separately for the vertical and the horizontal scintillator arrays. As mentioned above, the vertical arrays are calibrated with events with an impact position in the middle of the calorimeter (shaded vertical band in the left diagram). For the calibration of the horizontal arrays, events are selected in the horizontal band as shown in the right diagram. The asymmetric selection of events is necessary to avoid the shadowing by the insert of the SPACAL, indicated in figure 4.11. The restriction of the impact position

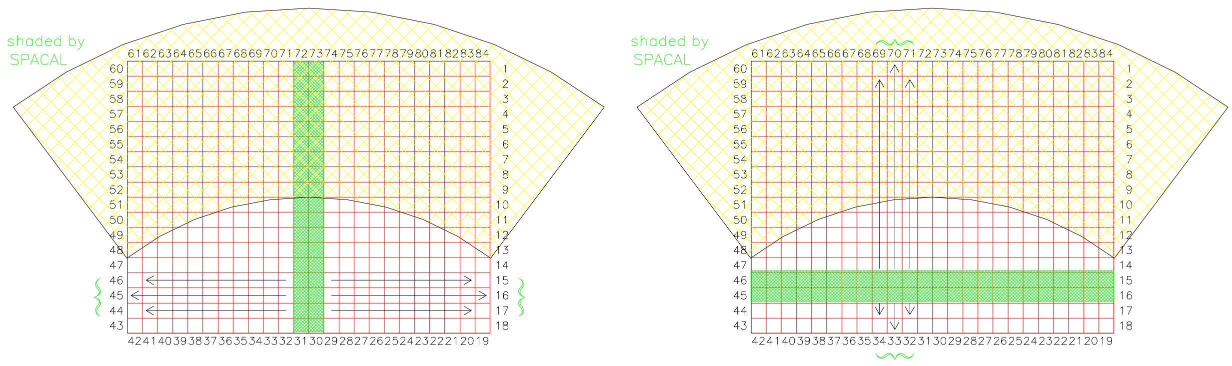

Figure 4.11: *Channel-to-channel calibration procedure for the vertical (left) and for the horizontal scintillator array (right). The channels are numbered [1:84]. For the calibration procedure, events inside the gray bands are selected.*

guarantees that the distance traveled by the scintillation light from the impact position to the wavelength shifter is constant in order to avoid light attenuation effects which would decrease the accuracy of the channel-to-channel calibration. The calibration procedure is explained by the following example. In order to calibrate channel 16, one selects all events with the maximum energy deposition in this channel. One sums up the energies E_j of the neighbouring channels[7] $E_{16}^n = \sum_{j=15}^{17} E_j$ for each event n. One calculates then the mean energy deposition over the whole data sample of N events: $\overline{E}_{16} = 1/N \sum_{n=1}^{N} E_{16}^n$. This procedure is repeated for all 84 channels of a calorimeter module. Figure 4.12 shows the mean energy response $\overline{E}_i$ of each channel i with the preliminary calibration. The left (right) plot shows the distribution for the upper (lower) module. The channel numbering is done clockwise starting at the calorimeter edge far from the beam. No energy response is measured

[7]For channels at the edge of the calorimeter one adds up twice the energy of the single neighbouring channel.

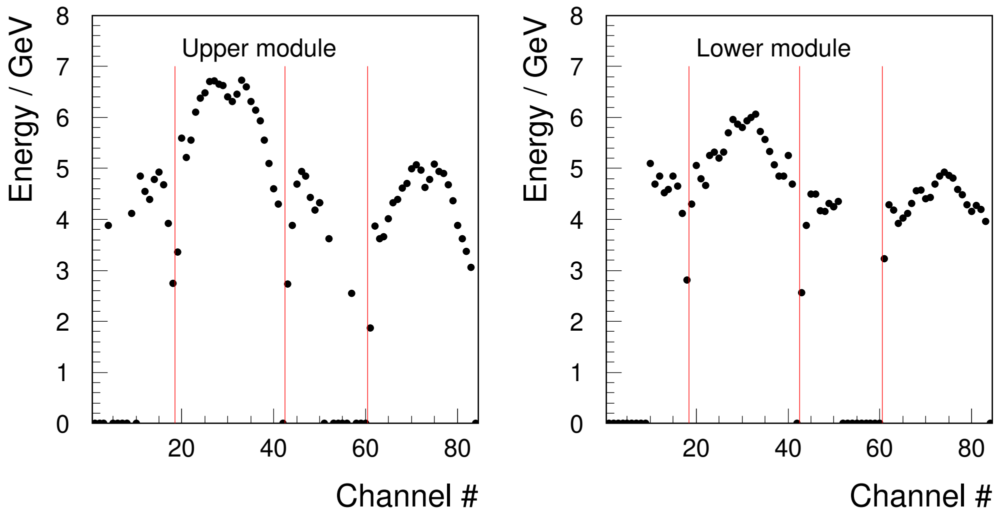

Figure 4.12: *Mean energy distribution of all channels for the upper (left) and the lower (right) module with the preliminary calibration from the test beam.*

for the areas covered by the SPACAL. The vertical lines delimit the edges of the scintillator arrays, the vertical arrays consisting of $N_v = 18$ and the horizontal ones of $N_h = 24$ channels. The horizontal arrays show a different overall energy level for all channels which is caused by the fact that the light attenuation for the upper horizontal array (channel 61-84) is larger than for the lower horizontal array (channel 19-42) due to the different distances for the light to travel, as indicated by the arrows on the right hand side in figure 4.11. The mean energy deposition for each array is calculated $E_{\mathrm{mean}} = 1/N_{\mathrm{v,h}} \sum_{i=1}^{N_{v,h}} \overline{E}_i$ and subsequently a calibration factor c_i for each channel is determined: $c_i = E_{\mathrm{mean}}/\overline{E}_i$. The whole procedure is then repeated with these new channel dependent calibration factors applied before the reconstruction of the calorimeter clusters. After six iterations a uniform energy response for all channels in an array is achieved, see Figure 4.13. For each scintillator array the channels show an uniform energy response, except the channels at the edges of the scintillator arrays where the leakage losses are too large to be compensated. The calibration factors for these edge channels are set to 1 at each iteration.

Kinematic Peak Calibration

The calibration factors determined in the channel-to-channel calibration are applied before the cluster reconstruction. As a result the energy response of all channels in an array are uniform. In the second step of the calibration procedure the absolute energy scale as well as the position dependent correction for leakage and light attenuation effects will be determined. Once again one selects kinematic peak events with the following criteria:

- exactly one cluster with an energy above 20 GeV is reconstructed in the calorimeter

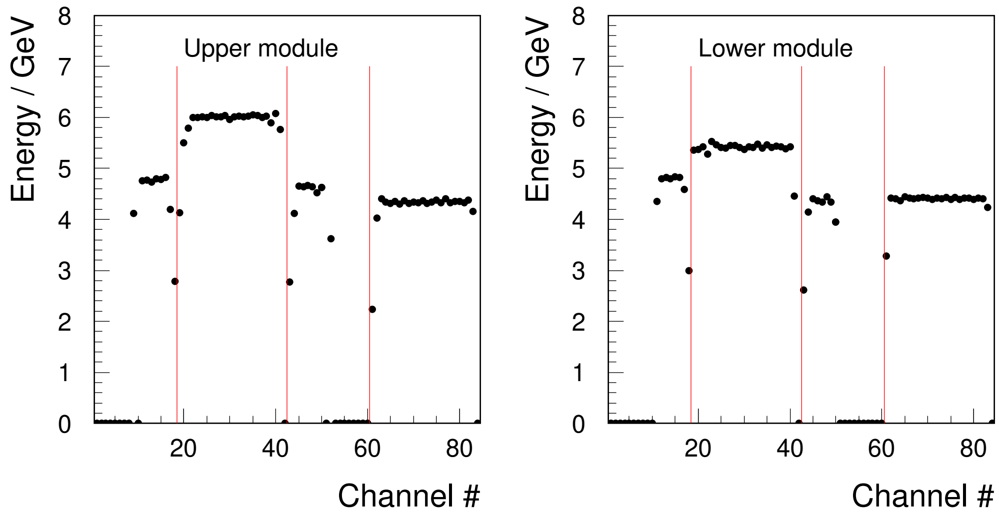

Figure 4.13: *Mean energy distribution of all channels for the upper (left) and the lower (right) module with the channel-to-channel calibration after six iterations.*

- in the VLQ phase space events at the kinematic peak show very low hadronic energy in the main calorimeters of the H1 detector. Therefore a cut on the inelasticity of the hadronic final state is done: $y_{had} < 0.05$
- no single diode hit was found in the calorimeter
- if the central tracker of the H1 experiment has reconstructed the z position of the vertex, a cut on the z_{vtx} is done: -35 cm $< z_{vtx} <$ 35 cm
- the energy in each tagger (ET44, ET and photon tagger) does not exceed 2 GeV

The surface of the calorimeter is divided in x-y bins. For the bins close to the beampipe where the cross section and therefore the number of events is large, a small bin size is chosen, while for the bins further away from the beam, larger bin sizes are chosen. For each bin j the mean of the kinematic peak energy spectrum $\overline{E}_j^{kp}$ is then determined by fitting a gaussian distribution to the energy distribution. The calibration factor c_j for bin j is calculated by: $c_j = \overline{E}_{MC}^{kp}/\overline{E}_j^{kp}$ where $\overline{E}_{MC}^{kp}$ denotes the mean of the kinematic peak distribution in the Monte Carlo simulation. $\overline{E}_{MC}^{kp}$ has been determined to be 27.1 GeV. This procedure is only performed if more than 100 events were reconstructed in a bin to guarantee a statistically safe behaviour, otherwise the calibration factor for this bin is set to 1.

Figure 4.14 shows the result of the kinematic peak calibration for a given bin j. The dashed line indicates the energy distribution of kinematic peak events before the above described calibration step with its mean value at ≈ 24 GeV. After the calibration procedure the resulting energy distribution is shown by the solid line. The parameters of a gaussian distribution fitted to the energy spectrum are shown. The mean value amounts now to

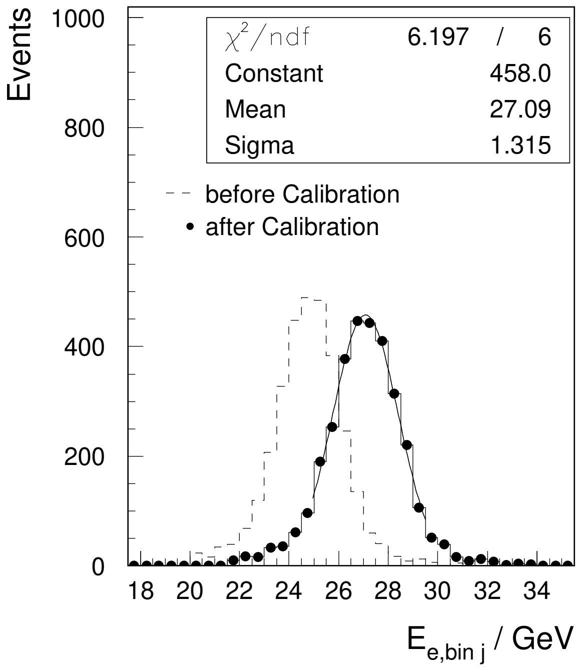

Figure 4.14: *Energy distribution of kinematic peak events before (dashed line) and after (points) the kinematic peak calibration for a given bin j. The parameters of a gaussian fit to the distribution are given.*

27.059 GeV, which is close to the value predicted by the Monte Carlo simulation, see figure 4.15.

The energy distribution resulting from the kinematic peak calibration in comparison with the simulated Monte Carlo events for the whole fiducial area is shown in figure 4.15. The dashed line indicates the energy distribution before the kinematic peak calibration while the points show the calibrated distribution. The simulated Monte Carlo is represented by the shaded histogram. The right diagram shows the distribution for the upper module and the left diagram for the lower module. Except for the tails of the distributions the data are well described by the simulation. The parameters of a gaussian fit to the data distribution are shown. For both calorimeter modules the resolution of the electromagnetic energy measurement at the kinematic peak is determined to be $\approx 5.5\%$, comparable to the value measured in [35]

The calibration of the VLQ calorimeters is checked with a sample of elastic ρ^0 events. The ρ^0 produced in the ep collision decays into two charged pions π^+ and π^-:

$$ep \rightarrow ep\rho^0 \qquad \rho^0 \rightarrow \pi^+\pi^-$$

The decay products of the ρ^0 meson can be detected in the central region of the H1 experiment while the scattered electron is detected in the VLQ spectrometer. Using energy and momentum conservation, the energy of the scattered electron can be determined by the

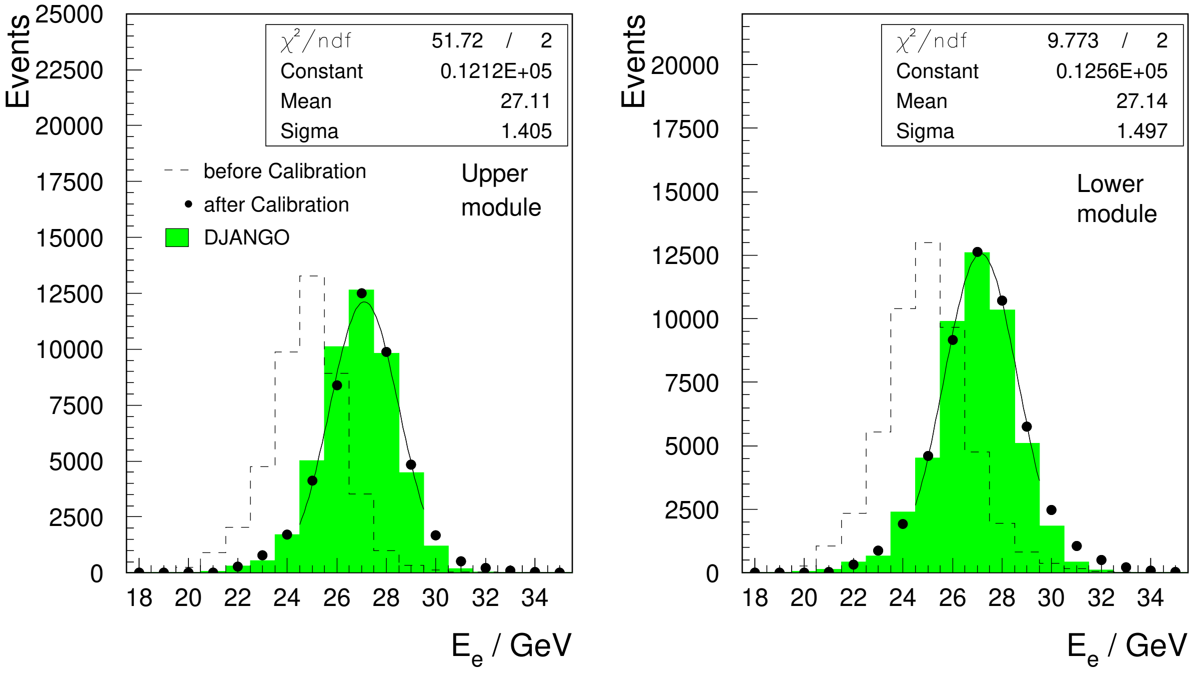

Figure 4.15: *Energy distribution of kinematic peak events before (dashed line) and after (points) the kinematic peak calibration for data (points). The shaded histogram shows the energy distribution for the simulated Monte-Carlo events. Distributions are given for the upper module (left) and the lower (right) module. The parameters of a gaussian fit to the data distributions are indicated.*

following equation:

$$E_e^{\pi\pi} = \frac{2E_0 - \sum_{i=1}^{2}(E_i - P_{z,i})}{1 - \cos\theta_e}$$

where i denotes the final state pions, E_i resp. $P_{z,i}$ the energy resp. the z-component of the momentum of the pions, E_0 the energy of the incoming electron and θ_e the scattering angle of the electron measured with the VLQ spectrometer.

The selection criteria of the elastic ρ^0 mesons are summarized in table 4.1 [54]. Figure 4.16 (left) shows the invariant mass distribution of the two pion final state for data and MC after the selection cuts. A peak at the mass of the ρ^0 meson $m_\rho = 770$ MeV is visible. In the right plot of figure 4.16 the ratio of the energy of the scattered electron measured by the VLQ calorimeters E'_e to the value reconstructed from the final state pions $E_e^{\pi\pi}$ is shown. The mean values of the distributions are also given. Data and MC show a good agreement within 0.5%.

The ρ^0 sample allows for a check of the calibration procedure at the kinematic peak. In order to guarantee for a correct calibration at lower energies, the linearity of the calorimetric response is verified using an elastic QED Compton event sample, see section 4.2.2. The final state of elastic QED Compton events, composed of an electron and a photon, is detected simultaneously in both VLQ calorimeters. Each particle carries approximatively half of

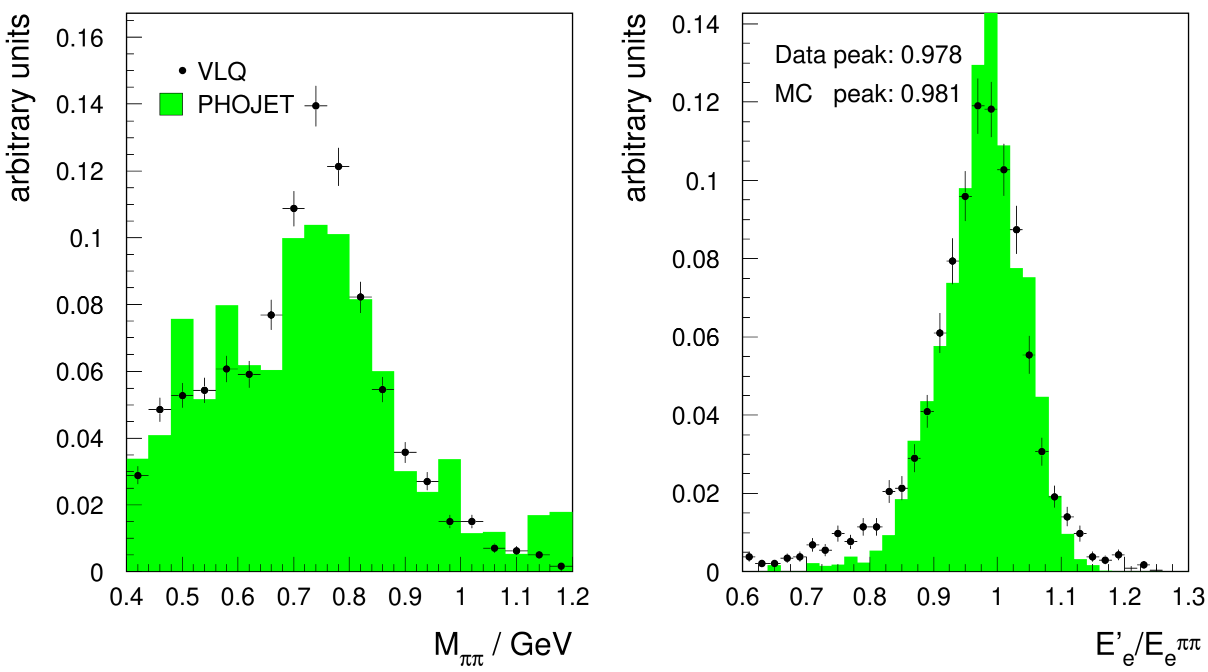

Figure 4.16: *The left plot shows the reconstructed mass of the two pion final state for data (points) and MC (shaded histogram). The ratio of the electron energy measured with the VLQ spectrometer E'_e to the electron energy reconstructed from the final state pions $E_e^{\pi\pi}$ is given in the right plot.*

Selection criteria	Purpose
electron candidate inside the VLQ fiducial area	E'_e and θ_e measurement
2 central tracks with opposite charge and $20^\circ < \theta_{track} < 160^\circ$ which were not identified as muons	ρ^0 identification
energy in the LAr calorimeter: $E_{LAr} < 2.5$ GeV	background rejection
reconstructed ϕ mass: $M_\phi > 1.04$ GeV	background rejection

Table 4.1: *Selection criteria for the ρ^0 sample.*

the electron beam energy of 27.5 GeV. The left plot in figure 4.19 shows the sum of the energy depositions in the upper and the lower module for data and `COMPTON` MC. The data distribution is well described by the MC distribution and the agreement between the peak values of data and MC is within 1% which demonstrates the linearity of the calorimetric response.

4.2.2 Alignment

The exact knowledge of the position of a subdetector relative to H1 coordinates and thus to the beam axis is essential to an accurate reconstruction of the kinematic variables, see section 2.3. The procedure to determine the position of a subdetector is called alignment. In the case of the VLQ spectrometer a method using the Wide Angle Bremsstrahlung process $e\,p \;\rightarrow\; e'\,p\,\gamma$, also called QED Compton process, was developed in [49]. Figure 4.17 shows the corresponding Feynman diagrams for the QED Compton process. If the momentum transfer q_1 is large compared to $q_2 \simeq 0$ the angle between electron and photon is large and in a small fraction of the events electron and photon are simultaneously detected in the upper resp. lower module of the VLQ spectrometer. Furthermore in the elastic case of the QED Compton process, electron and photon are back to back in azimuth thus providing a redundant determination of the event kinematics.

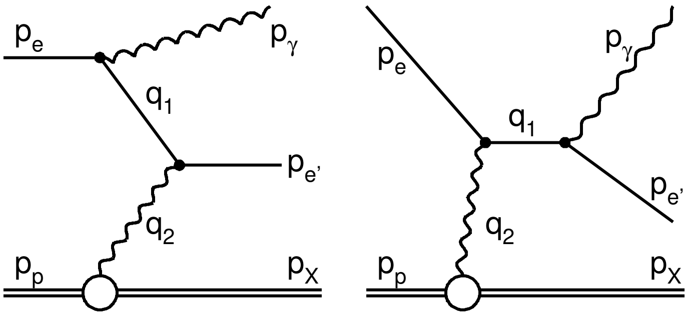

Figure 4.17: *Diagrams of the Wide Angle Bremsstrahlung process.*

Selection of QED Compton Events

QED Compton events are characterized by a simultaneous energy deposition in the upper and the lower module of the VLQ spectrometer. Over the whole data taking period of the VLQ the dedicated QED Compton subtrigger s47 `VLQ_low_AND`, see section 5.1.2, was active requiring for both calorimeters an energy deposition above the low threshold of ≈ 6 GeV and no single diode hit on level 1 of the trigger system. The rate of the subtrigger s47 recorded during standard data taking was in the range of 0.02 - 0.07 Hz and no prescaling to s47 was applied. A further reduction of the event rate by a factor of 7 was achieved on trigger level

4 by applying several cuts on the reconstructed information of the VLQ calorimeters, see table 4.2. Besides the obvious conditions that the event is triggered by s47 on trigger level

L4 Selection
s47 on
$E_1 > 0$ GeV & $E_2 > 0$ GeV
16 GeV $< E_1 + E_2 <$ 38 GeV
$\lvert\Delta\phi - 180°\rvert < 20°$

Table 4.2: *Selection criteria for QED Compton events on trigger level 4.*

1 and that an energy deposition is recorded in both modules, a soft cut on the sum of the energy depositions in the VLQ calorimeters is applied. The energy sum for QED Compton events is expected to be ≈ 27.5 GeV. The last cut on the acoplanarity[8] $\Delta\phi = |\phi_1 - \phi_2|$ rejects events which are not roughly back-to-back in azimuth.

In order to further reduce the amount of background events, several offline cuts are applied on the fully reconstructed event information.

- To achieve a full containment of the electromagnetic cluster in the calorimeter, the impact position of the electron has to be at a minimal distance of 0.95 cm to the edge of the calorimeter in x and y direction.

- The energy deposited in the electron taggers ET and ET44 and the photon detector PD does not exceed 2 GeV. This cut reduces the amount of photoproduction background and rejects events where a photon has been radiated from the initial state of the electron, the so called ISR[9] events.

$$E_{\mathrm{ET}} < 2\mathrm{GeV} \qquad E_{\mathrm{ET44}} < 2\mathrm{GeV} \qquad E_{\mathrm{PD}} < 2\mathrm{GeV}$$

- In the case of elastic QED Compton events, the proton escapes through the beampipe and is not detected by the H1 detector. To reduce beam-gas and beam-wall induced events with large hadronic activity in the H1 detector, a cut on y reconstructed with the Hadron Method is applied:

$$y_{\mathrm{had}} < 0.05$$

In figure 4.18 the impact of the y_{had} cut is shown on the energy sum and the acoplanarity distributions. The amount of background at low energies and at large values of the

[8] On level 4 a coarse alignment of the calorimeters is applied during the calculation of the azimuthal angle of the cluster in the VLQ.

[9] Initial State Radiation

acoplanarity is heavily reduced. Events induced by the QED Compton process with an energy sum of $\approx$ 27.5 GeV and $\Delta\phi \approx 0$ are only slightly affected by this cut. As the alignment procedure has not been carried out yet, the true position of the VLQ modules relative to the beam axis is unknown and the position values have been taken from the technical drawings:

$$\begin{array}{lcclccc} \mathrm{x}_1 & = & 0 & ; & \mathrm{y}_1 & = & 3.6 \\ \mathrm{x}_2 & = & 0 & ; & \mathrm{y}_2 & = & \text{-}3.6 \end{array}$$

$\mathrm{x}_{1,2}$ measures the distance of the middle of the calorimeter to the y axis and $\mathrm{y}_{1,2}$ the distance of the inner edge of the modules to the beam axis. The accuracy of these values is in the range of several millimeters. The acoplanarity distribution peaks at a value of $\approx 4°$ clearly indicating that the true position of the modules is shifted relative to the values in the technical drawings. Thus an alignment procedure which will be discussed in the next section is necessary to determine the precise position of the modules.

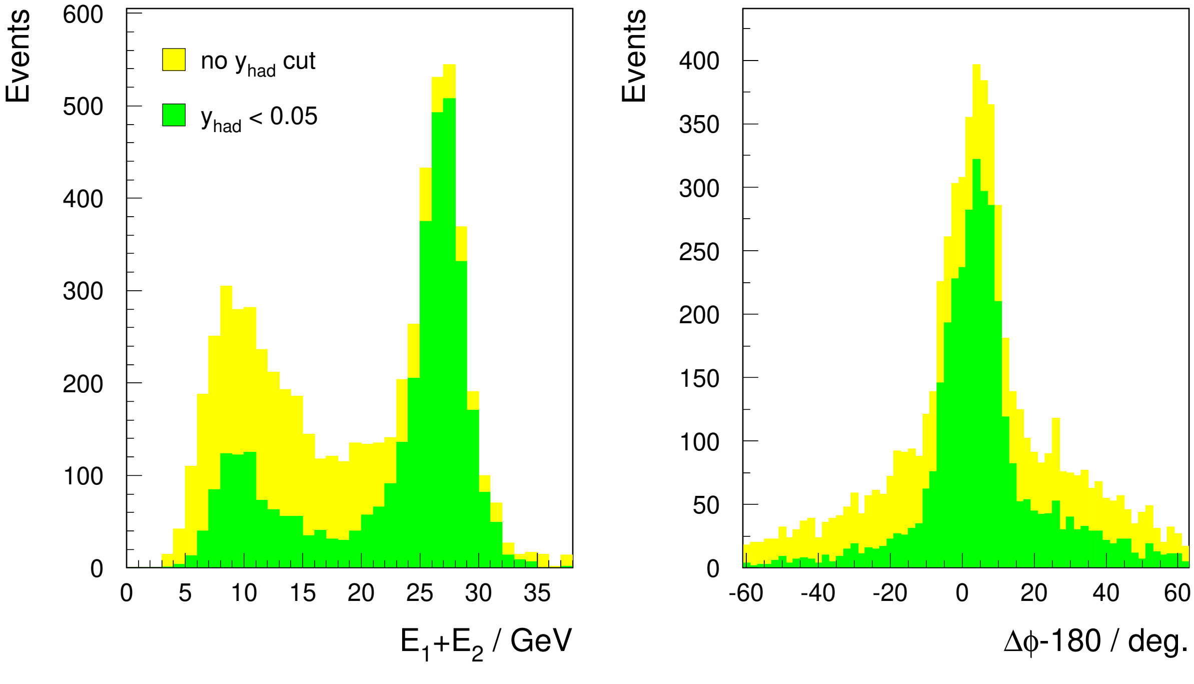

Figure 4.18: *Energy sum (left) and acoplanarity (right) of the QED Compton event sample before the alignment procedure. The distributions are shown before (light area) and after (dark distribution) the cut on* $y_{\mathrm{had}} < 0.05$.

- A small fraction of events with a low energy sum and thus resulting from background processes survive the above cuts. A cut on the energy sum finally rejects these events:

$$20 \text{ GeV} < \mathrm{E}_1 + \mathrm{E}_2 < 38 \text{ GeV}$$

- Furthermore a cut on the acoplanarity $\Delta\phi = |\phi_1 - \phi_2|$ is applied:

$$|\Delta\phi - 180°| < 20°$$

- Due to energy and momentum conservation the transverse momentum $\vec{p}_\perp$ of the electron and the photon is balanced, where $\vec{p}_\perp$ is defined as follows:

$$\vec{p}_\perp = E \cdot \frac{\vec{r}}{|\vec{x}|}$$

with E the energy, $\vec{x}$ the vector of the cluster in coordinate space and $\vec{r}$ the distance of the cluster to the beam axis. The following cut on the balance of the $\vec{p}_\perp$ of electron and photon is required:

$$p_{\text{bal}} = \frac{|\vec{p}_{\perp,e} + \vec{p}_{\perp,\gamma}|}{|\vec{p}_{\perp,e}| + |\vec{p}_{\perp,\gamma}|} < 0.3$$

Figure 4.19 shows the final distributions for the energy sum and the acoplanarity after the application of the above selection criteria. The shaded area shows the corresponding distributions for the Monte Carlo generator `COMPTON` 2.00 [48], see section 3.1.3. As the position of the modules are known in the simulation, the MC distributions show the expected behaviour for an aligned VLQ spectrometer. The simulation shows a good description of the peak of the energy sum distribution, thus indicating a correct calibration of the VLQ calorimeters in data and MC, see section 4.2.1. Additionally the linearity of the calorimeters is verified within 1%. The MC-distributions are normalized to the number of events in data. The data show an excess at the edges of the distributions, which may be due to remaining background events. On the other hand the distributions of the acoplanarity and of the $\vec{p}_\perp$-balance (left plot in figure 4.20) show large discrepancies due to a misalignment of the modules in the data. Finally in the right plot of figure 4.20 the number of events as a function of the integrated luminosity is shown. The linear increase with the integrated luminosity indicates a stable behaviour of the QED Compton selection.

Alignment Procedure

The alignment procedure described in this section provides a position determination of the VLQ modules relative to the CJC and thus to the HERA laboratory frame for the e^+p data taking period (July to December 1999). Before and after this data taking period the VLQ spectrometer was removed from the H1 detector to undergo maintenance. For these data taking periods the alignment procedure has to be performed separately.

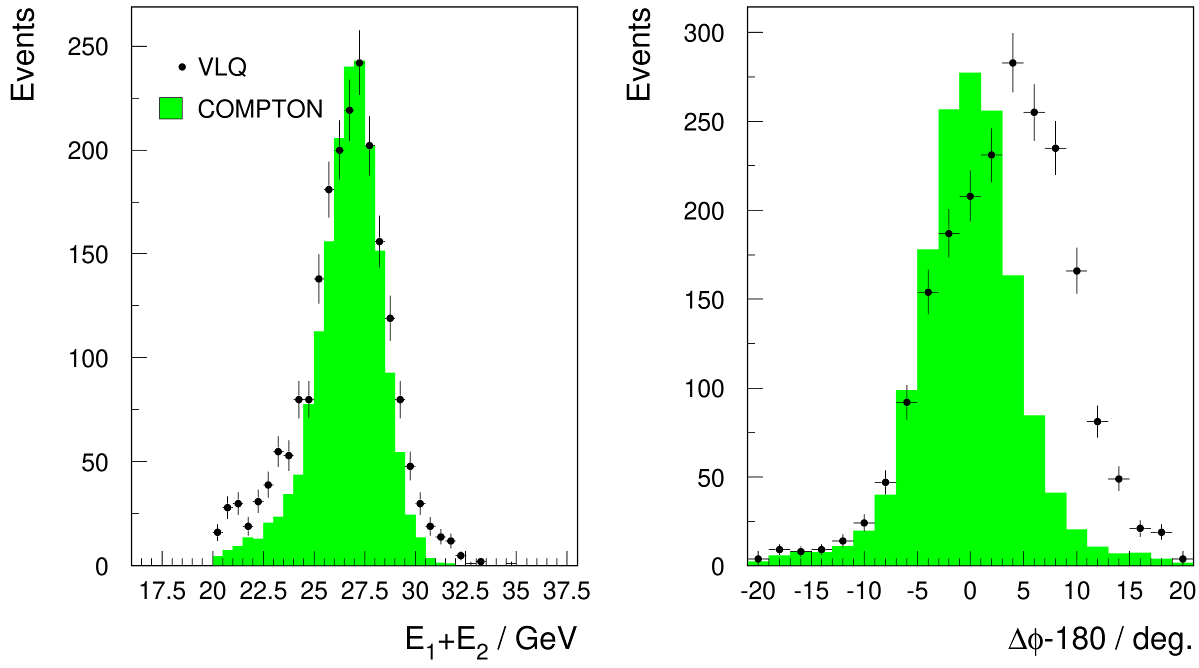

Figure 4.19: *Energy sum (left) and acoplanarity (right) of the final QED Compton event sample for data (points) and MC (shaded distribution) before the alignment procedure.*

The alignment procedure takes advantage of the redundant determination of the event kinematics for elastic QED Compton events. As electron and photon of the final state are coplanar a clean measurement of the impact position of one of the particles, either electron or photon, provides a prediction of the one degree of freedom left i.e. the scattering angle of the second particle. As the z-position of the VLQ calorimeters is known, the impact position of the second particle may be calculated.

The coordinates x_{true} and y_{true} of a cluster in a VLQ calorimeter relative to the H1 laboratory frame are calculated as follows:

$$\begin{aligned} x_{true} &= x_{calo} + \Delta x_{beam} + \Delta x_{align} \\ y_{true} &= y_{calo} + \Delta y_{beam} + \Delta y_{align} + \Delta y_{VLQ} \end{aligned}$$

- x_{calo} and y_{calo} describe the cluster coordinates relative to the internal coordinate system of the calorimeter. The coordinates in units of wavelength shifters are provided by the calorimeter reconstruction for each calorimeter.

- Δx_{beam} and Δy_{beam} denote the influence of the tilt and the shift of the beam. The tilt ($sx0$ and $sy0$) and the shift ($vx0$ and $vy0$) are measured by the central jet chambers

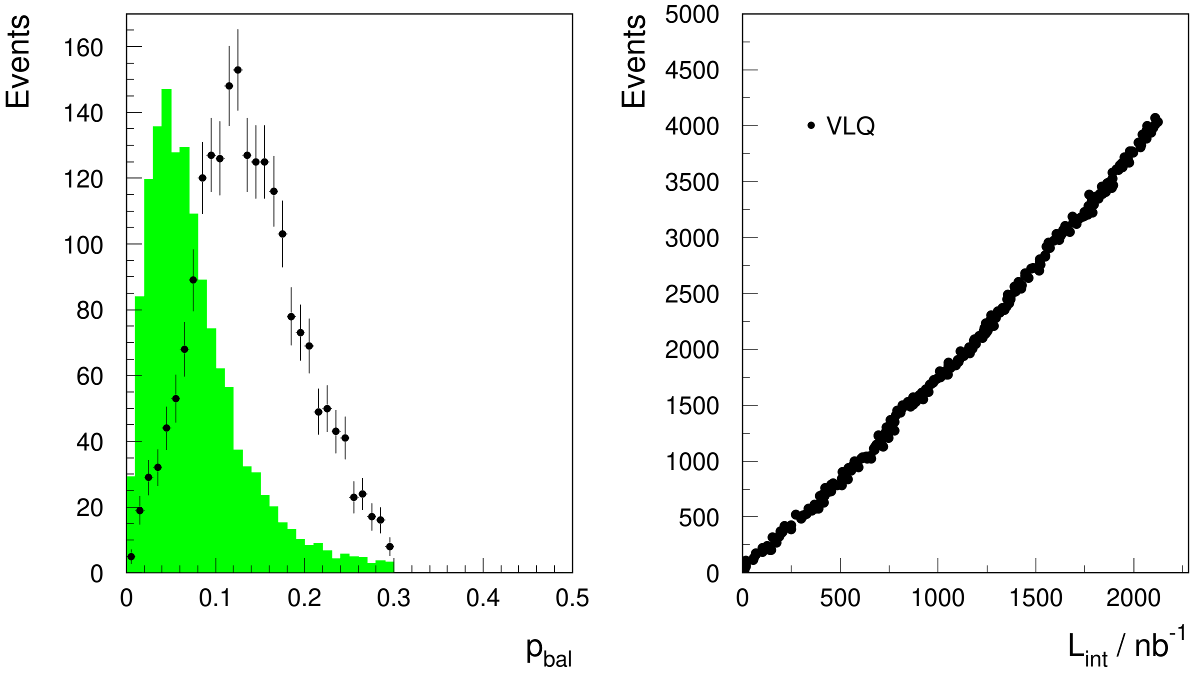

Figure 4.20: *$\vec{p}_\perp$-balance for data (points) and MC (shaded distribution) before the alignment procedure and number of elastic QED Compton events as a function of the integrated luminosity*

at $z = 0$ for each run:

$$\begin{aligned} \Delta x_{beam} &= vx0 + \tan(sx0) \cdot z_{VLQ} \\ \Delta y_{beam} &= vy0 + \tan(sy0) \cdot z_{VLQ} \end{aligned}$$

with z_{VLQ} the distance in z direction of the VLQ calorimeters from the origin $z = 0$.

- The position relative to the central jet chambers is given by Δx_{align} and Δy_{align}. The goal of the alignment procedure consists in determining the correct values for Δx_{align} and Δy_{align} for each calorimeter.

- Δy_{VLQ} is measured by the optical position measurement system of the moving mechanism. Figure 4.21 shows the run dependent measurement of Δy_{VLQ} for the upper module over the whole minimum bias data sample. The absolute value of Δy_{VLQ} is arbitrary. At the beginning of a luminosity fill the modules are moved into data taking position. For adjacent runs belonging to one luminosity fill, figure 4.21 shows that Δy_{VLQ} slowly decreases, indicating that the module sinks. This behaviour is due to a leak in the hydraulics of the moving mechanism. At the end of each luminosity fill the modules are retracted and remain behind the iron yoke until the next fill.

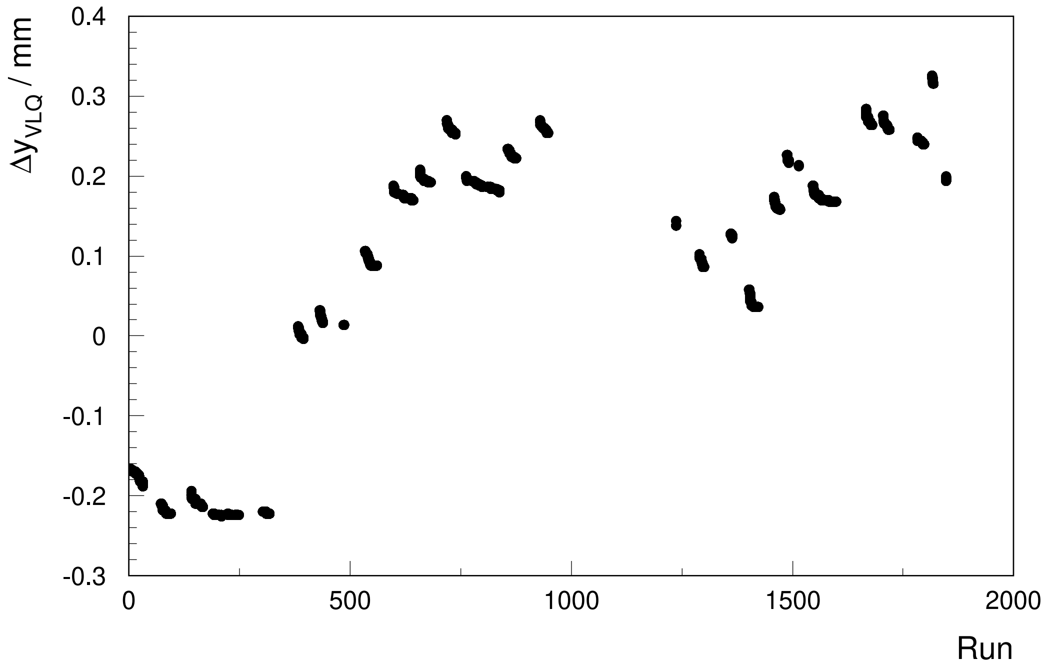

Figure 4.21: *Run dependent measurement of Δy_{VLQ} for the upper module.*

The position of the VLQ modules is given by a set of four parameters (Δx_{align} and Δy_{align} for each module). These parameters will be determined in a fitting procedure based on the χ^2 minimization method. The first step of the alignment procedure consists of using the values from the technical drawings for Δx_{align} and Δy_{align} and subsequently calculating the particle impact position relative to the laboratory frame for each event of the QED Compton sample. The acoplanarity $\Delta\phi$ is determined for each event by:

$$\Delta\phi \;=\; |\phi_1 - \phi_2| \;=\; \left|\arctan\left(\frac{y_{true,1}}{x_{true,1}}\right) - \arctan\left(\frac{y_{true,2}}{x_{true,2}}\right)\right|$$

In the second step the χ^2 variable is calculated by:

$$\chi^2 \;=\; \sum_i \left(\Delta\phi - 180\right)^2$$

where the sum runs over all events i. In the last step the minimization of the variable χ^2 is performed by the program MINUIT [55] by varying Δx_{align} and Δy_{align}. The algorithm is based on Newton's minimization method. If the minimization procedure converges, a set of values for Δx_{align} and Δy_{align} is provided. The whole procedure is then repeated with the new parameters as starting values in the second iteration. Usually several iterations (in this case six iterations) of this fitting procedure are necessary until the results converge to a final set of parameters.

Unfortunately if all four parameters are determined simultaneously the minimization procedure diverges. The minimization fails because the acoplanarity of the events is achieved by shifting the upper module to $y = +\infty$ and the lower module to $y = -\infty$, resulting in $\Delta\phi = 0$ and thus $\chi^2 = 0$ for each event. This non-physical result of the fit can be avoided by fixing the distance Δy between both modules. The y-position of the upper module $\Delta y_{align,1}$ is determined by the fitting procedure, whereas the y-position of the lower module is determined by the relation $\Delta y_{align,2} = \Delta y_{align,1} - \Delta y$. The distance between the modules in data-taking position is measured to be:

$$\Delta y = 7.85 \pm 0.04 \text{ cm}$$

After six iterations the following result for the alignment of the VLQ modules during the e^+p data taking period (July to December 1999) is obtained for a 3-parameter fit-procedure:

$$\begin{array}{rclcrcl} \Delta y_{align,1} & = & 3.24 \text{ cm} & ; & \Delta x_{align,1} & = & \text{-0.03 cm} \\ \Delta y_{align,2} & = & \text{-4.61 cm} & ; & \Delta x_{align,2} & = & \text{-0.3 cm} \end{array}$$

The accuracy of the alignment procedure has been estimated to $\pm$ 0.5 mm, mainly given by the accuracy of distance measurement between the two modules. In figure 4.22 the behaviour of the fitting procedure is shown over all iteration steps. The difference of the parameter value Δ_i of iteration i to the final value Δ_{final} is shown. The minimization procedure converges after six iterations. The values obtained by the alignment procedure for this data taking period are roughly comparable to the results obtained in [49] for the preceding e^-p data taking period (January to April 1999). The slightly different alignment values are due to the fact that during the shutdown of HERA in the summer of 1999, the VLQ modules were removed from the H1 detector and later reinstalled.

Figure 4.23 shows the distributions of acoplanarity and $\vec{p}_\perp$-balance for the QED Compton sample with the result of the alignment procedure included in the position determination of the calorimeter clusters. The simulated events give a much better description of the data distributions than before the alignment of the VLQ modules, see figures 4.19 and 4.20, thus indicating a correct position determination.

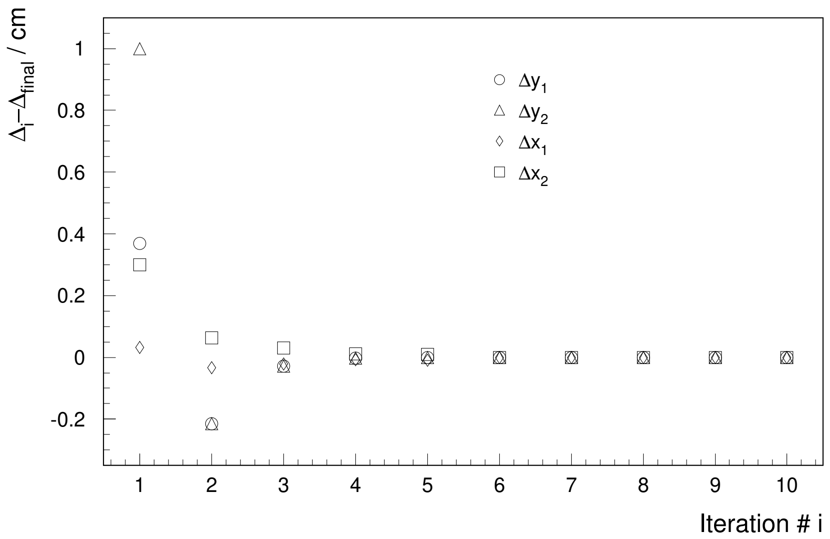

Figure 4.22: *The difference of the parameter value Δ_i of iteration i to the final value Δ_{final}. After six iterations all parameters converge.*

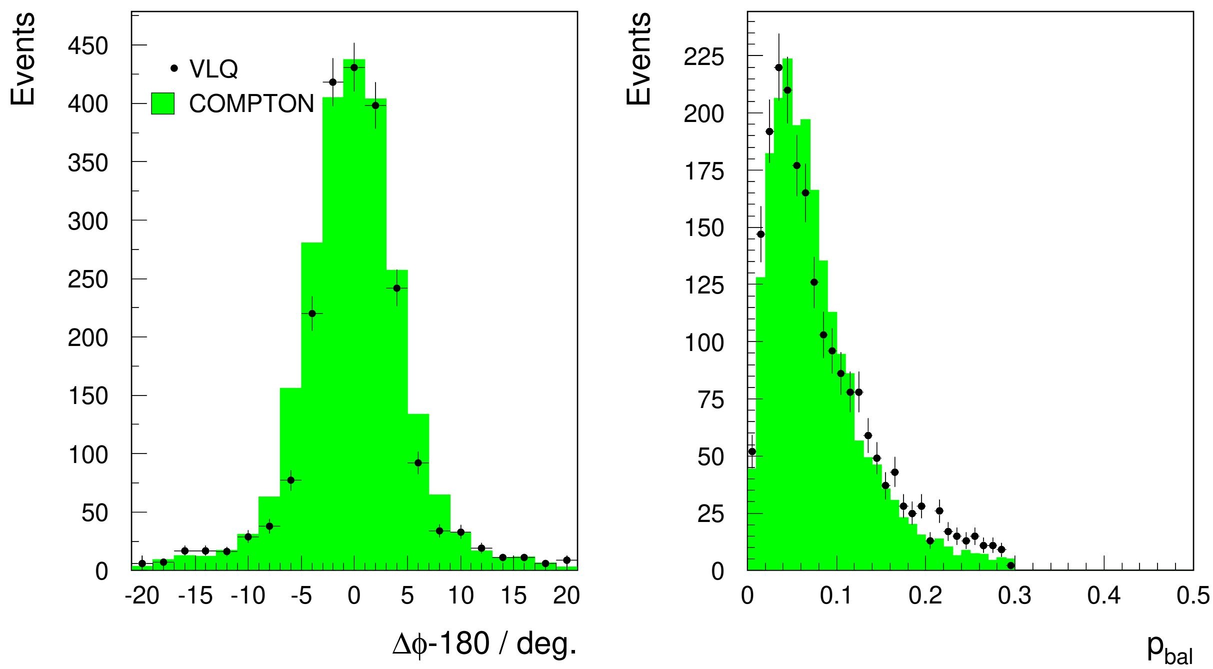

Figure 4.23: *Acoplanarity and $\vec{p}_\perp$-balance of the QED Compton event sample after alignment of the VLQ spectrometer.*

5
Efficiencies

The following chapter discusses in detail the implementation of the VLQ triggerelements and the trigger setup on level 1 during the data taking in 1999. Subsequently the efficiency of the VLQ triggers are determined. Finally the efficiencies of the requirements on the hadronic final state, trigger element `zVtx_T0` and offline vertex reconstruction, are outlined.

5.1 VLQ Trigger

The insertion of the VLQ spectrometer extends the acceptance of the H1 detector in the region of small electron scattering angles. It is thus necessary to implement an independent trigger signal based on energy depositions in the calorimeter modules.

5.1.1 VLQ Triggerelements

The VLQ trigger elements are based on the information delivered by the VLQ calorimeters. The readout channels of all four projections are summed up in groups of six, the so-called trigger segments. To avoid the splitting of energy depositions into two trigger segments, neighbouring segments are summed up again to build overlapping regions[1]. In the original design [27] this summing scheme should be carried out by the readout chips of the Front End electronics. Unfortunately due to coherent noise on the readout chip, this led to a trigger threshold of roughly 20 GeV, which is too high. A tolerable situation was reached by replacing the summing scheme on the front end electronics. In the new scheme the readout signals are summed up after they are transferred to the electronics trailer of the H1 experiment and thus the summing procedure is independent of the coherent noise on the trigger logic of the readout chip. Now only the 12 vertical readout channels closest to the beam on the left and on the right side of a calorimeter are combined to form two trigger segments with 9 readout channels each (T1, T2, T3 and T4 in figure 5.1). By summing up neighbouring segments (T1+T2 and T3+T4) an overlapping region of 6 channels is formed. The remaining six outer channels do not contribute to the trigger as this region

[1] The so-called sliding-window scheme.

Figure 5.1: *Schematic view of the sliding window scheme of the VLQ trigger for the upper module. The trigger segments T1 and T2 (T3 and T4) on the right (left) of the calorimeter each combine 9 readout channels with an overlapping region of 6 channels. The shaded area shows the region which is not included in the trigger.*

is shielded by the insert of the SPACAL, see shaded area in figure 5.1 (cf. also figures 6.2, 4.11). If the sum of the energy measured in opposite trigger segments (T1+T3; T2+T4) exceeds one of the following thresholds (`high`, `low` and `noise`) the according trigger element is set: `VLQ_top_high`, `VLQ_top_low` and `VLQ_top_noise` for the upper module and `VLQ_bot_high`, `VLQ_bot_low` and `VLQ_bot_noise` for the lower module. The energy values corresponding to the different trigger thresholds are approximatively 10 GeV for the `high` threshold, 6 GeV for the `low` threshold and 4 GeV for the `noise` threshold. A precise determination of the thresholds will be presented in section 5.2.2. Additionally due to the projective readout of the calorimeter, events with only a single diode hit in a calorimeter are suppressed by comparing the energy depositions on opposite sides of the modules (i.e. T1 and T3). If the energy deposition results from a particle hitting the calorimeter, the energy will be roughly equally distributed on both opposite trigger segments. If instead the energy deposition is solely due to a single diode, the energy will be concentrated in one trigger segment while the segment on the opposite side shows no response. In this case the trigger element `VLQ_top_SDE` will be set for the upper module and accordingly `VLQ_bot_SDE` for the lower module. The average rates of the VLQ trigger elements are shown in table 5.1. The rates decrease strongly with increasing trigger threshold. The rate difference between the upper and the lower module is explained by the alignment described in section 4.2.2. As the *ep* cross section decreases with increasing scattering angle, the upper module which is closer to the beam records higher trigger rates than the lower module.

Upper Module		Lower Module	
Triggerelement	Rate [Hz]	Triggerelement	Rate [Hz]
`VLQ_top_low`	1200	`VLQ_bot_low`	800
`VLQ_top_high`	550	`VLQ_bot_high`	500
`VLQ_top_noise`	1300	`VLQ_bot_noise`	1100
`VLQ_top_SDE`	470	`VLQ_bot_SDE`	430

Table 5.1: *Average rates of the VLQ trigger elements during the minimum bias run of 1999.*

Trigger	Definition
`VLQ_high_OR`	(`VLQ_top_high` && !`VLQ_top_SDE`) || (`VLQ_bot_high` && !`VLQ_bot_SDE`)
`VLQ_low_OR`	(`VLQ_top_low` && !`VLQ_top_SDE`) || (`VLQ_bot_low` && !`VLQ_bot_SDE`)
`VLQ_low_AND`	(`VLQ_top_low` && !`VLQ_top_SDE`) && (`VLQ_bot_low` && !`VLQ_bot_SDE`)
`VLQ_noise_OR`	(`VLQ_top_noise` || `VLQ_bot_noise`)

Table 5.2: *Definition of the VLQ trigger element combinations*

5.1.2 Level 1 Subtriggers

The information of all trigger elements is sent to the central trigger logic of the H1 experiment. Here the information of one or several subdetectors is combined to form so-called subtriggers, in order to select events from *ep* collisions and suppress background events. The definition of VLQ related combinations is listed in table 5.2.

- `VLQ_high_OR` and `VLQ_low_OR`: energy deposition above the high (low) threshold in the upper or in the lower module in the absence of a single diode hit.
  These trigger elements are intended to select inclusive *ep* events. In combination with several veto requirements they are used as subtriggers s46 and s49 in this analysis, see table 5.3.

- `VLQ_noise_OR`: energy deposition above the noise threshold in the upper or in the lower module.

- `VLQ_low_AND`: energy deposition above the low threshold simultaneously in both modules in the absence of a single diode hit.
  This trigger element, combined with veto requirements to form subtrigger s47 (see table 5.3), selects QED-Compton events which are characterized by a simultaneous energy deposition in both modules. The QED-Compton event sample is mainly used in the alignment procedure of the calorimeters, see section 4.2.2.

The left plot in figure 5.2 shows the development of the trigger rate of subtrigger s49 during lumi fill 2200. The decrease in rate is due to the decrease of luminosity over a lumi fill, caused

Inclusive Triggers			
Subtrigger	Definition	Veto	Rate [Hz]
s46	`VLQ_high_OR`	v:8 f:3	20 - 40
s47	`VLQ_low_AND`	v:8 f:2	0.06
s49	`VLQ_low_OR`	v:8 f:3	40 - 200

Table 5.3: *Definition and rates of VLQ related inclusive subtriggers on trigger level 1 without prescaling.*

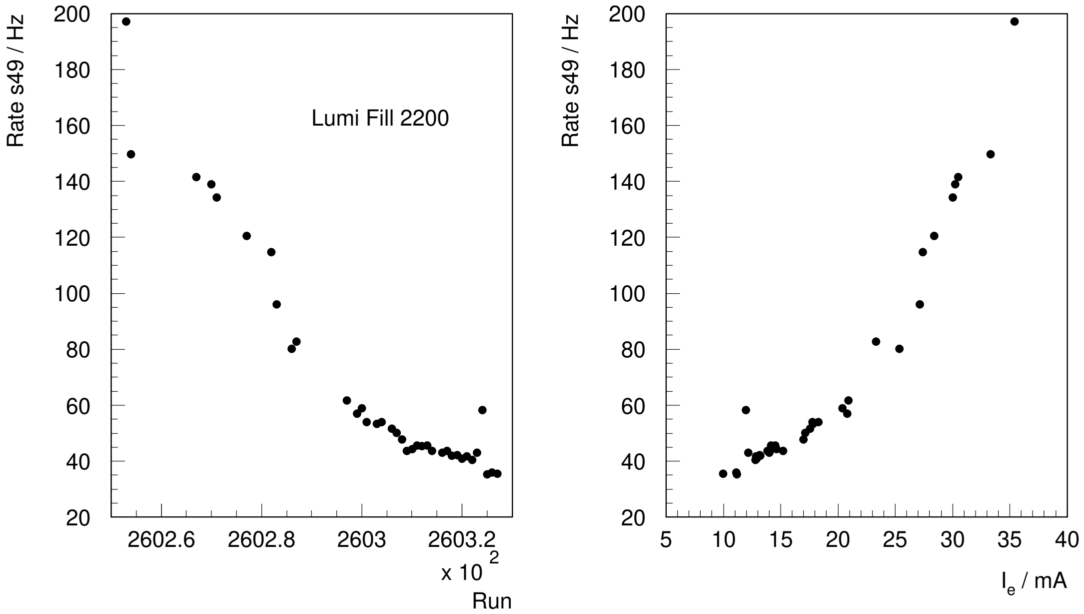

Figure 5.2: *Development of the rate of subtrigger s49 during lumi fill 2200 (left). Dependence of the rate of s49 on the electron beam current.*

by the continuous reduction of the beam currents. The right hand side in figure 5.2 shows the strong dependence of the rate of s49 on the electron beam current over the duration of lumi fill 2200. The change of slope is due to a run dependent prescaling of the subtriggers. The final inclusive subtriggers and their average rates before prescaling are shown in table 5.3. Experience with fully inclusive triggers as subtriggers s46 and s49 showed that the inclusive data samples were dominated by a large amount of background at low energy depositions in the VLQ calorimeters. As the event rate which can be stored by the H1 data acquisition is limited to 20 Hz during minimum bias running, it is vital to reduce the amount of background which is written to tape. In order to achieve this goal several subtriggers with additional requirements on the hadronic final state were implemented. These exclusive subtriggers had to match several conditions. Besides the reduction of background they should guarantee a measurement of *ep* events over the whole kinematic range accessible to the VLQ spectrometer. Additionally they should allow to collect a maximum number of

Exclusive Triggers			
Subtrigger	Definition	Veto	Rate [Hz]
s50	VLQ_low_OR && zVtx_T0	v:8 f:3	2 - 10
s51	VLQ_low_OR && DCRPh_Ta	v:8 f:3	1 - 4
s52	VLQ_low_OR && LAr_IF	v:8 f:3	2 - 10
s53	VLQ_low_OR && SPCLe_ToF_E_1	v:8 f:3	1 - 5

Table 5.4: *Definition and rates of VLQ related exclusive subtriggers on trigger level 1 without prescaling.*

events during the four weeks of minimum bias running. Table 5.4 shows the definition of these exclusive subtriggers and their according rates before prescaling. It is obvious that the rates of these subtriggers are much lower than the rates of the inclusive triggers in table 5.3. The reason for this is twofold: on one hand the amount of background is reduced and on the other hand events at medium and high y with a large amount of hadronic activity in the central region of the H1 detector are favoured over low y events with low or no hadronic activity at all. This leads to a large rate reduction because the high event rate at low y, due to the strong increase in the ep cross section, is more heavily reduced than the event rate at medium and high y. The combination of the VLQ trigger with the trigger element zVtx_T0 showed to be the most successful subtrigger in reducing the background while recording a large amount of statistics. This subtrigger will later be used to determine the proton structure function F_2. In H1 nomenclature this subtrigger is called s50, see table 5.4. The remaining three subtriggers s51, s52 and s53 are combinations of the low threshold VLQ trigger with a requirement on a track measured by the central drift chambers (DCRPh_Ta), on a cluster in the forward region of the LAr calorimeter (LAr_IF) or on a cluster in the SPACAL calorimeter (SPCLe_ToF_E_1). In the later measurement of the inclusive cross section, these subtriggers will not be used.

Considering the rates of the VLQ subtriggers and those of the other detector components, prescale factors have to be applied on the subtriggers with high rate at level 1 of the trigger system. To take into account the varying rates of the subtriggers during a lumi fill, these prescale factors are run dependent. It was agreed to limit the rate of the VLQ subtriggers to 5 Hz. As the emphasis was placed on subtrigger s50 the prescale factor for this subtrigger was kept at a minimum level over the course of a lumi fill. At the end of the lumi fill when the rates dropped due to the reduced beam currents, the prescale factors of the inclusive triggers s46 and s49 were reduced in order to collect a fully inclusive data sample. On level 4 of the trigger system the only requirement on events triggered by the VLQ subtriggers was a reconstructed energy deposition in one of the VLQ calorimeters larger than 6 GeV. The values for the integrated luminosity collected with subtriggers s46, s49 and s50 can be found in table 6.2.

5.2 Efficiency Determination

In this section the efficiencies of the VLQ related subtriggers will be determined. First of all the efficiencies of the inclusive triggers s46 and s49 will be discussed. Subsequently the efficiencies of the trigger element `zVtx_T0` and of the vertex reconstruction will be calculated.

5.2.1 Method

The crucial point in the determination of the efficiency of a subtrigger S is the definition of a monitor sample. A suitable monitor sample is composed of a large amount of events which have been triggered by one or several triggers independent from subtrigger S to avoid correlations which would spoil the efficiency determination. The efficiency of the subtrigger is then defined as follows:

$$\epsilon_S = \frac{\#\text{ of events triggered by S in monitor sample}}{\text{total }\#\text{ of events in monitor sample}}$$

The trigger efficiency may depend on a suitable kinematic variable. In the case of the VLQ inclusive subtriggers s46 and s49 one would expect the efficiency to depend on the energy of the scattered electron due to the energy-dependent thresholds in the trigger logic, described in section 5.1.1. Additionally production tolerances of the scintillator bars, the wavelength shifters and the photodiodes would yield a dependence of the efficiency on the impact position of the scattered electron. The efficiency of the trigger element `zVtx_T0` and of the vertex reconstruction will instead be calculated in dependence of the kinematic variable y_{had} which is a good measure for the hadronic activity in the H1 detector.

The procedure is applied to the data set as well as to the Monte Carlo event sample. In the data several additional cuts on independent variables such as timing or run quality are applied in order to reduce background. In the determination of the vertex efficiency, the contribution from satellite bunches and from pilot bunches are taken into account, (see section 5.2.3).

5.2.2 VLQ Trigger Efficiency

The efficiency determination is based on the data sample described in section 6.1. The events which compose the monitor sample are triggered by subtriggers which are independent from the VLQ related trigger elements, e.g. jet triggers, inclusive SPACAL triggers. The efficiency is then determined in dependence of the electron energy and of the x- and y-coordinate of the impact position on the calorimeter surface.

Figure 5.3 shows the efficiencies of the inclusive subtriggers s46 (full triangles) and s49 (full circles) as a function of the energy of the reconstructed cluster. The error bars represent

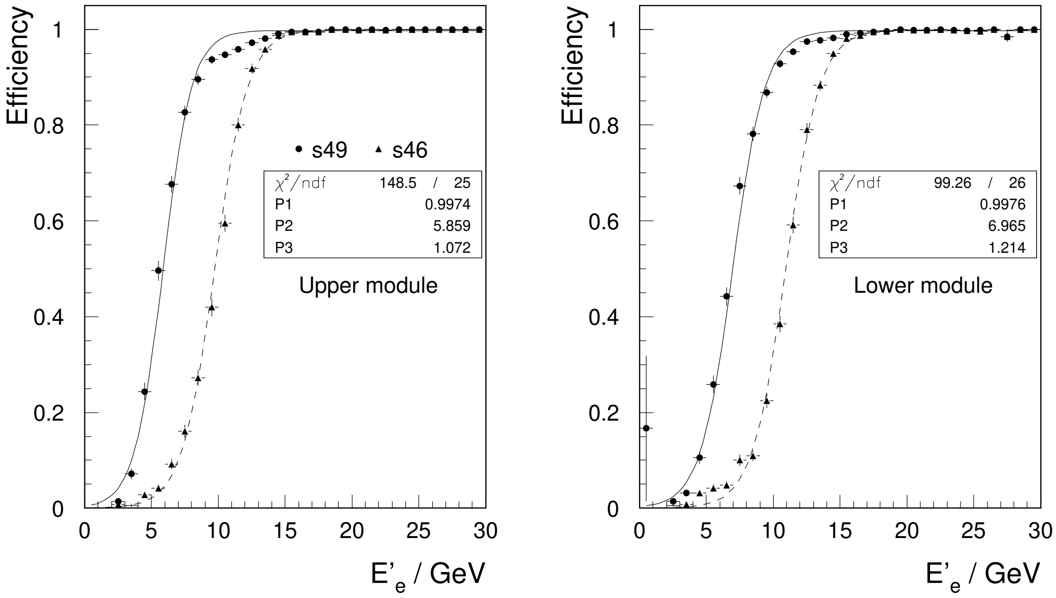

Figure 5.3: *Efficiencies of the inclusive VLQ triggers s46 (triangles) and s49 (points) as a function of the reconstructed cluster energy for the upper (left) and the lower module (right). The parameters of a fit to the efficiency of subtrigger s49 are given.*

the error of a binomial distribution:

$$\sigma = \sqrt{\frac{p(1-p)}{N}}$$

with p the efficiency and N the number of events in the monitor sample. The lower energy threshold of the `VLQ_low_OR` element of s49 can clearly be seen. A fit of an inverse Fermi function to the efficiency has been done (solid line for s49 and dashed line for s46). The fit function depending on the energy E is given by:

$$f(E) = \frac{\mathrm{P1}}{e^{\frac{\mathrm{P2}-E}{\mathrm{P3}}} + 1}$$

with the following parameter definitions:

- P1: maximum value of the efficiency
- P2: the energy value at which the efficiency reaches 50%
- P3: the width of the threshold; at a value of P2 $\pm$ 3 $\cdot$ P3 the efficiency reaches 95% resp. 5%.

The parameters of the fit to the efficiency of s49 are given in the diagram. The energy threshold of the inclusive subtrigger s49 is determined to 5.9 GeV for the upper and 7.0 GeV

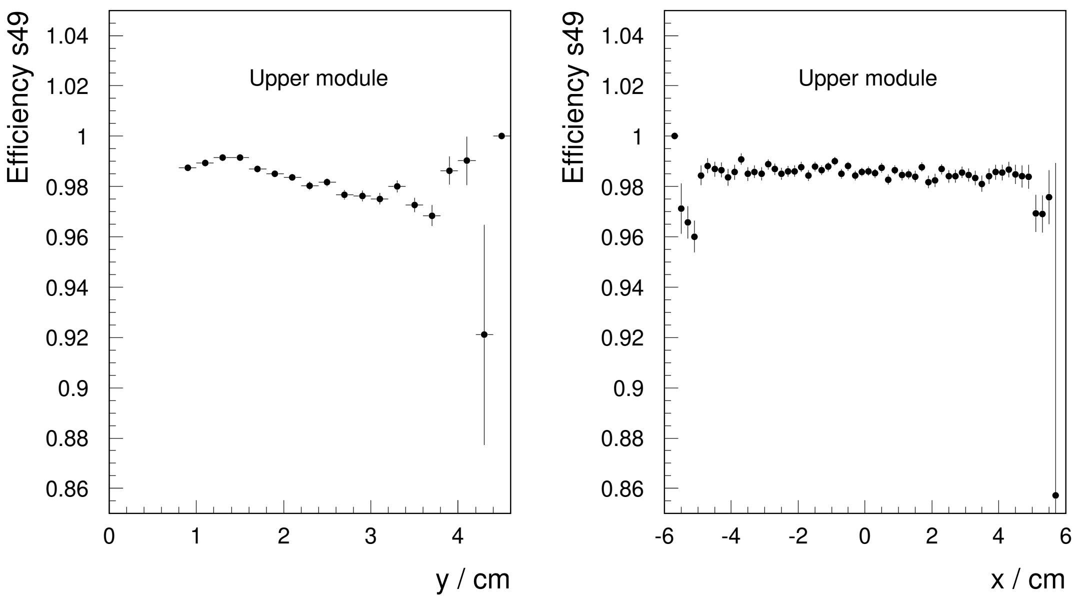

Figure 5.4: *Efficiency of the inclusive VLQ trigger s49 as a function of the reconstructed y-coordinate (left) and x-coordinate (right) of the cluster for the upper module.*

for the lower module. The efficiency for both modules exceeds 97% for energy depositions above 12 GeV. Full efficiency of the subtrigger is reached at 19 GeV. The values of the threshold for subtrigger s46 are determined to 9.7 GeV and 10.9 GeV.

A contamination of the monitor sample by events resulting from photoproduction background may influence the determination of the efficiencies of the inclusive VLQ triggers discussed in this section. As mentioned in section 4.1, a track requirement reduces the amount of background from neutral particles. Therefore a cross-check of the efficiency determination was performed by selecting events with a reconstructed track in the VLQ tracker satisfying the requirements on track-cluster distance and z_{vtx} measurement described in section 4.1. Based on this monitor sample, the efficiency of the inclusive subtriggers is determined and found to agree with the above results within the statistical accuracy.

In figure 5.4 the dependence of the s49 efficiency on the reconstructed position of the calorimeter cluster for the upper module is shown. The left diagram presents the dependence on the y-coordinate, which is defined as the distance to the calorimeter edge in y-direction. All events with an reconstructed energy above 8 GeV are included. The efficiencies show a stable behaviour at around 99%. The shielding of the upper module by the insert of the SPACAL starts at 4.0 cm. The dependence on the x-coordinate is shown in the right diagram. Again the efficiency is stable around 99%. Only at the edges of the calorimeter the efficiency is slightly reduced. The corresponding efficiencies for the lower module show a similar behaviour.

Figure 5.5 shows the stability of the trigger efficiency over time for the upper module

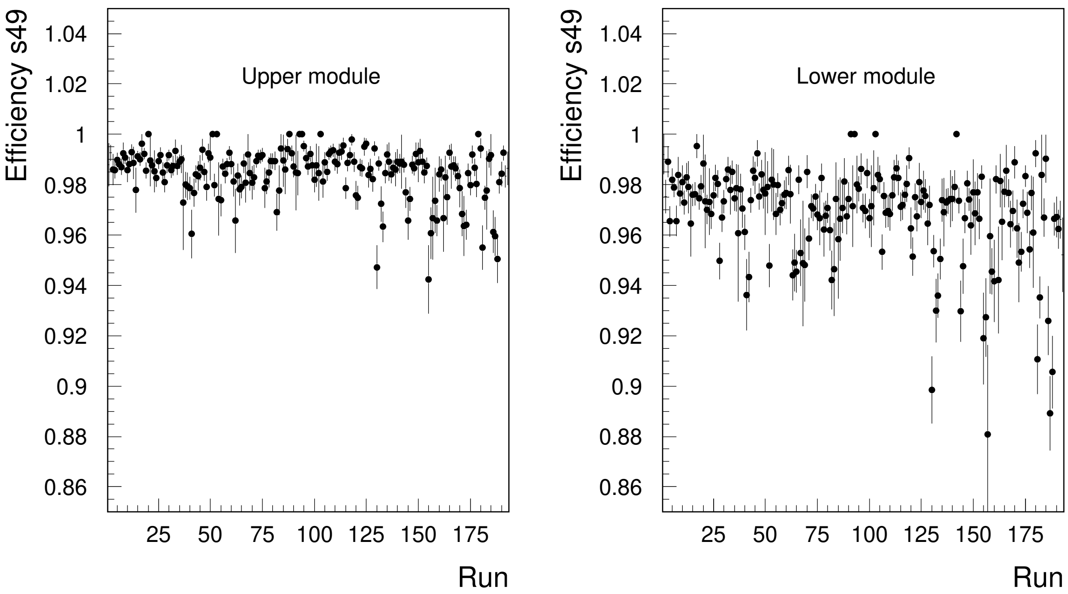

Figure 5.5: *Run dependence of the efficiency of the inclusive VLQ trigger s49 for the upper module (left) and the lower module (right).*

(left) and the lower module (right). All runs which have passed the quality criteria explained in section 6.1 are included. The efficiencies for both modules show a stable behaviour over the course of the minimum bias run, which lasted for 4 weeks. The overall efficiency of the lower module is slightly reduced, as can already be seen in figure 5.3. The runs with a decreased efficiency ($< 93\%$) at the end of the data taking for the lower module are short runs with a low number of events. The decrease in efficiency can therefore be neglected.

The results described in this section are later used to define the fiducial area of the calorimeters (section 6.2) and in the choice of the Q^2 and y bins for the cross section measurement (section 7.2). In the determination of the proton structure function F_2, the data are corrected for the reduced efficiency at low electron energies.

5.2.3 Vertex Efficiency in the Inclusive Data Sample

The triggering of NC events in the very low Q^2 region is based on the detection of a scattered electron under small scattering angles in the VLQ spectrometer with the subtriggers s46 and s49. The efficiencies of these subtriggers have been determined in the previous section 5.2.2. In the offline analysis of the inclusive data sample a requirement is placed on the information of the central tracking of the H1 detector. Only events with a vertex determined by the central tracker are selected for further analysis. As this vertex requirement is independent on the VLQ subtriggers s46 and s49 the efficiency of the vertex requirement can be calculated separately.

In an investigation on the efficiency of a vertex requirement, the inclusive VLQ triggers s46 and s49 are suitable independent triggers, on which the monitor sample is based. Additionally it is required that only one cluster is reconstructed in the VLQ spectrometer inside the fiducial area (section 6.2). To reduce the background contribution from photoproduction and other sources, the following cuts $E - P_z > 35$GeV and $E_{had} > 5$ GeV are required.

Two effects influencing the efficiency are also included in the determination procedure:

- Satellite bunches
  A bunch of the HERA proton beam has a complicated longitudinal structure. It consists of one large proton bunch and several smaller neighbouring ones, the satellite bunches. They lead to additional peaks in the z_{vtx}-distribution, the largest being at a z position of +70 cm, see figure 6.3. The contribution from satellite bunches has been estimated to 4% [2] [56]. Events resulting from these satellite bunches can not be removed from the monitor sample and are therefore statistically subtracted. A large sample of `PHOJET` events has been simulated with the interaction vertex at $z = +70$ cm. This event sample is then normalized to a relative contribution of 4% and added to the inclusive MC event sample. Thereafter the above described procedure is carried out to determine the vertex efficiency. The inclusion of the satellite bunches leads to a decrease of $\approx 0.5\%$ of the vertex efficiencies in the simulation.

- Pilot bunches
  Approximatively 175 bunches of each beam particle type are brought to collision in the center of the H1 detector. Additionally several bunches of each particle type[3] are stored in HERA which have no colliding counterpart, called pilot bunches. The particles of these pilot bunches can interact with residual beam gas or beam line elements only. The random background, e.g. caused by cosmic or beam halo muons, may be determined by empty bunch events. In section 6.5 it will be shown that events resulting from electron beam induced non *ep* background amount to $\approx 25\%$ of the data sample before the cuts on the hadronic final state and thus may also influence the vertex efficiency determination. During the procedure described in this section, both pilot bunch and empty bunch events are normalized to the number of colliding bunches and afterwards statistically subtracted from the data monitor sample. The contribution from pilot bunches is efficiently reduced by the cut $E_{had} > 5$ GeV and thus the influence on the vertex efficiency is negligible.

In figure 5.6 the dependence of the efficiency of the vertex requirement on y_{had} on a linear scale and on a logarithmic scale is presented for the inclusive data sample. y_{had} reconstructed with the Hadron Method (see section 2.3.2) measures the amount of hadronic

[2] The luminosity value for each run provided by the H1 Lumi system is corrected for the contribution caused by satellite bunches.

[3] Usually 14 electron pilot bunches and 6 proton pilot bunches are stored in HERA.

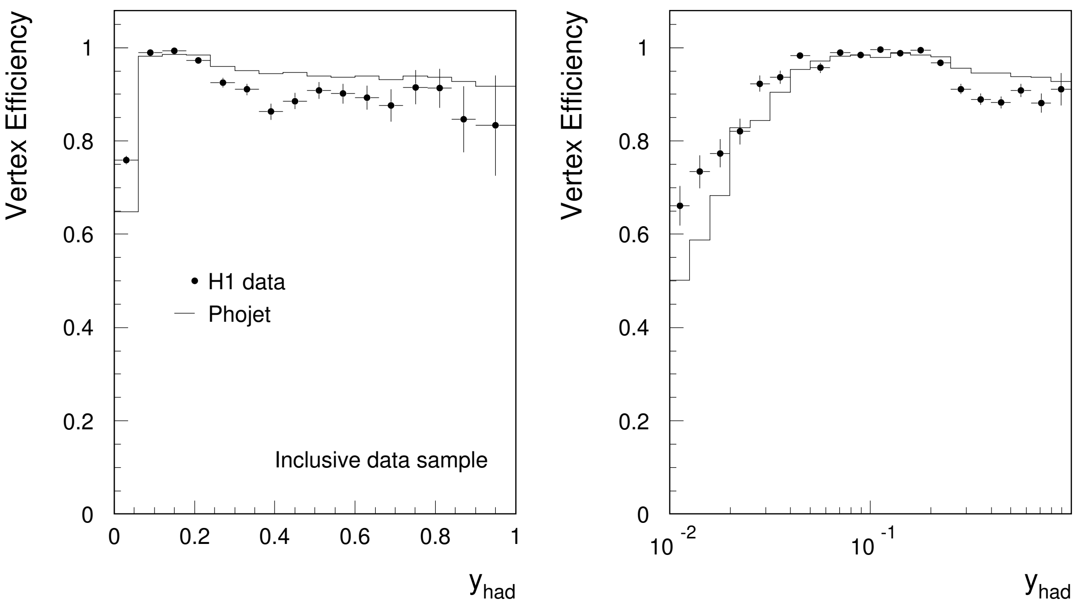

Figure 5.6: *Efficiency of the vertex requirement in dependence of y_{had} on a linear (left) and a logarithmic scale (right) for the inclusive data sample. The H1 data are represented by the points whereas the efficiency of the simulation is given by the histogram.*

activity in the H1 detector and is therefore a suitable variable to study the behaviour of the vertex reconstruction efficiency. The points represent the efficiency of the data sample whereas the histogram shows the efficiency of the simulation. As event generator PHOJET was used, see section 3.1.1.

Both data and simulation show high efficiency in the region of $y > 0.1$ whereas in the kinematic peak region $y < 0.1$ the efficiency of the vertex reconstruction is strongly decreasing. The efficiency in the data is well described by the simulation. The discrepancies are taken into account by a reweighting of the simulated events.

5.2.4 Vertex Efficiency in the Exclusive Data Sample

The subtrigger s50, defined in section 5.1.2, combines the inclusive subtrigger s49 with the trigger element `zVtx_T0`. The multiwire proportional chambers CIP, COP and FPC (see section 2.2.1) deliver an online reconstruction of the z-coordinate of the interaction vertex [57]. The pad signals from these chambers are connected by a straight line and extrapolated to $z = 0$. If the intersection of one of these lines with the beam axis lies in the range of $[-43.9\text{ cm}; 43.9\text{ cm}]$ around the nominal interaction point, the `zVtx_T0` triggerelement is set.

As in the case of the inclusive data sample, an offline requirement of an interaction vertex reconstructed by the central tracking of the H1 detector is made. To avoid correla-

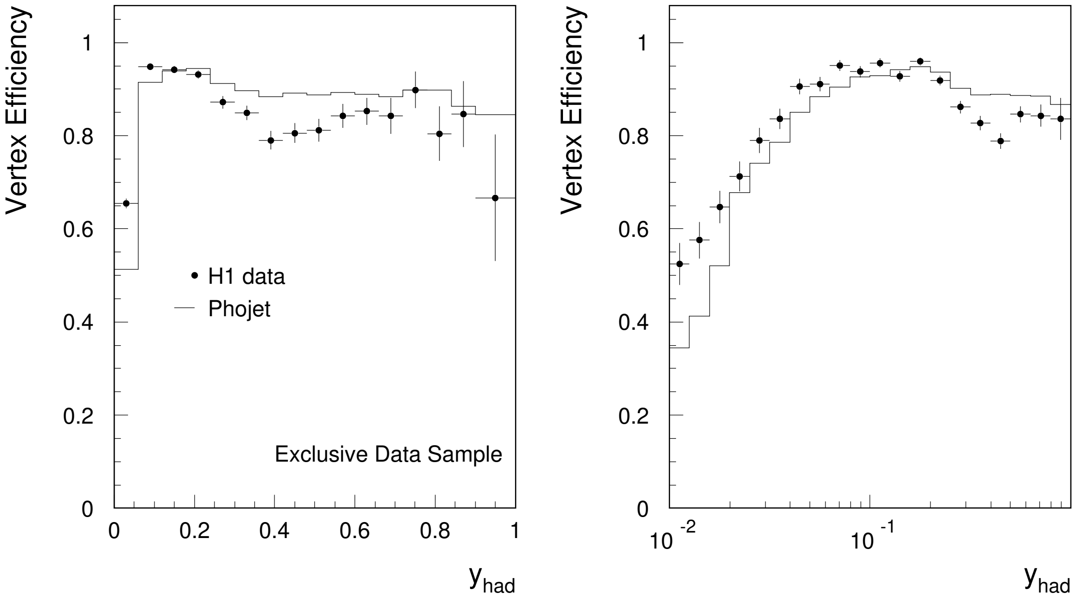

Figure 5.7: *Efficiency of the vertex reconstruction as a function of y_{had} on a linear (left) and a logarithmic scale (right) for the exclusive data sample. The H1 data are represented by the points whereas the efficiency of the simulation is given by the histogram.*

tions between the trigger element `zVtx_T0` and the offline vertex requirement `izvtx=1` the efficiency of a combination of these conditions is determined.

The monitor sample in the determination of the vertex reconstruction efficiency is defined by the same cuts as described in the previous section. Corrections for satellite and pilot bunches are also included.

Figure 5.7 shows the dependence of the efficiency of the vertex reconstruction in the exclusive data sample on the kinematic variable y_{had} on a linear scale and on a logarithmic scale. The overall behaviour with y_{had} in the data is similar to the inclusive case and is rather well described by the simulation. The discrepancies are taken into account by a reweighting of the simulated events.

6
Data Selection

The analysis of the proton structure function F_2 in the very low Q^2 region is based on the measurement of the scattered electron in the VLQ spectrometer. In order to guarantee a precise determination of the kinematic variables and to suppress background contributions, a set of selection cuts are applied to the data and the Monte Carlo sample.

First of all the data set on which the analysis is based and the subsequent run selection is presented in this section. Then the cuts on the fiducial area of the VLQ calorimeters and the electron identification are outlined. Investigations on the rejection of background events follow. Finally the trigger selection are discussed.

6.1 Run Selection

In the standard data taking triggers with high rates (e.g. VLQ inclusive triggers) are heavily prescaled to reduce the amount of data to be stored and to reduce the dead time of the H1 detector. However during certain designated periods of time, a trigger setup is chosen where low Q^2 inclusive triggers are not at all or only slightly prescaled, a so-called minimum bias run. These data sets are then mainly used to measure inclusive cross-sections in the region of low Q^2.

The data set used in this analysis was recorded during a minimum bias run from November 15 1999 to December 13 1999. The trigger setup on level 1 consisted partially of VLQ-related subtriggers, see section 5.1.2. The run-dependent prescales were chosen such that the total event rate triggered by the VLQ spectrometer was kept at approximatively 5 Hz over the course of a luminosity run. The only requirement on level 4 of the trigger system consisted of a reconstructed energy deposition above 6 GeV in one of the VLQ calorimeters.

An offline selection of the recorded runs was made according to the following criteria:

- Both modules of the VLQ spectrometer were in data taking position.
- The run was recorded in phase 2 of data taking[1].

[1]The data taking of the H1 experiment is divided into three phases. In phase 1 e and p beams are steered to maximize the specific luminosity and to reduce the rate of background processes (lumi tuning). In phase

- The run was qualified as “good”. All major systems were operational: the central jet chambers, the main calorimeters, the tracking chambers, the luminosity system and the muon chambers. Due to a water leak the forward tracking chambers were not operational during the end of 1999.
- The luminosity recorded in the run exceeded 0.5 nb^{-1}.
- Runs were excluded which showed an increased number of events per luminosity for the upper module. 13 runs showed this effect which was most likely due to a deteriorated background situation.

A total of 184 runs fulfill these conditions corresponding to an integrated luminosity of 2.3 pb^{-1} recorded by the H1 detector. The luminosity recorded by the subtriggers used in this analysis differs from the above value due to the prescaling on level 1 of the trigger system (see table 6.2).

6.2 VLQ Fiducial Cuts

In order to increase the precision of the energy and polar angle measurement of the scattered electron leakage effects at the edges of the calorimeters and areas which are shaded by other detector components have to be taken into account. Leakage effects occur when the electron hits the calorimeter near the edge and part of the electromagnetic shower is lost. The consequences for the cluster reconstruction caused by this energy loss are twofold. The reconstructed energy of the cluster is smaller than the ’true’ value. This can be partially compensated by a spatial dependence of the calibration, see section 4.2.1. Moreover the reconstructed impact position lies further away from the edge than the ’true’ position, due to the energy loss on one side of the cluster. This behaviour can be seen in figure 6.1. On the left (right) hand side the difference $\Delta y = y - y_T$ of the reconstructed y-position from calorimeter y and tracker y_T w.r.t. the absolute value of y for the upper (lower) module is shown for the data[2]. As the track reconstruction is not affected by leakage effects, the coordinate y_T from the tracker gives the ’true’ position. For both modules the calorimeter measurement deviates from the track value at low values of |y|, which indicates that the energy loss due to leakage is still large. At $\approx$ 1 cm from the edge the calorimeter and the tracker measurement lie within the shaded band indicating the region of $\pm$ 0.025 cm, which corresponds to the resolution of the calorimeter. At a |y| value of 6.5 cm resp. 7.5 cm the deviations become again large because of the shielding by the SPACAL insert. By the same procedure the fiducial cuts in x-direction have been chosen to $|x| < 4$ cm. In figure 6.2

2 a stable operation of HERA is achieved and the H1 experiment is in standard data taking mode. The rest of the time e.g. the beams are lost, ramping of beams etc. the H1 experiment is in phase 0.

[2]In order to avoid an influence of the shielding of the SPACAL insert, only events inside a vertical band of $|x| < 0.5$ cm enter this plot.

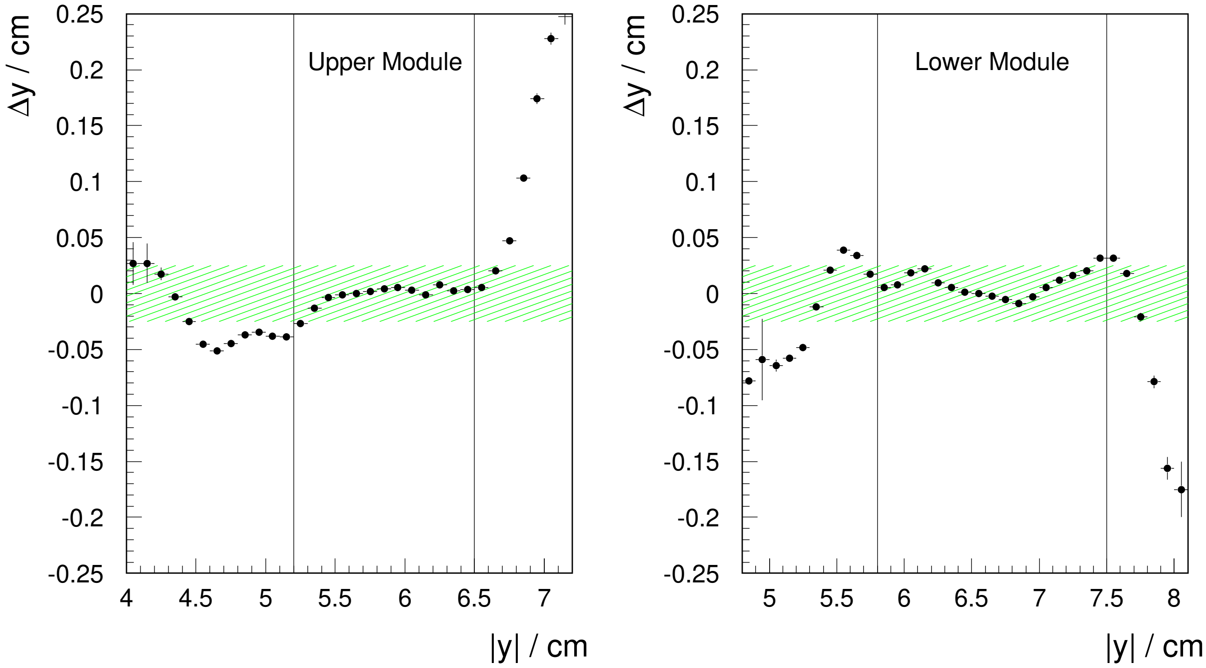

Figure 6.1: *Difference Δy $=$ y $-$ y_T of the reconstructed y-position from calorimeter y and tracker y_T w.r.t. |y| for the upper (left) and the lower (right) module for data. The shaded band indicates the region of $\pm$ 0.025 cm. The vertical lines represent the fiducial cuts in y-direction.*

the impact position of the scattered electron reconstructed with the calorimeter is shown. The circular shape of the SPACAL insert can clearly be seen by the dramatic drop of the population density at large values of |y|. The cuts on the fiducial area of the VLQ have been chosen such that both requirements (small leakage effects and no shielding by the insert) are satisfied. The values of the fiducial area are listed in table 6.2. The lines in figure 6.1 and 6.2 indicate the cut values. One sees that energy depositions also occur at positions shielded by the SPACAL insert. These events are due to backscattering of particles off beam line elements.

	Upper module	Lower module
y	y > 5.2 cm	y < -5.8 cm
$r = \sqrt{x^2 + y^2}$	r < 6.5 cm	r < 7.5 cm
x	|x| < 4 cm	

Table 6.1: *Definition of the fiducial area for the VLQ calorimeters.*

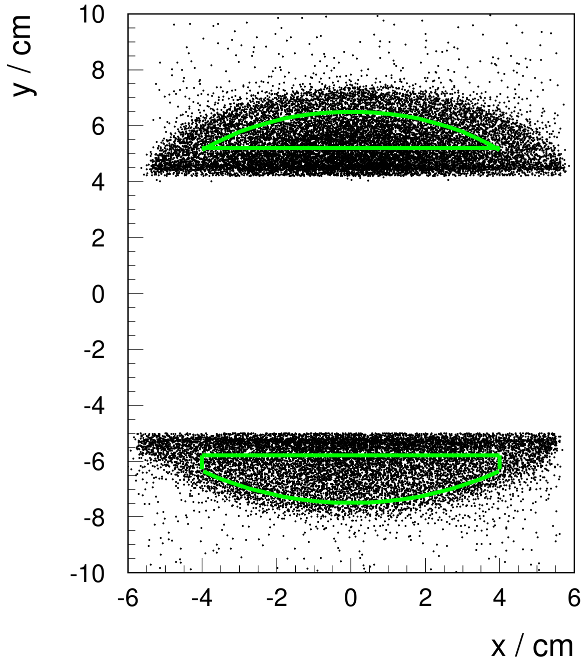

Figure 6.2: *Impact position of the scattered electron reconstructed with the calorimeter. The lines indicate the fiducial area of the VLQ defined for this analysis. The circular shielding of the SPACAL insert is visible.*

6.3 Electron Identification and Reconstruction

The reconstruction of the event kinematics is based on the correct identification of the scattered electron. The electron identification procedure used in this analysis requires an energy deposition in one of the VLQ calorimeters inside the fiducial area of the VLQ spectrometer. The event sample is dominated by events with a single cluster. 97% of the events in the upper module and 94% of the events in the lower module are single cluster events. In the case that two clusters are reconstructed in one VLQ calorimeter, e.g. resulting from final state radiation, the clusters are merged if the distance between them is smaller than 2.5 cm otherwise the cluster with the higher energy is identified as scattered electron. The contribution from events with more than two clusters in one calorimeter module is negligible ($< 0.5\%$). Events which have an energy deposition in each calorimeter module, e.g. QED-Compton events, are efficiently suppressed by the vertex requirement, see section 6.5.2. The contribution is below 0.1%.

Based on the results of the calibration (see section 4.2.1) and the alignment (see section 4.2.2) of the VLQ calorimeters the energy and the position of the electromagnetic cluster are reconstructed. In order to calculate the polar angle θ of the scattered electron, it is necessary to determine the z-position of the interaction vertex. As the VLQ tracker suffers from a low efficiency, the interaction vertex can not be reconstructed by an electron track and has thus to be reconstructed using hadronic tracks in the central track detector. 50% of the event

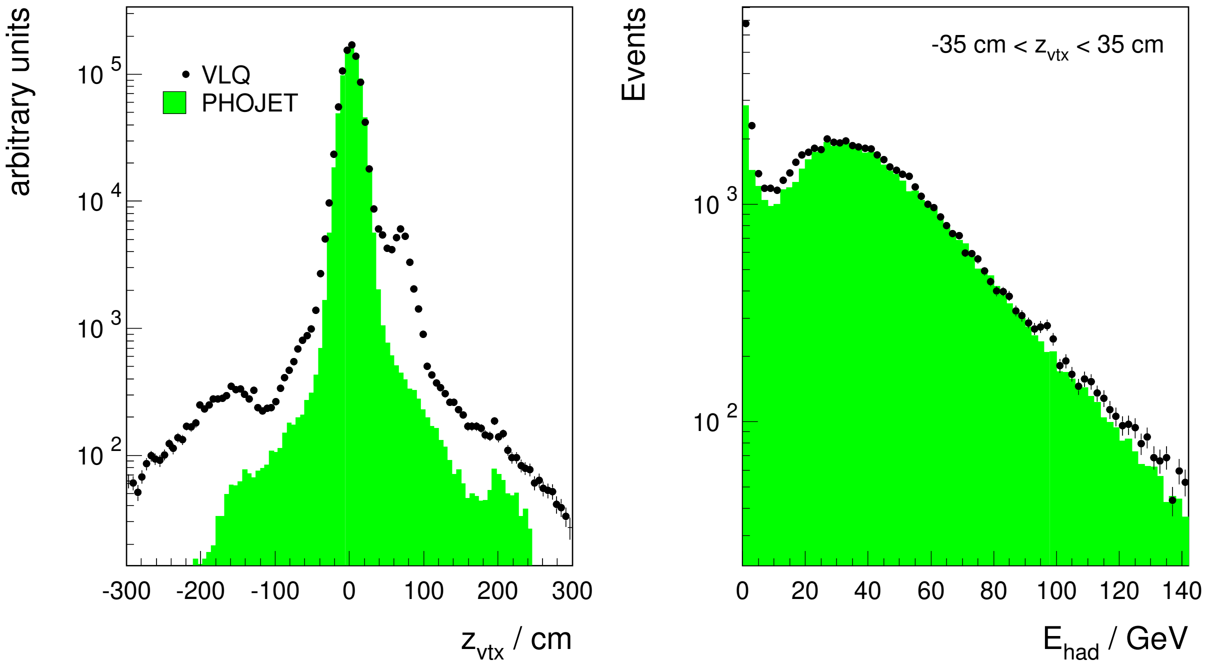

Figure 6.3: *Distribution of the reconstructed z-position of the vertex (left) and the energy of the hadronic final state (right) in data and Monte Carlo.*

sample with an energy deposition in one of the VLQ calorimeters show at least one track in the CTD enabling the measurement of the interaction vertex. For the remaining part of the event sample, the interaction vertex can not be determined and no accurate reconstruction of the polar angle can be provided. Therefore events without a reconstructed central vertex are rejected. The impact of this requirements will be discussed in the following sections.

6.4 Technical Cuts

The left diagram of figure 6.3 shows the distribution of the reconstructed z-position of the vertex using central tracks for data in comparison with the distribution of the simulated events. The structure in the data distribution at large values of z is due to the complex longitudinal structure of the particle bunches. The peak at $z = +70$ cm is caused by proton satellites, see section 5.2.3. As this beam structure is not modeled in the simulation, it is necessary to restrict the interaction vertex to the central region [-35 cm;35 cm].

Additionally it is necessary to reject events with low hadronic energy E_{had} in the final state. Figure 6.3 shows the E_{had} distributions for data and the PHOJET MC normalized to the luminosity of the data set. The data distribution is very well described by the Monte Carlo for large values of E_{had} whereas at $E_{had} < 5$ GeV the data show a large excess. In figure 6.4 the region of low energy of the hadronic final state for data in comparison to PHOJET is

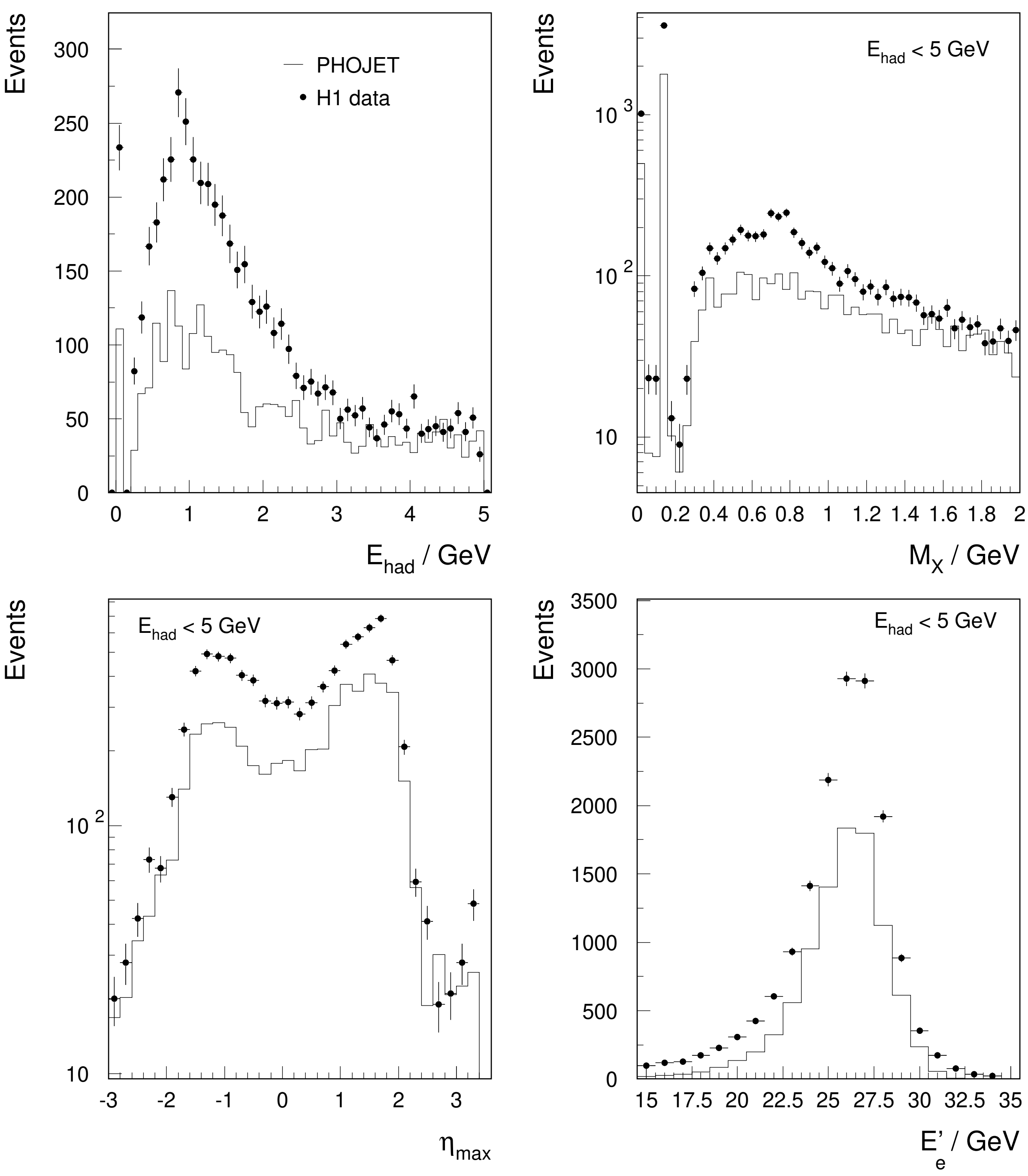

Figure 6.4: *Distributions of the energy E_{had} (upper left), the invariant mass M_X (upper right), the maximum rapidity η_{max} (lower left) of the hadronic final state and the energy of the scattered electron E'_e (lower right). All distributions are shown for events with $E_{had} < 5$ GeV.*

given. The data distribution shows an excess at $E_{had} \approx 1$ GeV. As the distribution of the invariant mass of the hadronic final state indicates, the excess is mainly caused by events with a single pion ($M_\pi = 0.139$ GeV) in the final state. As can be seen in the η_{max} distribution, these events with single pions show a large rapidity gap and are therefore presumably of diffractive nature. Finally the events with low hadronic energy tend to lie at high electron energies E'_e. As the absolute normalization of this diffractive contribution to the total cross section is not modeled by the PHOJET Monte Carlo, it is necessary to reject events with $E_{had} < 5$ GeV to guarantee a correct calculation of the correction factors, see section 7.1. This cut provides a much improved description of the η_{max} distribution. see section 7.3.

6.5 Background Rejection

The background to the measurement of the inclusive cross section is divided into non-*ep*-induced and *ep*-induced background. Both contributions will be discussed in the following sections.

6.5.1 Non-ep-induced Background

Beam-gas and beam-wall events represent the largest contribution to non-*ep*-induced background. Beam-gas background is caused by scattering of beam particles off residual gas atoms in the beam pipe. Beam-wall background is induced by beam particles, e.g. off-momentum particles deflected by the electromagnetic field of the focusing magnets, hitting beam line elements. The event rate from non-*ep*-induced background is much larger than the *ep* event rate (50 kHz compared to ≈20 Hz), but the amount of background events is already efficiently reduced by the time-of-flight information of the level 1 trigger system.

The contribution of non-*ep*-induced background may be estimated with pilot bunches, see section 5.2.3. The amount of empty and pilot bunches is normalized to the number of colliding bunches. The left plot in figure 6.5 shows the relative contribution of the different event topologies to the event sample. The empty histogram depicts the relative contribution before the vertex requirement. Empty bunch events are negligible while electron- and proton-beam induced background events correspond to ≈ 25% of the data sample. The vertex from non-*ep*-induced background is randomly distributed in z-direction while the z_{vtx}-distribution of *ep* events shows a gaussian distribution around the nominal interaction point. Additionally non-*ep*-induced background events show predominately a low energy hadronic final state. One expects a significant reduction of non-*ep*-induced background by the requirements on the hadronic final state: a primary vertex with z-position in the range of [-35 cm;35 cm] and hadronic energy $E_{had} > 5$ GeV. The shaded histogram represents the relative contribution of the different event topologies after these requirements. The contribution of non-*ep*-colliding bunches is reduced to less than 0.5%. The right hand side of figure 6.5 shows the VLQ energy distribution for electron beam induced non *ep* background events before the hadronic cuts (empty histogram). The contribution from electron beam induced background increases towards lower energies. As expected the hadronic requirements heavily suppress this contribution (shaded histogram).

A further reduction of the non-*ep*-induced background can be achieved by using the timing information delivered by the CJC. Events which do not lie within $\pm$ 20 ns of the bunch crossing are rejected. The inefficiency of this cut has been estimated to be less than 1 %.

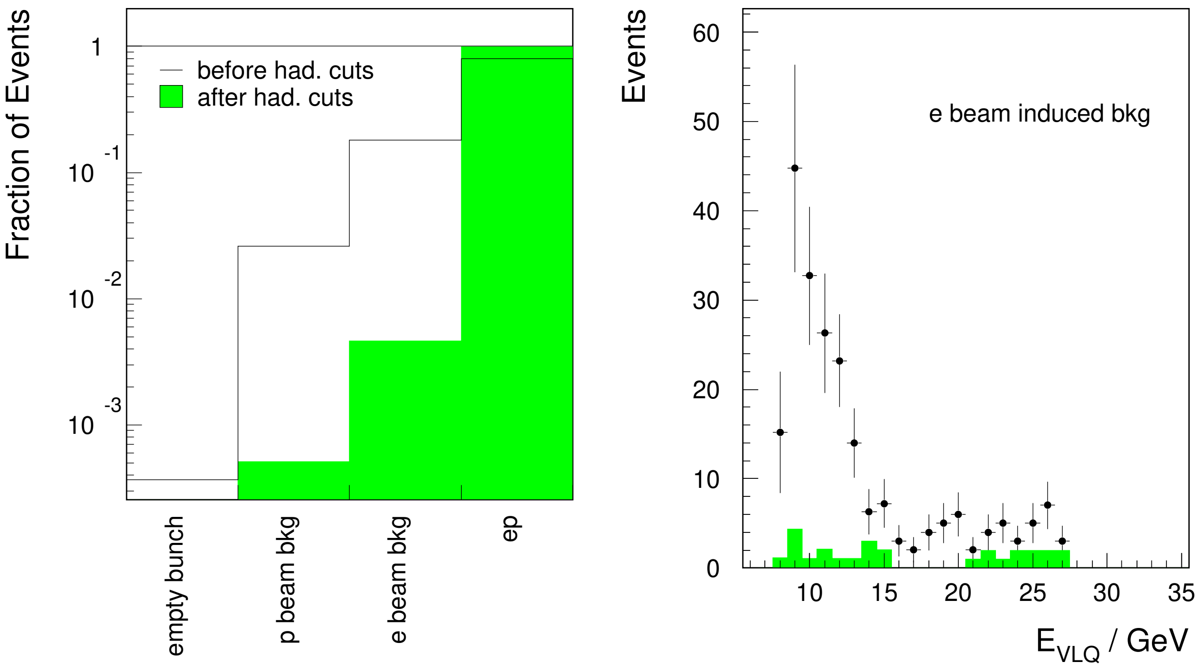

Figure 6.5: *Relative contribution of empty , proton beam induced background, electron beam induced background and ep-colliding bunches to the total event sample before (empty histogram) and after the cuts on the hadronic final state (shaded histogram). VLQ energy distribution for electron beam induced background before (points) and after the cuts on the hadronic final state (shaded histogram).*

6.5.2 ep-induced Background

Two sources of *ep*-induced background may contribute in the phase space of the VLQ spectrometer: photoproduction and QED-Compton events.

Photoproduction background arises from events with a particle of the hadronic final state hitting a VLQ calorimeter. The energy deposition is misidentified as scattered electron while the 'true' scattered electron is not detected in the VLQ and escapes undetected through the beampipe. The contribution of photoproduction to the total data sample is estimated with so-called tagged events. In these events the scattered electron is detected in the electron tagger (ET) of the luminosity system. The left diagram in figure 6.6 shows the total $(E-P_z)_{\mathrm{all}}$

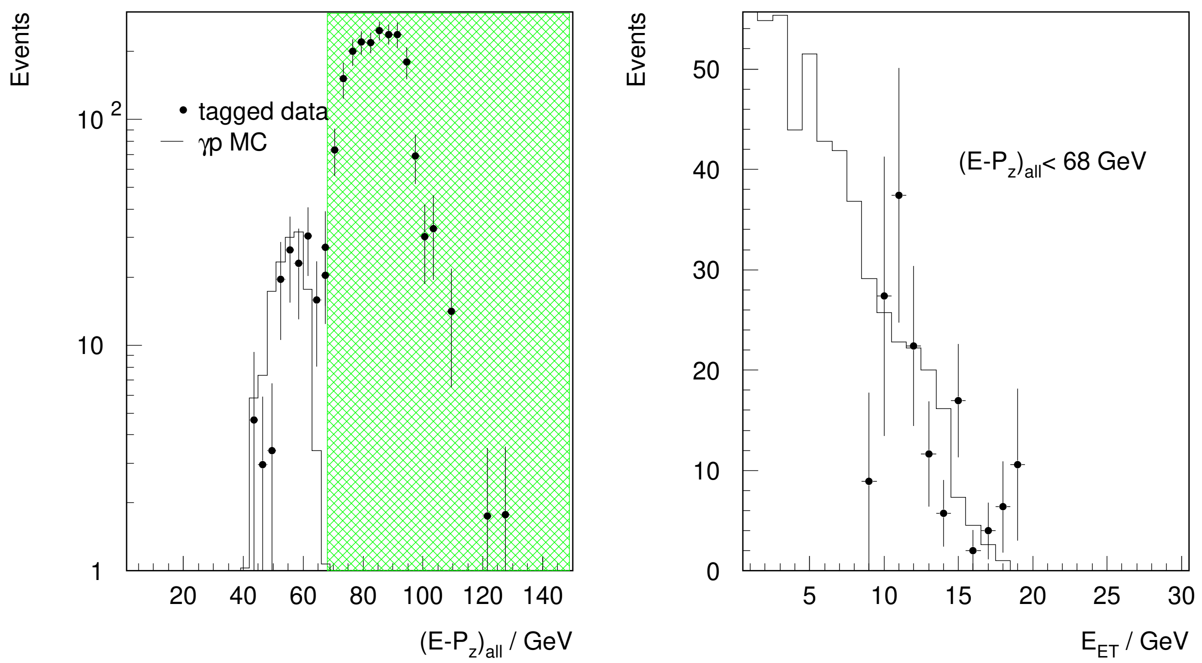

Figure 6.6: *On the left the $(E-P_z)_{\rm all}$ distribution for tagged events for data (points) compared to a photoproduction MC (histogram) is shown. The shaded area indicates the region of overlapping events. Energy spectrum in the electron tagger ET for tagged events with $(E-P_z)_{\rm all} < 68$.*

distribution for the tagged events including the energy deposits E_{ET} in the electron tagger:

$$(E-P_z)_{\rm all} = E-P_z + 2 \cdot E_{ET} \qquad \text{with} \qquad E-P_z = \sum_{i=1}^{N}(E_i - P_{z,i})$$

where i runs over all particles of the final state detected in the central H1 detector. If the measured $(E-P_z)_{\rm all}$ value is roughly 55 GeV, all particles of the final state including the electron in the ET come from one ep scattering (photoproduction). Instead if $(E-P_z)_{\rm all}$ shows much higher values, the particles of the final state may arise from two overlapping ep scattering processes, e.g. a DIS and a Bethe-Heitler event. The solid line corresponds to a photoproduction Monte Carlo, which is corrected for the restricted acceptance of the ET in the range of $0.3 < y < 0.7$. It gives a good description of the data in the range of $(E-P_z)_{\rm all} < 68$ GeV. A large contribution from overlap events in the region of $(E-P_z)_{\rm all} > 68$ GeV is visible. In the right diagram of figure 6.6 the energy distribution of the scattered electron in the ET is shown for tagged events with $(E-P_z)_{\rm all} < 68$ GeV, thus resulting from photoproduction. The restricted acceptance of the ET at low values of E_{ET} is clearly seen in the data. The extension to lower energy values over the acceptance range of the ET is shown for the γp MC. The good description of the tagged data by the photoproduction Monte Carlo is necessary to guarantee a correct subtraction of the background contribution from the measured cross section in the determination of the proton structure function F_2.

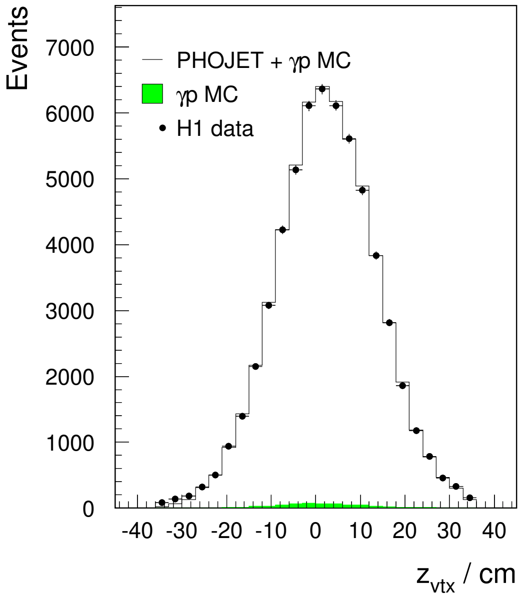

Figure 6.7: *z_{vtx} distribution in data (points) and Monte Carlo (histogram) after all selection cuts and efficiency corrections are applied.*

Wide-Angle Bremsstrahlung events (so-called QED-Compton events) are an additional source of *ep*-induced background. The Feynman diagrams of the QED-Compton process are shown in figure 4.17. In the case of elastic QED-Compton events the final state detected in the H1 detector is solely composed of the scattered electron and a photon while in the inelastic case the proton breaks up and yields additional particles in the final state. In both cases the number of particles of the final state in the central region of the H1 detector is small. Therefore QED-Compton events are efficiently suppressed by the requirements on the hadronic final state. The remaining contribution by QED-Compton events is below 0.1%.

Figure 6.7 shows the distribution of the z-coordinate of the interaction vertex measured with the CJC, the so-called z_{vtx}, for the data (points) and Monte Carlo (histogram) after all selection cuts and efficiency corrections are applied. The distribution is based on the event sample triggered by subtrigger s50. The simulation gives a good description of the data distribution.

6.6 The Trigger

The trigger setup and the efficiencies of the various subtriggers, including offline vertex requirements, are described in detail in section 5. The overall efficiency for the inclusive and

Subtrigger	Definition	Luminosity [nb^{-1}]	# events after selection cuts
s46	`VLQ_high_OR`	450	29000
s49	`VLQ_low_OR`	90	6200
s50	`VLQ_low_OR` && `zVtx_T0`	878	55000

Table 6.2: *Definition and integrated luminosity of VLQ related subtriggers on trigger level 1. The number of recorded events, after all selection cuts are applied, is also shown.*

the exclusive data samples are determined as follows on an event by event basis:

$$
\begin{aligned}
\epsilon(\text{s46 \&\& rec.vertex}) &= \epsilon(\texttt{VLQ\_high\_OR}) \cdot \epsilon(\text{rec.vertex}) \\
\epsilon(\text{s49 \&\& rec.vertex}) &= \epsilon(\texttt{VLQ\_low\_OR}) \cdot \epsilon(\text{rec.vertex}) \\
\epsilon(\text{s50 \&\& rec.vertex}) &= \epsilon(\texttt{VLQ\_low\_OR}) \cdot \epsilon(\texttt{zVtx\_T0}\text{ \&\& rec.vertex})
\end{aligned}
$$

The procedure of multiplying the different efficiencies is valid because the requirements on the hadronic final state (a reconstructed vertex and/or the trigger element `zVtx_T0`) and the inclusive VLQ subtriggers (s46 or s49) are independent from each other.

The integrated luminosity[3] recorded by each subtrigger is given in table 6.2. Due to the prescaling of the subtriggers on trigger level 1, the luminosity values differ from the total integrated luminosity of 2.3 pb^{-1} recorded by the H1 detector during the minimum bias run. The largest data set has been recorded with the subtrigger s50.

Considering the rejection of background events and the recorded luminosity, the subtrigger s50 was chosen as main subtrigger in this analysis. Additionally data samples triggered by subtriggers s46 and s49 are used to perform cross checks.

6.7 The Final Selection Criteria

Finally the following selection cuts have been applied to the recorded data set and the MC sample in the determination of the proton structure function F_2:

- run selection
- event triggered by s50
- one electron candidate inside the fiducial area of the VLQ calorimeters
- primary central interaction vertex with $-35\text{cm} < z_{vtx} < 35$ cm.

[3] The correction of the luminosity measurement necessary because of satellite bunches is included in the given values (see also section 5.2.3).

- energy of the hadronic final state: $E_{had} > 5$ GeV
- CJC timing

Table 6.2 lists the number of events after all selection cuts for the main subtrigger s50 and for the inclusive subtriggers s46 and s49. Considering the fact that the efficiencies determined in section 5 are not yet applied, the number of events scale approximatively with the recorded luminosity for each subtrigger. Figure 6.8 shows the number of events per luminosity run as a function of time for subtrigger s50. All selection cuts are applied to the data set. The upper (left) and the lower (right) module show a stable behaviour over the duration of the minimum bias run.

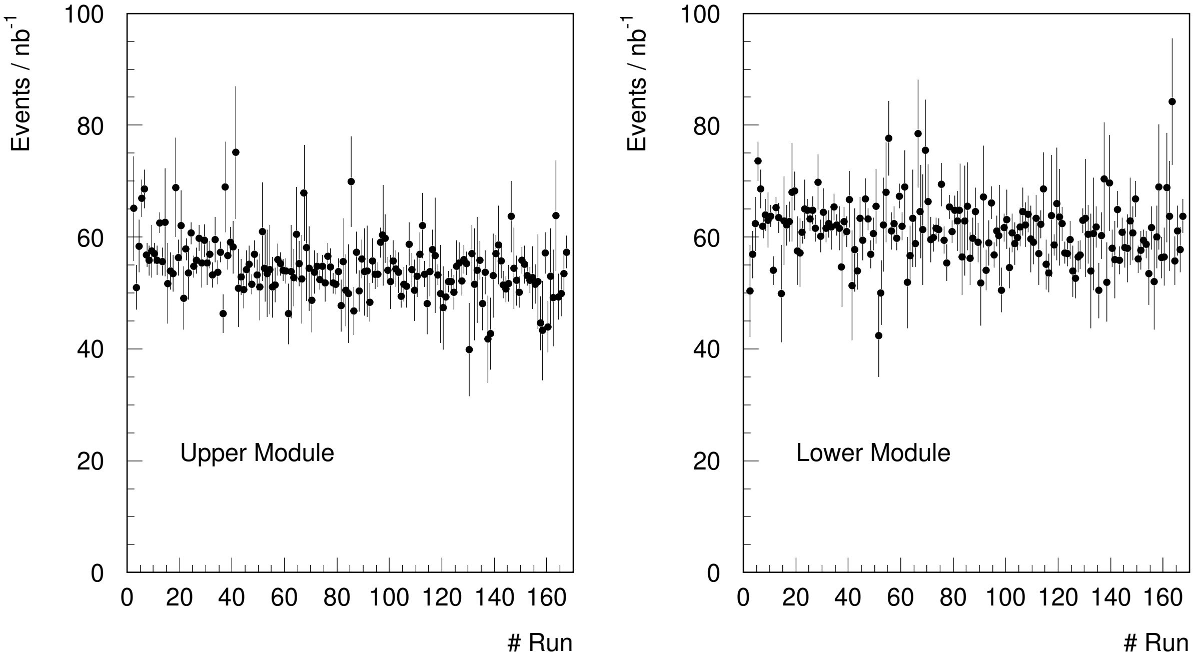

Figure 6.8: *Event yield of subtrigger s50 after all selection cuts during the minimum bias run versus run number for the upper (left) and the lower (right) module.*

7
Measurement of $F_2(x,Q^2)$

In this section the measurement of the proton structure function F_2 with the VLQ spectrometer is presented. First of all the method used in the determination of F_2 (x,Q^2) and the binning of the phase space are outlined. After all selection criteria and efficiencies are applied the simulated MC distributions are compared to the data. The radiative corrections to the cross section are determined. Finally the systematic uncertainties on the measurement are discussed and the final result on the proton structure function F_2 is presented.

7.1 The Method

Determination of the Cross Section

A cross section is given by the ratio of the number of events N to the luminosity $\mathcal{L}$:

$$\sigma = \frac{N}{\mathcal{L}}$$

Taking into account the resolution of the kinematic variables and the statistics of the data set, a cross section can be calculated differentially in one or several suitable variables. The cross section in this analysis is determined in Q^2-y bins. In contrast to a binning in Q^2-x, the binning in Q^2-y allows for the extension of the accessible kinematic range to low values of x and Q^2, see figure 7.1. Considering detector effects, radiative corrections and background contributions the main relation for the determination of the inclusive double differential cross section in a bin j of finite size (Δy, ΔQ^2) is given by:

$$\frac{d^2\sigma}{dydQ^2} = \frac{1}{\Delta y \Delta Q^2}\left[\frac{\sum_{i=1}^{N_j}\epsilon_i^{-1} - N_{bkg,j}}{A_j \cdot \mathcal{L}_{\text{int}}}\right]\frac{1}{1+\delta_{r,j}}C_{b,j} \tag{7.1}$$

with the following definitions:

- Δy and ΔQ^2 the width of bin j in y respectively Q^2.
- N_j the total number of events measured in bin j.

- ϵ_i the trigger efficiency of event i. The trigger efficiency is applied on an event by event basis for a given subtrigger according to the relation given in section 6.6. The efficiency of the inclusive VLQ triggers and the efficiency of the vertex requirement have been determined in section 5.2.

- $N_{bkg,j}$ the number of background events in bin j. The contribution from background is efficiently suppressed by the requirements on the hadronic final state. The remaining background caused by photoproduction is estimated with a γp MC, see section 6.5.

- A_j the acceptance of bin j. The acceptance correction takes into account on one hand detector effects, e.g. the limited geometrical acceptance of the detector, the finite resolution of the energy measurement and the position determination and on the other hand the efficiency of the selection criteria. In order to compare measurements from different experiments (in which acceptance and resolution may differ) it is necessary to unfold the data for detector effects and selection efficiencies. In this analysis the unfolding of the data is done by the "bin-by-bin" unfolding method. The acceptance A_j for a given bin j is determined with the MC simulation and is defined as the ratio of the number of events $N_{rec,j}$ reconstructed in bin j after all selection cuts to the number of events $N_{gen,j}$ generated in bin j: $A_j = N_{rec,j}/N_{gen,j}$. This unfolding method is only valid if the correlations between single data points are small. This assumption will be justified in the next section 7.2.

- $\mathcal{L}_{\text{int}}$ the integrated luminosity of the data set for the chosen subtrigger.

- $\delta_{r,j}$ the correction due to radiative processes for bin j. $\delta_{r,j}$ is defined as the ratio of the cross section σ_{rad} including QED corrections to the cross section σ_{Born} on Born level: $1 + \delta_{r,j} = \sigma_{rad}/\sigma_{Born}$. The radiative corrections are estimated in this analysis with a program called `HELIOS` (see section 7.4).

- $C_{b,j}$ the bin center correction defined as $C_{b,j} = \sigma_f/\sigma_{cog}$ determined with the Monte Carlo simulation. The cross section σ_{cog} which is measured at the center-of-gravity (Q^2_{cog}, y_{cog}) of bin j is corrected to the cross section σ_f at the values (Q^2_f, y_f) at which the proton structure function F_2 will finally be extracted, see table 7.2.

The acceptance and the bin center correction are calculated with the Monte Carlo `PHOJET`. As mentioned in section 3.1.1 the `PHOJET` MC is reweighted to the parameterization ALLM97, which gives a good description of the measured structure function F_2.

By substituting the definition of the acceptance A_j in equation 7.1 one obtains the so-called "Monte Carlo Method":

$$\frac{d^2\sigma}{dydQ^2} = \left[\frac{\sum_{i=1}^{N_j}\epsilon_i^{-1} - N_{bkg,j}}{N^{MC}_{rec,j}}\right]\frac{\mathcal{L}^{MC}}{\mathcal{L}_{\text{int}}}\frac{1}{1+\delta_{r,j}}C_{b,j}\frac{\Delta^2\sigma^{MC}_{gen}}{\Delta y\Delta Q^2}$$

with $\frac{\Delta^2\sigma_{gen}^{MC}}{\Delta y \Delta Q^2}$ the differential cross section on generator level, $N_{rec,j}^{MC}$ the number of reconstructed MC events in bin j after all selection cuts and $\mathcal{L}^{MC}$ the integrated luminosity of the MC event sample.

Extraction of the Proton Structure Function F_2

The relation between the double differential cross section $\frac{d^2\sigma}{dydQ^2}$ and the structure functions F_2 and F_L has been introduced in chapter 1.2. The proton structure function F_2 is given by:

$$F_2 \;=\; \frac{yQ^4}{2\pi\alpha^2}\left[2(1-y)+\frac{y^2}{1+R}\right]^{-1}\frac{d^2\sigma}{dydQ^2}$$

with $\frac{d^2\sigma}{dydQ^2}$ determined from relation 7.1 and $R = \sigma_T/\sigma_L = F_L/(F_2 - F_L)$. At low y ($y \approx 0.1$) the influence of F_L is negligible and thus the determination of the cross section can be interpreted as a direct determination of F_2. At high y the F_L contribution becomes large and in order to extract the structure function F_2 one needs to assume a certain parameterization of F_L resp. R. In the present analysis the following parameterization of R by Badelek et al. [58] is used:

$$R = \frac{0.165 \cdot Q^2}{m_\rho^2}$$

with $m_\rho = 0.77$ GeV the mass of the ρ meson.

Based on relation 1.18 the virtual photon-proton cross section $\sigma_{tot}^{\gamma^* p}$ may be calculated using the following relation:

$$\sigma_{tot}^{\gamma^* p} = \frac{4\pi^2\alpha}{Q^2} F_2(x, Q^2).$$

7.2 Selection of Bins

All studies carried out in regard of the bin selection are based on a large sample of PHOJET Monte Carlo events. As mentioned in the previous section the proton structure function F_2 will be determined in bins of finite size in Q^2 and y. The choice of these bins is made according to various requirements.

The geometrical acceptance of the VLQ spectrometer limits the accessible phase space in Q^2 and x. The dashed lines in figure 7.1 indicate the range of polar angles covered by the VLQ: $178.54° \lesssim \Theta_e \lesssim 179.1°$. Additionally the kinematic acceptance is restricted to the range of $y_e < 0.7$ (dotted line) due to the low trigger efficiency above this value, see section 5.2.2. In the remaining phase space the bins are then chosen such that the bin quality factors purity P and stability S are typically above 40 %. Purity P, efficiency E and stability S for a given bin are defined as follows:

$$P = \frac{N_{gen+rec}^{MC}}{N_{rec}^{MC}} \qquad E = \frac{N_{gen+rec}^{MC}}{N_{gen}^{MC}} \qquad S = \frac{N_{gen+rec}^{MC}}{N_{gen+sel}^{MC}}$$

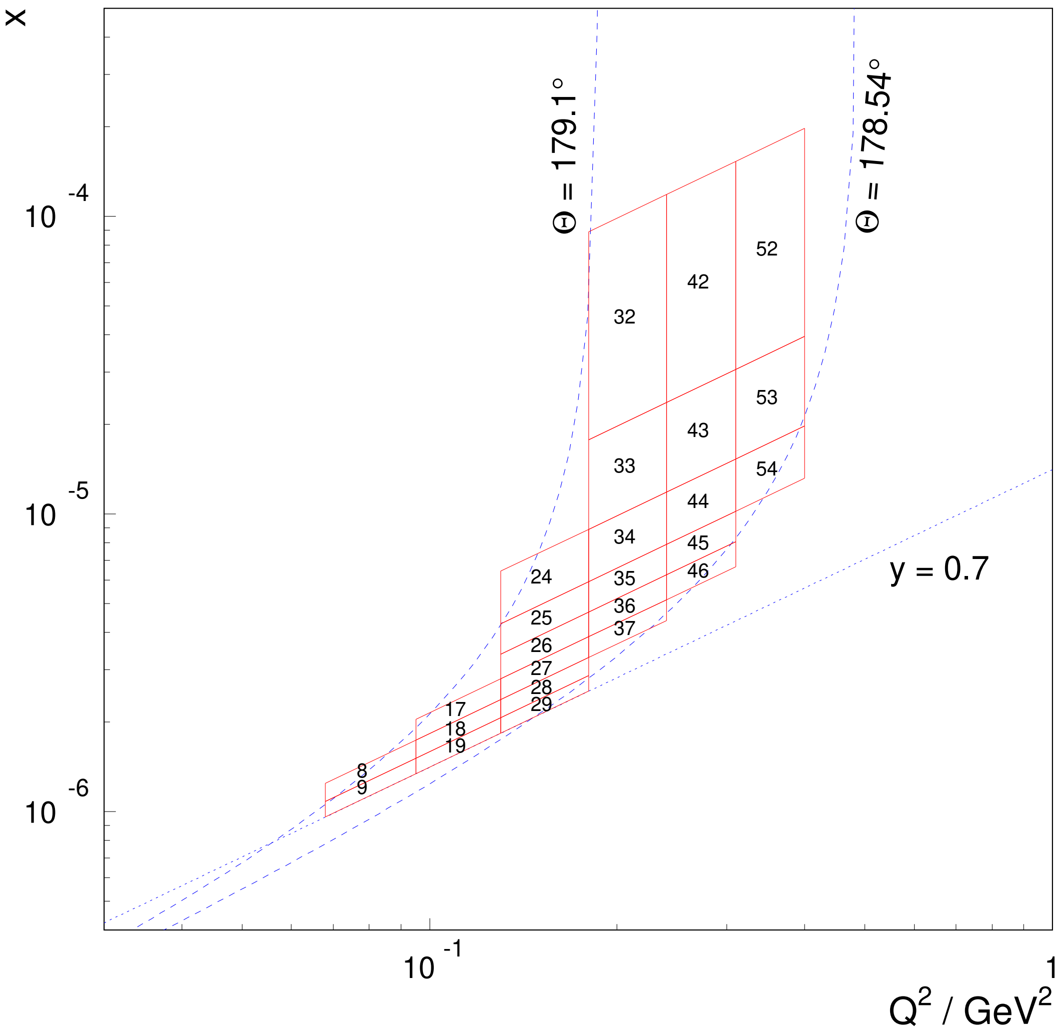

Figure 7.1: *Selected Q^2-y bins in the Q^2-x phase space. The geometric acceptance $178.54^\circ \lesssim \Theta_e \lesssim 179.1^\circ$ (dashed line) and the y-cut due to the decreasing trigger efficiency of the VLQ spectrometer (dotted line) are indicated.*

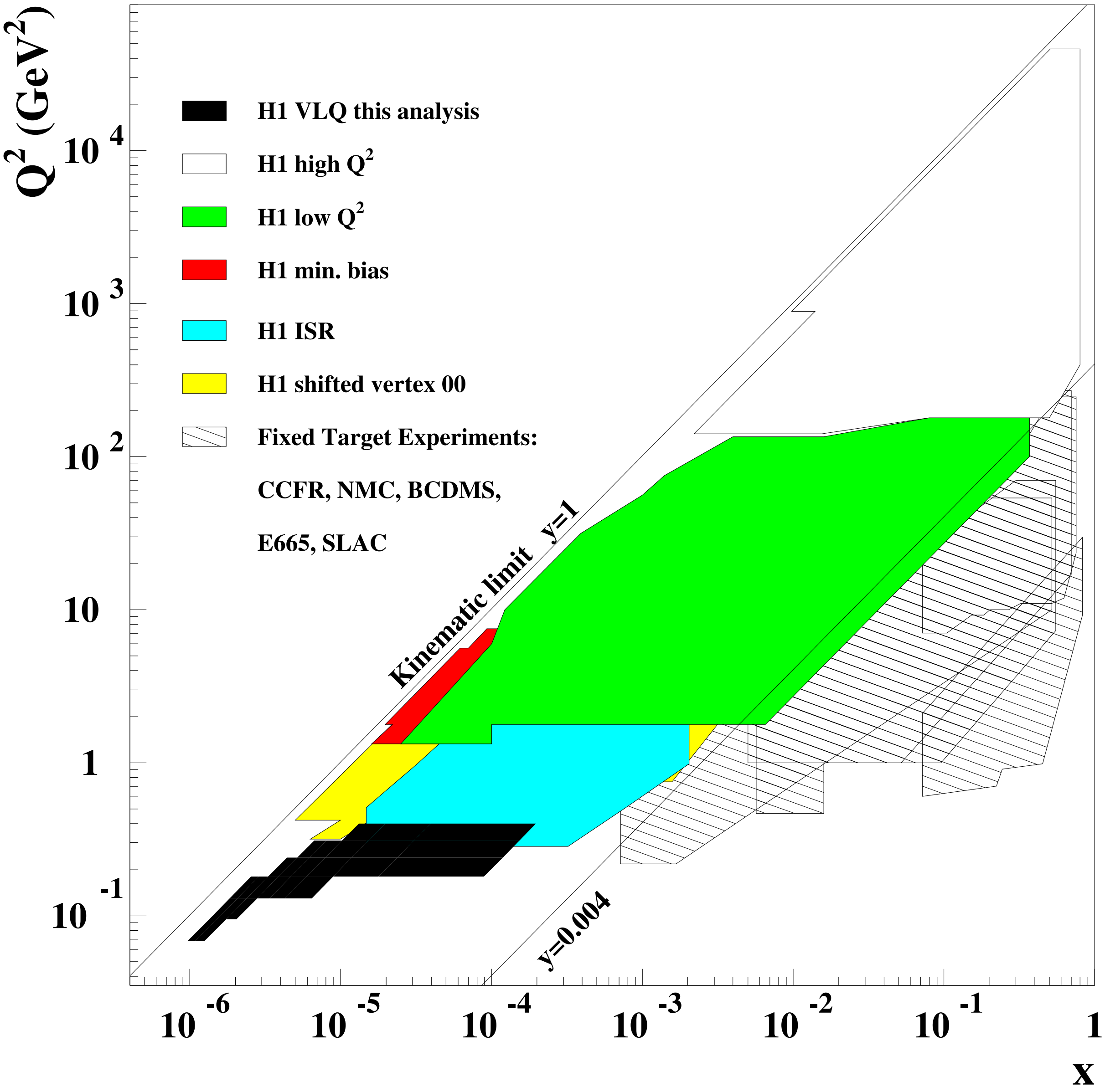

Figure 7.2: *Kinematic coverage of this analysis in the Q^2-x phase space in comparison to various other analyses of the H1 collaboration. Also shown is the phase space covered by fixed-target experiments.*

where $N^{MC}_{gen+rec}$ denotes the number of events that enter the same bin on generator and reconstruction level, N^{MC}_{rec} resp. N^{MC}_{gen} the number of events that are reconstructed resp. generated in this bin and $N^{MC}_{gen+sel}$ the number of events which are generated in this bin and pass all selection cuts on the reconstruction level. The purity P measures the migrations between bins due to the limited detector resolution. The efficiency E takes into account the limited geometrical acceptance of the VLQ spectrometer in azimuth as well as the effect of the selection cuts on the total number of generated events in a bin. Finally the stability S determines the influence of the detector resolution and the selection cuts.

The final binning is illustrated in figure 7.1 and the bin boundaries in Q^2 and y are listed in table 7.1. Bins at the edge of the kinematic acceptance are dropped if the center-of-gravity of the bin is outside the kinematic limits. The numbering scheme of the selected bins, shown in figure 7.1, will later be useful in the investigation of the systematic uncertainties.

Bin boundaries in Q^2 / GeV^2						
0.068	0.095	0.13	0.18	0.24	0.31	0.4

Bin boundaries in y								
0.02	0.1	0.2	0.3	0.38	0.46	0.54	0.62	0.7

Table 7.1: *Bin boundaries in Q^2 and y.*

The kinematic coverage of the H1 experiment and of several fixed target experiments is shown in figure 7.2. This analysis extends the measurement of inclusive NC cross sections to low Q^2 and very low x. A small region of overlap with the ISR analysis of 1997 and the shifted vertex analysis of 2000 is reached, in which the results of the different measurements can be compared.

Figure 7.3 shows the quality factors for the selected bins, with the purity P as the upper value, the efficiency E the middle value and the stability S as the lower value. The bin number is given in the upper left corner of each diagram. Purity and stability are above 40 % for each bin which indicates that the migrations between bins are low. It is therefore valid to unfold the data by the bin-by-bin unfolding method. The values for the efficiency E are low (0.6 - 11%) due to the limited azimuthal coverage of the VLQ spectrometer.

The fractional resolution of the kinematic variables Q^2 and y reconstructed with the Electron Method is shown in figures 7.4 and 7.5 for each bin. The bin number is indicated in the upper left corner of each diagram. These distributions estimate the effect of the limited resolution of the VLQ spectrometer and are defined as follows:

$$\sigma(Q^2) = \frac{Q^2_{rec} - Q^2_{gen}}{Q^2_{gen}} \qquad \sigma(y) = \frac{y_{rec} - y_{gen}}{y_{gen}}$$

where Q^2_{rec} resp. y_{rec} denotes the reconstructed value of the kinematic variable and Q^2_{gen} resp. y_{gen} the 'true' generated value. The resolution of the Electron Method in Q^2 is

Bin # Purity
Efficiency
Stability

Y \ Q^2 / GeV^2	0.0815	0.1125	0.155	0.21	0.275	0.355
0.06				32 59.1 2.1 47.6	42 61.7 7.9 46.9	52 60.8 6.8 45.1
0.15				33 47 5.1 55.1	43 48.1 10.6 54.8	53 48.3 6.1 52.1
0.25			24 49.9 1.3 56	34 51.9 8.8 56.8	44 50.1 8.7 53.9	54 48.4 2.5 48.7
0.34			25 49.8 3.6 54.2	35 49.3 9.9 52.9	45 49 5.5 49.4	
0.42			26 51.8 7.2 55.3	36 49.1 8.6 53.1	46 47.7 2.4 45.8	
0.5		17 50.1 2.6 52.5	27 54.2 9.8 55.6	37 55 5.9 53.7		
0.58	8 48.6 0.6 47.2	18 52.1 7.5 56.7	28 52.4 8.9 56.2			
0.66	9 52.6 4.4 55.5	19 54.2 10 56.6	29 49.3 3.7 49.4			

Figure 7.3: *The quality factors purity (upper value), efficiency (middle value) and stability (lower value) for the selected Q^2-y bins. The bin number is given in the upper left corner of each diagram.*

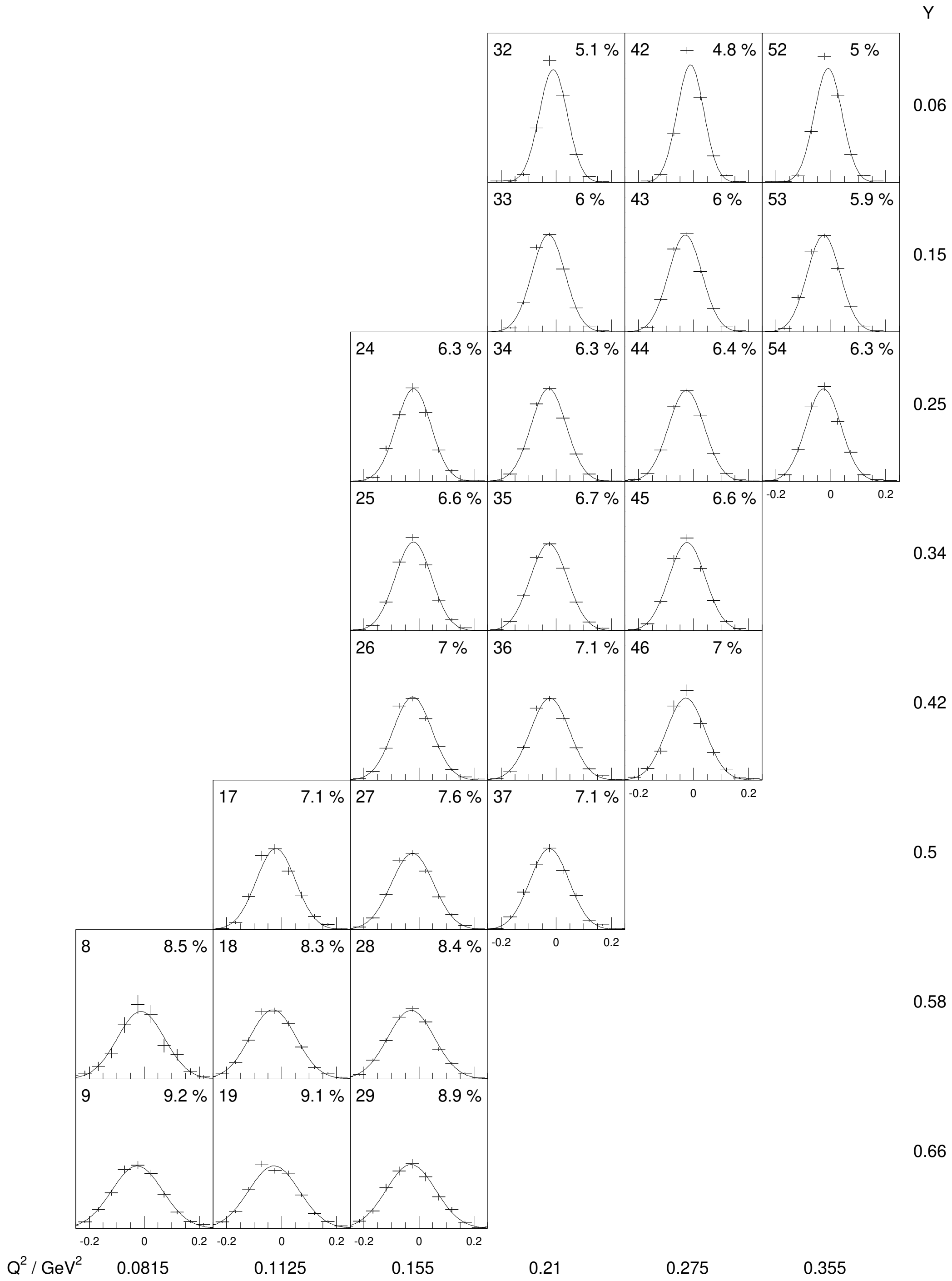

Figure 7.4: *Fractional resolution of the kinematic variable Q^2 reconstructed with the Electron Method in the selected Q^2-y binning. The resolution (in %) determined with a Gaussian fit is shown for each bin. The bin number is given in the upper left corner of each diagram.*

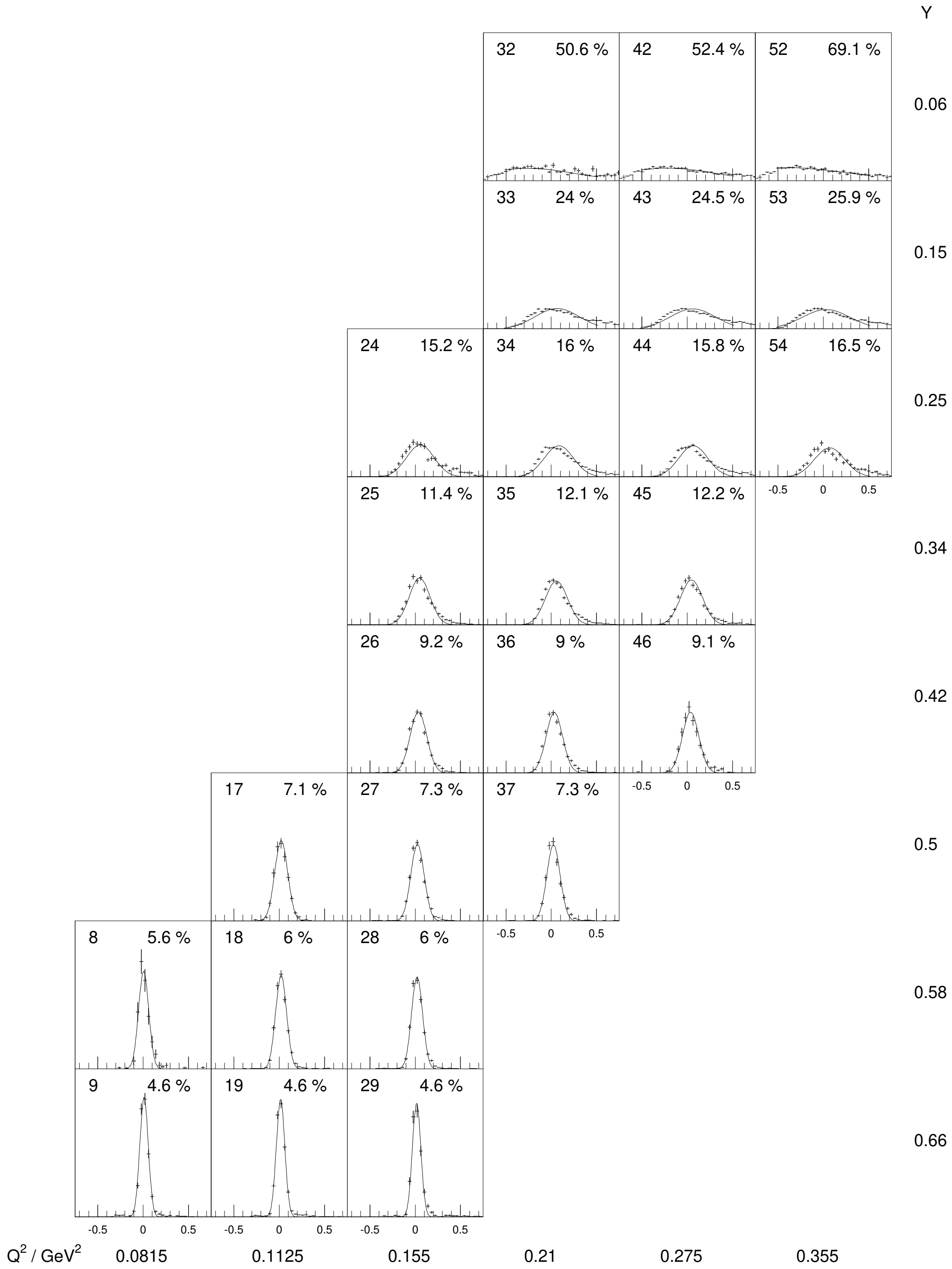

Figure 7.5: *Fractional resolution of the kinematic variable y reconstructed with the Electron Method in the selected Q^2-y binning. The resolution (in %) determined with a Gaussian fit is shown for each bin. The bin number is given in the upper left corner of each diagram.*

approximatively constant over the whole kinematic range while the y resolution dramatically drops with decreasing y values due to the y-dependence of the uncertainties in the Electron Method, see section 2.3.1.

In table 7.2 the central values of the Q^2-y bins in which the proton structure function F_2 will be determined are listed. The bin-center correction from the arithmetic central values of the bins to these final values are less than 3% for all bins.

Bin centers in Q^2 / GeV^2					
0.08	0.11	0.15	0.21	0.27	0.35

Bin centers in y							
0.06	0.15	0.25	0.34	0.42	0.50	0.58	0.66

Table 7.2: *Bin center values for Q^2 and y used in the determination of the proton structure function F_2.*

7.3 Comparison of Data and MC

In this section control distributions of simulated events are compared to the data. The results of the alignment (section 4.2.2) and the calibration (section 4.2.1) of the VLQ spectrometer are included in the reconstruction of the kinematic variables for the data as well as for the simulated events. The efficiencies determined in section 5.2 are applied. The events in both data and MC sample are selected according to the criteria summarized in section 6.7. As mentioned in section 3.1.1 the events in the Monte Carlo are reweighted to the ALLM97 parameterization, which gives a good description of the cross section measured in this analysis. In the distributions the luminosity of the MC sample is scaled to the luminosity of the data. In each distribution the empty histogram represents the sum of the contributions from the PHOJET Monte Carlo and from the photoproduction Monte Carlo (γp MC). In addition the distribution from the γp MC is shown separately in the shaded histogram.

Figure 7.6 shows the distributions of the energy of the electron candidate in the upper and in the lower module in the whole accessible kinematic range (without the binning in Q^2 and y). The data distributions are well described by the MC. The discrepancies at low energies are due to the trigger threshold of the VLQ_low_OR trigger element, see section 5.2.2, which is not included in the simulation. In the measurement of F_2 the region $y > 0.7$ is rejected due to the low trigger efficiency. The distributions of the polar angle θ and the azimuthal angle ϕ are given in the Q^2-y binning used in the determination of the proton structure function F_2. The energy distribution measured by the VLQ spectrometer in the selected Q^2-y bins is given in figure 7.7. The discrepancies at high energy values may be due to the fact that the PHOJET MC does not include radiative corrections. The inclusion of QED radiative effects

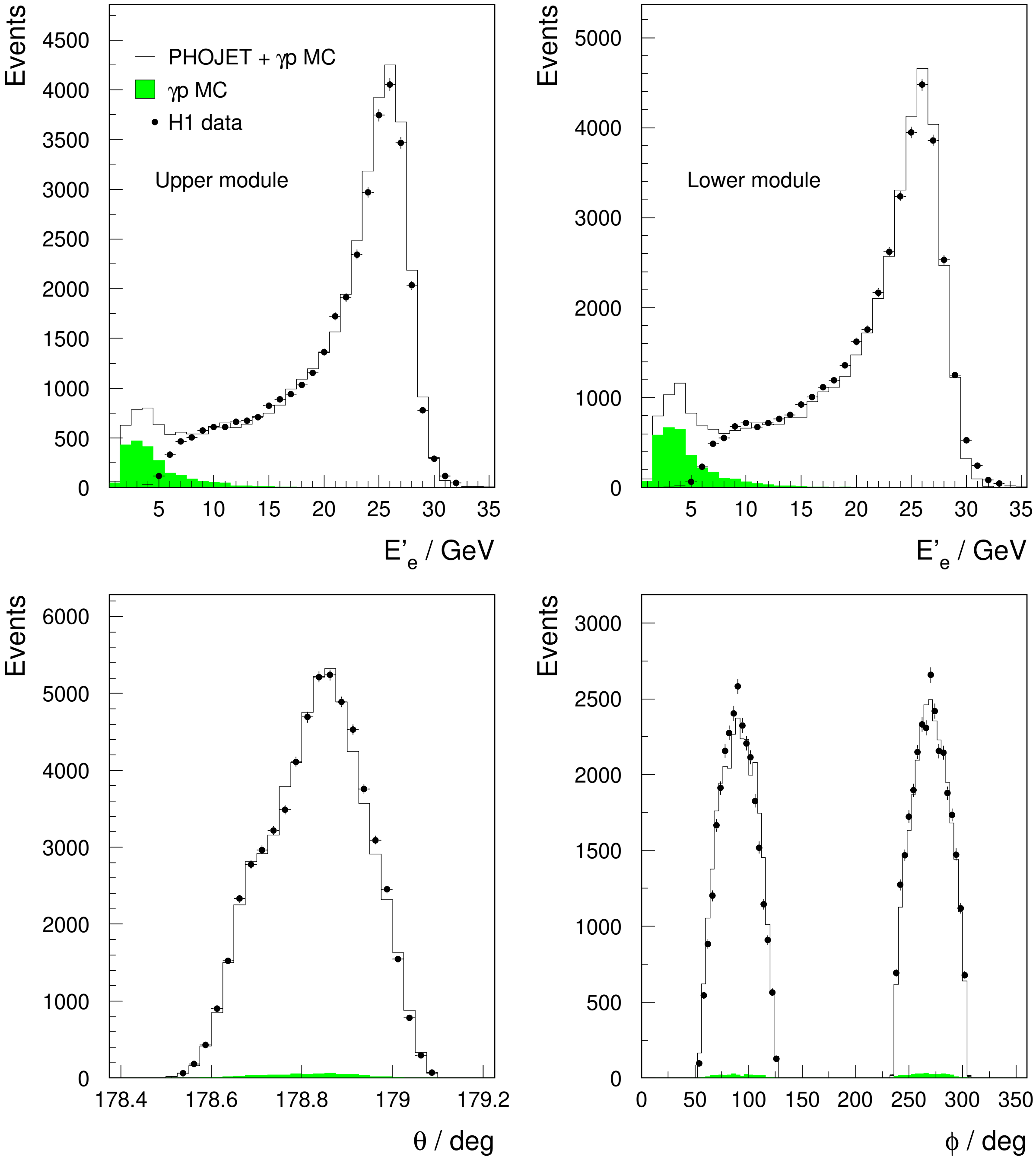

Figure 7.6: *The distributions of the energy in the upper module (upper left diagram) and in the lower module (upper right) are shown over the whole kinematic range. The distributions of the polar angle θ (lower left) and of the azimuthal angle ϕ (lower right) of the electron candidate are shown in the selected Q^2-y bins. Distributions are shown for data (points), Monte Carlo (*`PHOJET`*+γp MC; empty histogram) and γp MC (shaded histogram).*

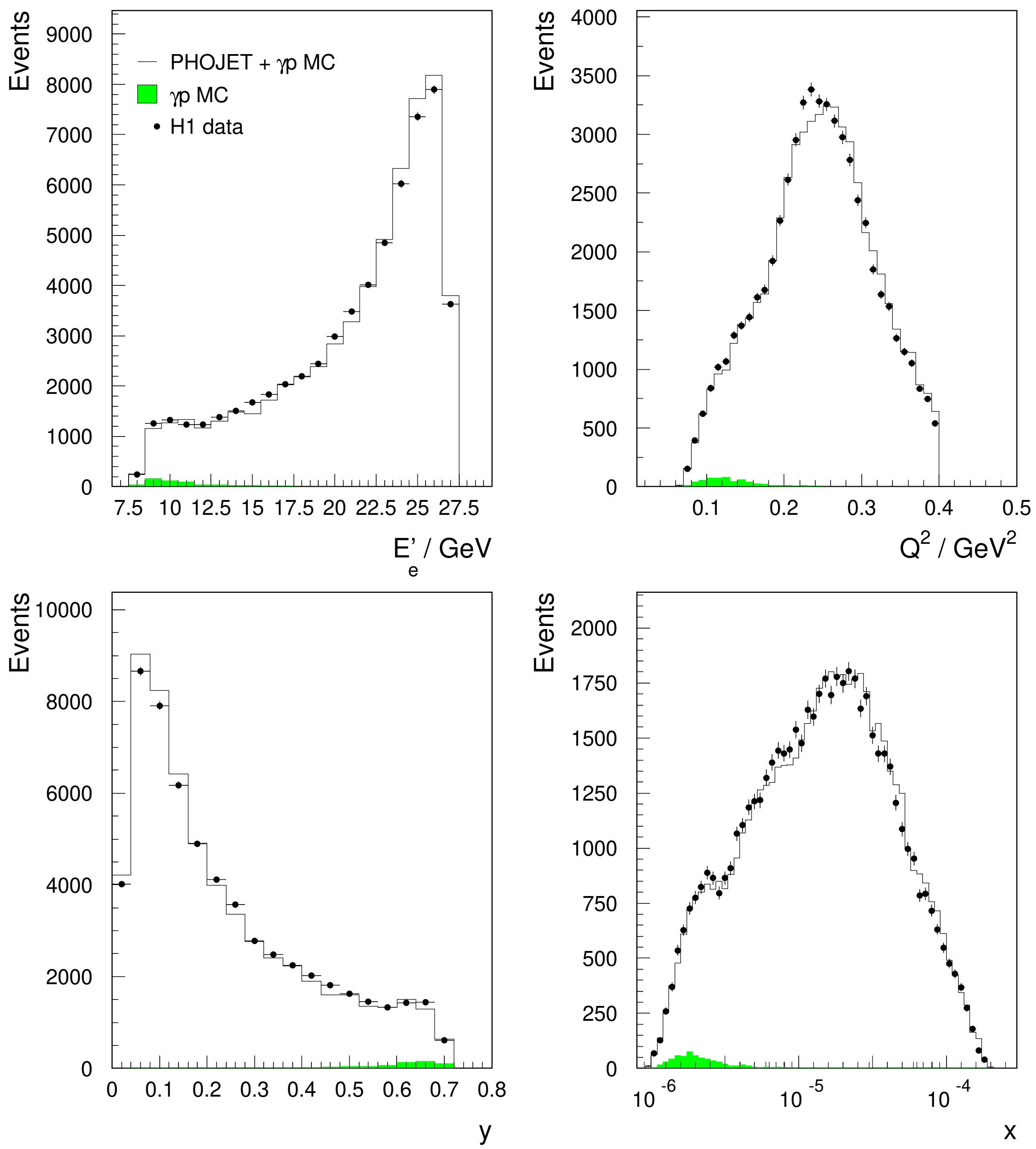

Figure 7.7: *The distributions of the energy of the electron candidate (upper left diagram) and the kinematic variables Q^2 (upper right), y (lower left) and x (lower right) reconstructed with the Electron Method. Distributions are shown for data (points), Monte Carlo (PHOJET+γp MC; empty histogram) and γp MC (shaded histogram). All plots are shown in the selected Q^2-y bins.*

would lead to a shift of events towards lower energies. The radiative corrections to the cross section, calculated with `HELIOS` (section 7.4) are only later applied during the unfolding procedure (section 7.1). The influence of radiative corrections are discussed in the following section.

As the energy as well as the polar and the azimuthal angle of the electron candidates are all well described by the MC, one would expect a good agreement between data and MC in the distributions of the kinematic variables Q^2, y and x reconstructed with the Electron Method. This is indeed the case as one can see in figure 7.7 for the distributions of Q^2, y and x.

Overall the agreement between data and MC in the distributions concerning the measurement of the electron candidate is good. Unfortunately this is not the case for distributions including the measurement of the hadronic final state. The variable $E - P_z$ of an event is defined by the following equation: $E - P_z = \sum_{i=1}^{N}(E_i - P_{z,i}) = 2 \cdot E_0$ where the sum runs over all particles of the final state and E_0 is the energy of the incoming electron. The $E - P_z$ distributions of the data and MC are shown in figure 7.8. The data distribution shows a large tail towards low values of $E - P_z$, which is caused by initial state radiation of photons. In this case E_0 is reduced by the photon energy resulting therefore in a decreased value of $E - P_z$. QED radiative corrections including ISR are not implemented in the `PHOJET` Monte Carlo.

The variable y_{balance} is defined as follows:

$$y_{\text{balance}} = \frac{y_{\text{had}}}{y}$$

with y_{had} the inelasticity measured with the Hadron Method and y determined with the Electron Method. The distributions of y_{balance} in data and MC show a peak at the expected value of 1. The MC falls then steeply off to lower values of y_{balance} while the data distribution becomes flat. The reason for this behaviour is illustrated in the distributions of y_{had} in figure 7.8. Both diagrams, on a linear and on a logarithmic scale, exhibit an excess of the data relative to the MC at low values of y_{had}. This excess results then in the plateau seen in the y_{balance} distribution. In the following section it will be shown that these discrepancies in the description of the hadronic final state vanish if radiative corrections are applied to the MC.

Figure 7.9 shows the distributions of E_{had} and η_{max}. Both data distributions are well described by the MC after the cut on the energy of the hadronic final state $E_{had} > 5$ GeV. The η_{max} distribution indicates that the diffractive contribution ($\eta_{max} < 3$) in the selected data sample is well modeled by the MC, in contrast to the low energy region, see section 6.4.

The bin-by-bin unfolding method used in the measurement of the NC cross section (described in section 7.1) relies on the accurate description of the data distributions by the simulated events. As all relevant kinematic variables reconstructed with the Electron Method show a good agreement between data and MC, the procedure to measure the cross section can be carried out. The hadronic final state only influences the cross section measurement indirectly through the requirement of a primary interaction vertex and the cut on the energy.

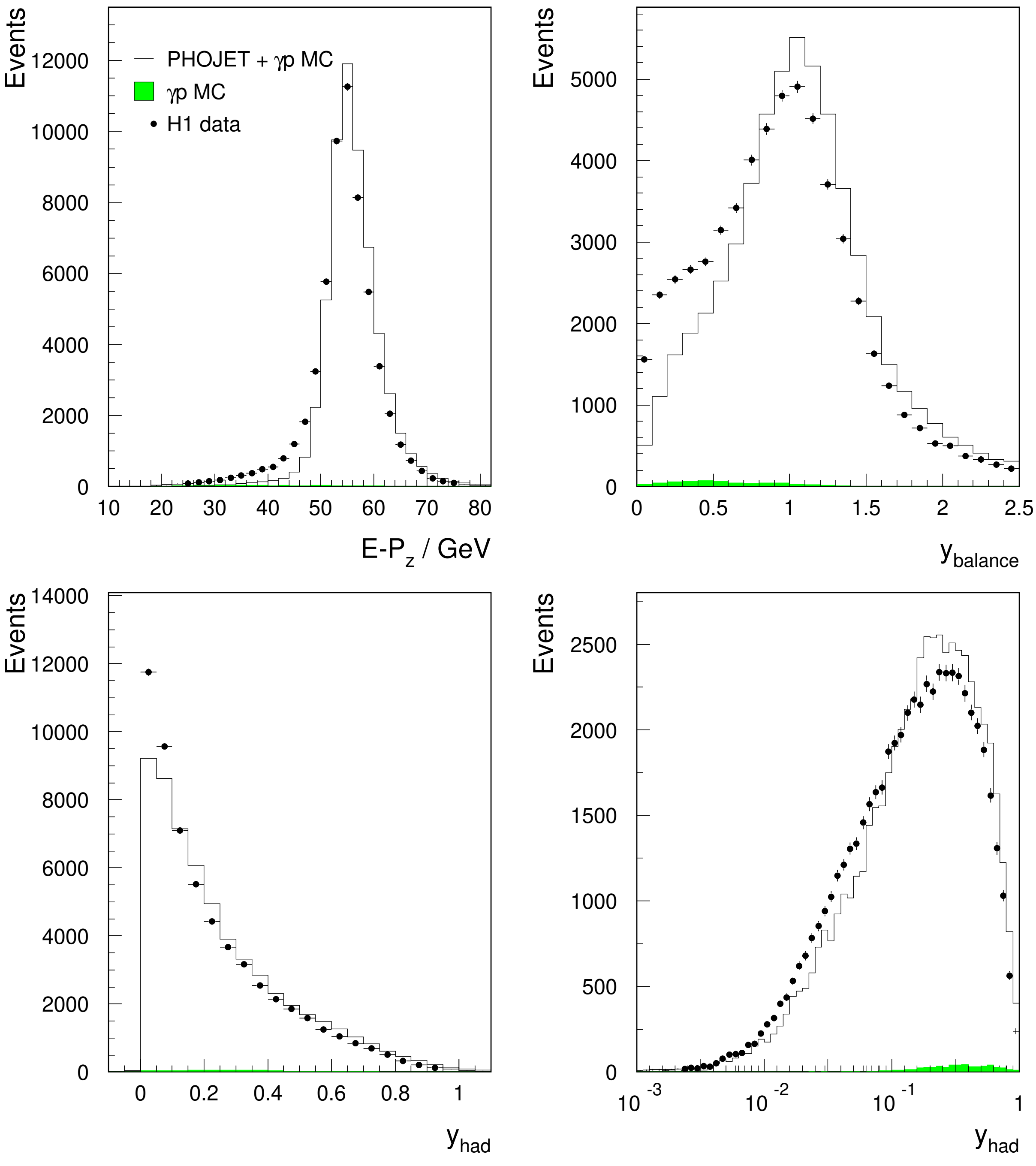

Figure 7.8: *The distributions of $E - P_z$ (upper left diagram), $y_{\rm balance}$ (upper right) and $y_{\rm had}$ on a linear (lower left) and a logarithmic scale (lower right). Distributions are shown for data (points), Monte Carlo (PHOJET+γp MC; empty histogram) and γp MC (shaded histogram). All plots are shown in the selected Q^2-y bins.*

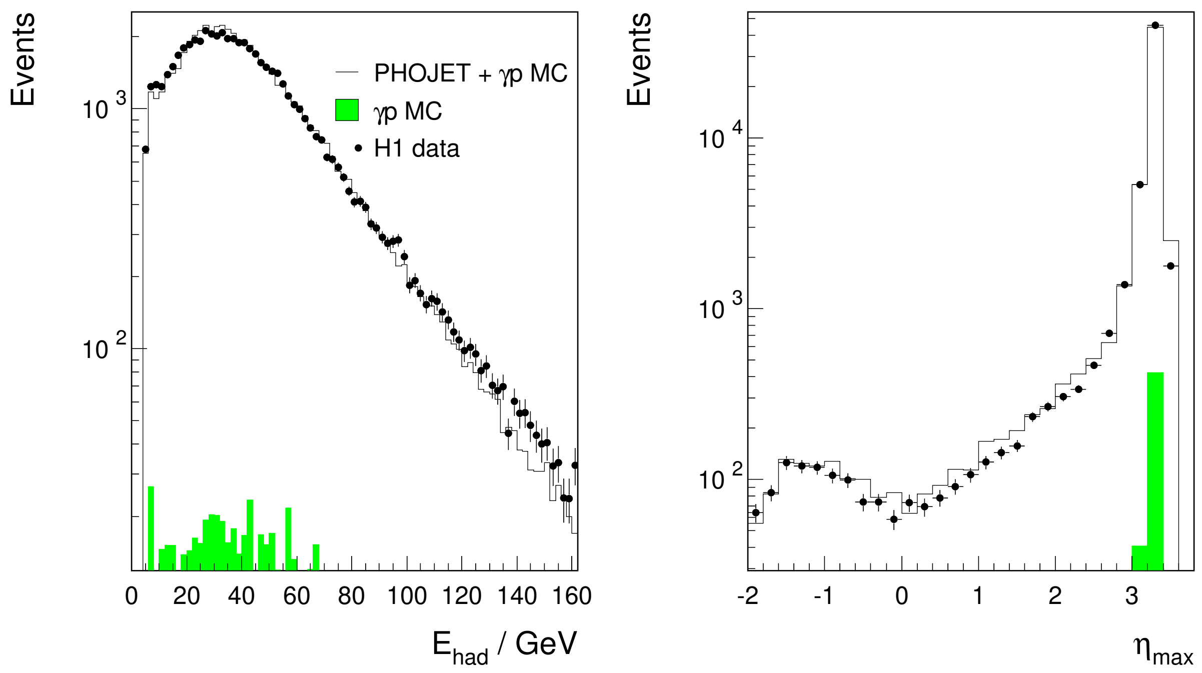

Figure 7.9: *The distributions of E_{had} and η_{max} for data (points), Monte Carlo (PHOJET+γp MC; empty histogram) and γp MC (shaded histogram). All plots are shown in the selected Q^2-y bins.*

The efficiency corrections are applied to the simulated events as as a function of y_{had}. The discrepancies in the description of the hadronic final state are therefore taken into account in the estimation of the systematic uncertainties.

7.4 Radiative Corrections

So-called radiative corrections in ep scattering arise from the additional emission or absorption of bosons (electromagnetic or weak) by the particles involved in the scattering process. The weak radiative corrections may be neglected as they are suppressed due to the high mass of the gauge bosons ($M_Z^2 \approx 80^2$ GeV^2) relative to the scale of the analyzed phase space ($Q^2 < 1$ GeV^2). The remaining radiative corrections are suppressed by the coupling strength α_{em}. Radiative corrections will lead to two characteristic signatures in the final state. In initial state radiation (ISR) a photon is radiated off the incoming lepton resulting in a reduced center-of-mass energy of the ep scattering process. In final state radiation (FSR) the scattered electron radiates a photon. In this case the angle between electron and photon is most likely small and the photon is included in the electromagnetic shower in the VLQ calorimeter.

Figure 7.10 shows the $y_{\rm had}$ and $y_{\rm balance}$ distributions in comparison to the DJANGOH MC which includes radiative corrections, see section 3.1.2. The DJANGOH MC does not describe

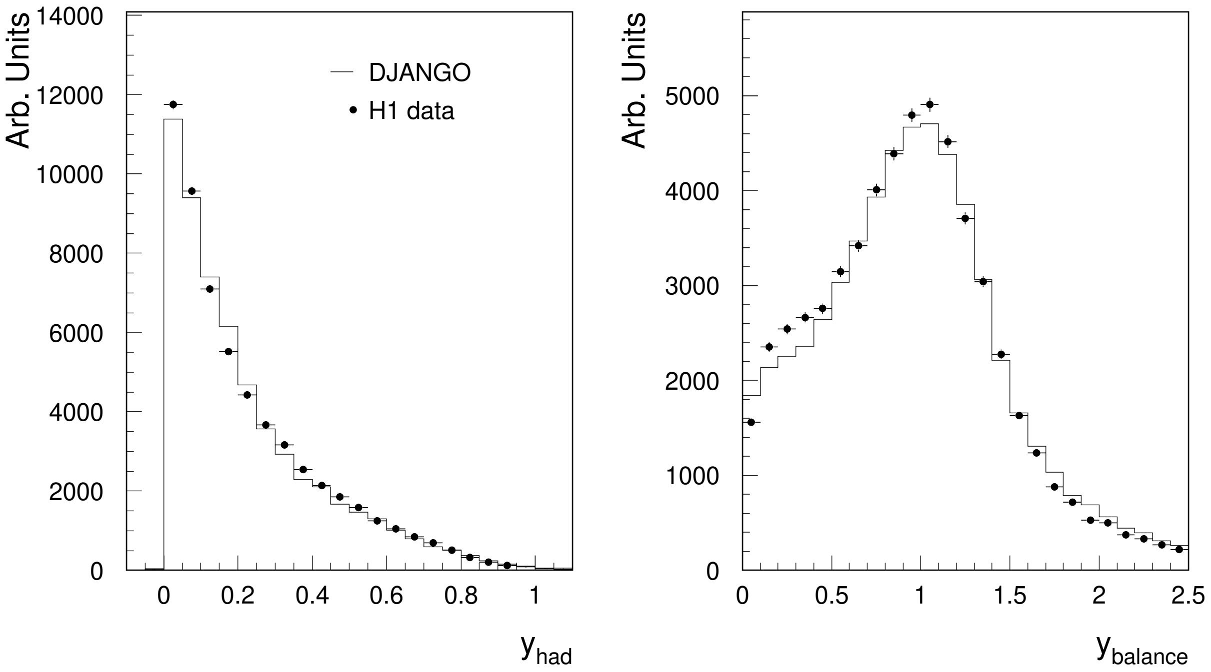

Figure 7.10: *The distributions of y_{had} and y_{balance} for data (points) in comparison to the DJANGOH MC (histogram). Plots are shown in the selected Q^2-y bins. The normalization scale is arbitrary.*

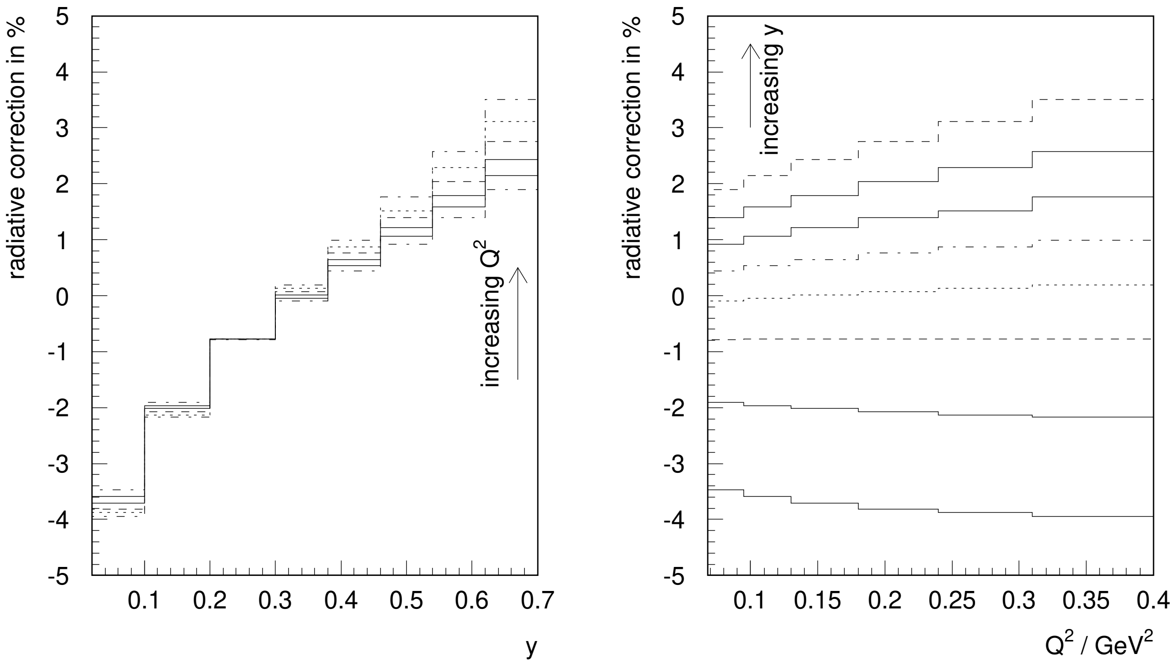

Figure 7.11: *Radiative corrections in the VLQ phase space in dependence of y for different Q^2 bins (left). The right plot shows the radiative corrections in dependence of Q^2 for different y bins.*

the overall normalization of the data distribution, therefore the MC distribution is scaled to the data. The radiative MC gives a much improved description of the data at low y_{had} and low y_{balance}. This indicates that the discrepancies between data and PHOJET are due to the missing QED corrections.

The effect of the radiative processes on the measurement of the cross section depends on the detector acceptance, on the selection cuts and on the choice of the reconstruction method (see section 2.3.1). Therefore measured cross sections need to be corrected for real γ emission on a bin by bin basis, see section 7.1. In this analysis the radiative corrections are estimated with a program called HELIOS which is included in the software package HECTOR [59]. HELIOS allows the calculation of QED corrections in leading logarithmic approximation including higher order corrections to NC scattering. In figure 7.11 the radiative corrections $\delta_{r,j}$ for the Electron Method in the VLQ phase space are shown with the following definition:

$$\delta_{r,j} = \frac{\sigma_{rad,j} - \sigma_{Born,j}}{\sigma_{Born,j}}$$

where σ_{rad} is the cross section in a bin j including all radiative processes and σ_{Born} is the cross section on Born level. The left diagram shows the radiative corrections $\delta_{r,j}$ in dependence of Q^2 for different y bins and on the right hand side $\delta_{r,j}$ is given in dependence of y for different Q^2 bins. While the y dependence of $\delta_{r,j}$ is large at a given Q^2 the Q^2 dependence is small. For each bin the radiative corrections are smaller than 4%.

7.5 Systematic Uncertainties

The measurement of a cross section necessarily includes the determination of the accuracy of the measurement. Several sources restrict the achievable accuracy like uncertainty in the position determination of the detector, uncertainty in the energy scale etc. To estimate the contribution from the different sources, every source is varied separately by one standard deviation upwards and downwards and subsequently the selection criteria are applied. The relative uncertainty δ of a source is then given by the resulting difference in the measurement of the cross section σ_{varied} to the central value of the cross section $\sigma_{\mathrm{central}}$:

$$\delta = \frac{\sigma_{\mathrm{varied}} - \sigma_{\mathrm{central}}}{\sigma_{\mathrm{central}}}$$

The total systematic uncertainty for a bin is then given by the quadratic sum of the individual systematic uncertainties of every source. Finally the total uncertainty of the cross section measurement is given by the total systematic error and the statistical uncertainty added in quadrature.

In the following all relevant sources of uncertainty will be described and their influence on the measurement will be evaluated. The variations by one standard deviation upwards and downwards will be done in the Monte Carlo, if not stated differently. The contributions from the single sources to the systematic uncertainties for the F_2 bins are shown in figure 7.12. The full circles represent the variation by one standard deviation upwards and the open circles the variation by one standard deviation downwards. The total positive and negative systematic uncertainty for a particular bin is then obtained by adding the positive and negative contributions from all sources in quadrature. The statistical error, the total systematic error[1] and the total error for each bin are given in the lower diagram of figure 7.12.

Statistical Uncertainty

The restricted amount of events available in the measurement of a cross section results in statistical uncertainties. Two sources contribute to the total statistical uncertainty: the limited number of events in the data sample used in the determination of the cross section and the limited number of events in the Monte Carlo sample used in the unfolding procedure. In this analysis the MC sample contains approximatively twice the statistics of the data set, see section 3.1.1. Both contributions are added in quadrature. The lower plot in figure 7.12 shows that for all bins the total statistical error is smaller than the total systematic uncertainty.

VLQ Energy Scale

The uncertainty of the energy scale has been determined to 0.5% at the kinematic peak (see section 4.2.1) and to 1% at medium energies (see section 4.2.2). Thus the energy scale in the MC is varied by the following parameterization $\pm 0.005 \cdot \frac{27.5}{E}$ with E the measured energy in the VLQ calorimeter. The resulting change in the cross section measurement can be seen in diagram (a) of figure 7.12.

VLQ Alignment

The accuracy of the alignment procedure outlined in section 4.2.2 was estimated to 0.5 mm in y-direction. The position of the VLQ calorimeters is varied by ± 0.5 mm in the MC and afterwards the reconstruction of the calorimetric cluster is repeated. The resulting uncertainty can be seen in diagram (b) in figure 7.12. The accuracy of the alignment in x direction has only a negligible influence on the cross section.

VLQ Fiducial Cut

The boundaries of the VLQ fiducial area in y-direction (y>5.2 cm for the upper and y<-5.8 cm for the lower module, see section 6.2) are varied by ± 1 mm. The variations of the fiducial cut are applied in data and Monte Carlo (see diagram (c) in figure 7.12). A variation of the

[1] In case of asymmetric total systematic errors the larger uncertainty is shown.

radius cut (6.5 cm for the upper and 7.5 cm for the lower module) by ± 1 mm has only a small influence on the cross section ($< 0.5\%$) and is not shown in figure 7.12.

Inclusive VLQ Trigger Efficiency

The efficiencies of the inclusive VLQ triggers s46 and s49 are varied in the data by the statistical uncertainty of the efficiency determination following a binomial distribution. This variation has only an influence on the cross section in the region of low electron energies ($E \leq 12$ GeV), where the efficiency is below 1 (see diagram (d) in figure 7.12).

Vertex Efficiency

The efficiency of the vertex determination is varied by the statistical uncertainty of the efficiency determination in the simulation. The influence on the cross section is shown in diagram (e) of figure 7.12.

Luminosity Measurement

The uncertainty of the luminosity measurement is 1.5%. Therefore the resulting change δ due to the linear dependence of the cross section on the luminosity amounts to 1.5%. This contribution is not shown in figure 7.12.

Photoproduction Background

The photoproduction background which is statistically subtracted from the measured cross section is varied by $\pm 30\%$ (see diagram (f) in figure 7.12).

Fraction of Diffractive Events

The contribution of diffractive subprocesses to the total cross section is varied by +100% and -50% in the PHOJET MC (see diagram (g) in figure 7.12).

Cut on E_{had}

The cut on the energy of the hadronic final state is varied in data and MC by ± 2 GeV (see diagram (h) in figure 7.12).

Scale of the Hadronic Energy Measurement

The hadronic energy scale only influences the measurement of F_2 through the cut on E_{had} and through the reweighting of the vertex efficiencies in the simulation. The impact on F_2 is thus small ($\approx 0.5\%$, see figure 7.12 (i)).

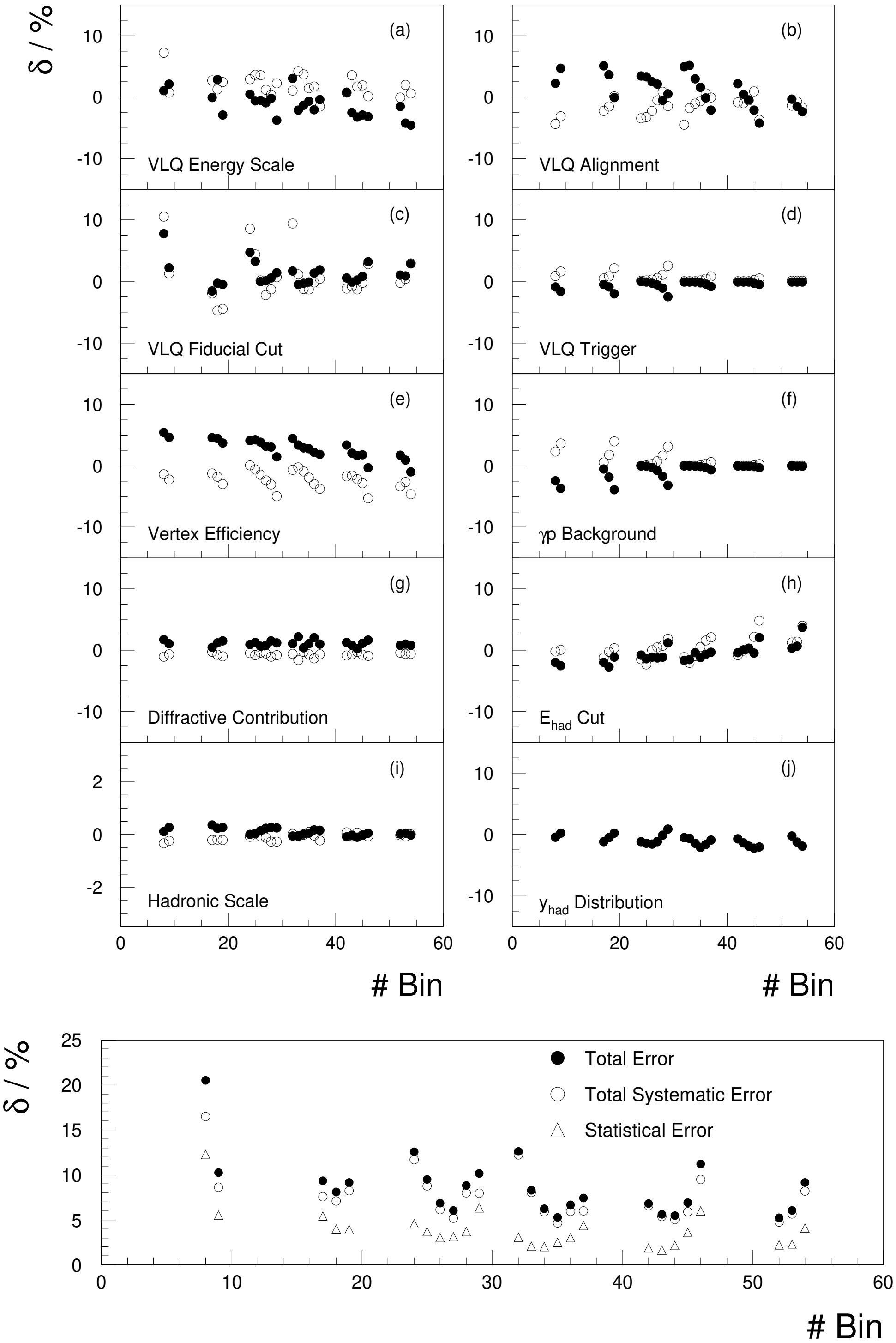

Figure 7.12: *Systematic uncertainty δ on the cross section measurement for each source as a function of the bin number. Variations by one standard deviation upwards (full circles) and by one standard deviation downwards (open circles) are shown. The lower diagram illustrates the statistical (open triangles), the total systematic (open circles) and the total error (full circles) on the cross section measurement.*

Measurement of the hadronic final state in the data and MC

The lower plots in figure 7.8 illustrates the y_{had} distribution on a linear and on a logarithmic scale for the data and the simulated events. As discussed before, the data show a steeper rise towards low values of y_{had} than the Monte Carlo. This difference in shape may influence the measurement of the cross section as the efficiency correction for the vertex reconstruction are applied as a function of y_{had} in the simulation. To estimate the influence of the deviating y_{had} distributions, the correction procedure is inversed and the efficiencies are applied to the data events instead of the simulated events. The resulting systematic change is illustrated in figure 7.12 (j).
In general the total uncertainty, varies in the range of 5-12% with a statistical precision of $\approx 4\%$, except for bin 8 which shows a total systematic error of 18%.

7.6 Results

The proton structure function $F_2(x,Q^2)$ is shown in figure 7.13 as a function of x for different values of Q^2. The measurement covers the range of $0.08\ \mathrm{GeV}^2 < Q^2 < 0.35\ \mathrm{GeV}^2$ and $1.2 \cdot 10^{-6} < x < 5.8 \cdot 10^{-5}$ and extends the kinematic range of the H1 experiment in the region of low Q^2. In total 25 points are determined with a precision of 5-12%. The inner error bars represent the statistical error and the outer ones the total uncertainty, composed of the statistical error and the total systematic error added in quadrature. The value of R is taken from Badelek et al. (see section 7.1). The radiative corrections calculated with `HELIOS` are also included. The overlaid curves represent the parameterization ALLM97 used in the `PHOJET` Monte Carlo (see section 3.1.1) and the prediction from the fractal fit. Both models give a good description of the measured F_2.

In table 7.3 the results on the measurement of F_2 and $\sigma_{tot}^{\gamma^* p}$ are listed for each bin. The statistical uncertainties δ_{stat} and the total positive and negative uncertainties δ_{tot} (including the total statistical error) are shown. The relative change $\Delta_{\mathrm{R=0}}$ of the F_2 value when R is set to 0 is given. Moreover the kinematic values of the bin centers are listed.

Figure 7.14 shows the measurement of $F_2(x,Q^2)$ based on the main subtrigger s50 in comparison to the measurement based on the inclusive subtriggers s46 and s49. The error bars represent the statistical errors on the measurement. The results from the different subtriggers are in good agreement. Deviations only occur at the edge of the phase space in the region of low y, where a more detailed analysis of the inclusive data set would be needed.

Figure 7.15 shows the results of the F_2 measurement presented in this analysis (full circles) in comparison to the ZEUS BPT measurement from 1997 [5] (rescaled to the Q^2-y binning of the present analysis (see section 7.2)). Both measurements are in good agreement within one standard deviation. The fact that the error bars in the VLQ analysis are larger than in the BPT data is due to the large uncertainties introduced by the variation of the fiducial cut and the alignment for most of the bins. This sensitivity to the position of

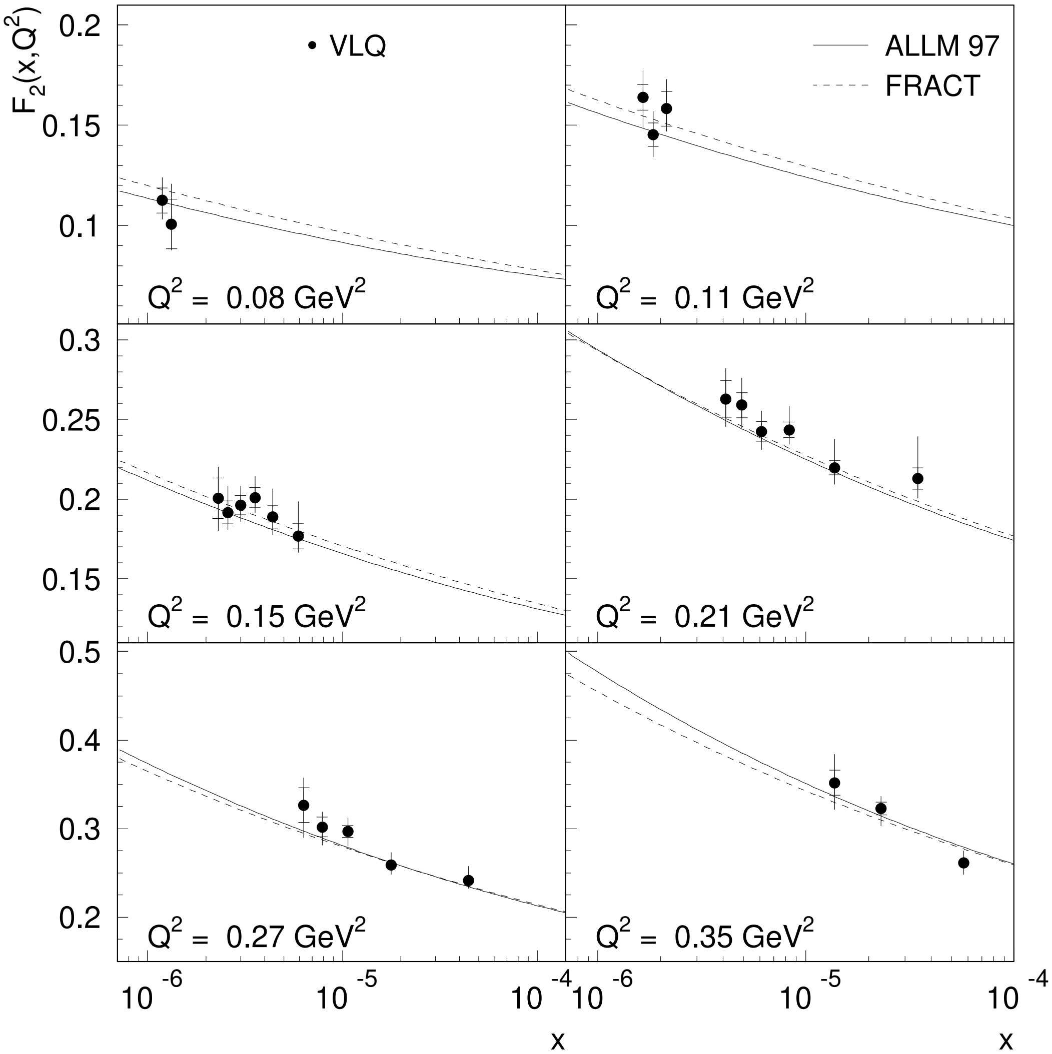

Figure 7.13: *The structure function $F_2(x,Q^2)$ as a function of x for different values of Q^2 (full circles) measured in this analysis. The solid curve shows the parameterization ALLM97 used in the* PHOJET *Monte Carlo.*

Bin	Q^2 (GeV^2)	y	x	$\Delta_{\mathrm{R}=0}$ (%)	δ_{stat} (%)	δ_{tot} (%)	(%)	$\sigma_{tot}^{\gamma^* p}$ (μb)	$F_2(x,Q^2)$ R_{Badelek}
8	0.080	0.580	0.136E-05	-0.63	12.26	20.53	-13.62	141	0.101
9	0.080	0.660	0.120E-05	-0.87	5.53	10.25	-8.45	158	0.113
17	0.110	0.500	0.217E-05	-0.61	5.45	9.33	-7.21	161	0.158
18	0.110	0.580	0.187E-05	-0.87	3.97	8.12	-7.63	148	0.145
19	0.110	0.660	0.164E-05	-1.19	3.96	8.21	-9.14	167	0.164
24	0.150	0.250	0.592E-05	-0.17	4.57	12.56	-6.26	132	0.177
25	0.150	0.340	0.435E-05	-0.33	3.68	9.50	-6.09	141	0.189
26	0.150	0.420	0.352E-05	-0.55	3.05	6.87	-4.80	150	0.201
27	0.150	0.500	0.296E-05	-0.83	3.10	6.04	-5.28	147	0.196
28	0.150	0.580	0.255E-05	-1.18	3.70	8.81	-5.83	143	0.192
29	0.150	0.660	0.224E-05	-1.61	6.36	9.76	-10.17	150	0.201
32	0.210	0.060	0.345E-04	-0.01	3.09	12.63	-6.10	114	0.213
33	0.210	0.150	0.138E-04	-0.07	2.05	8.30	-4.89	117	0.220
34	0.210	0.250	0.829E-05	-0.22	2.00	6.24	-3.86	130	0.244
35	0.210	0.340	0.609E-05	-0.44	2.52	5.30	-4.71	130	0.243
36	0.210	0.420	0.493E-05	-0.73	3.05	6.68	-5.55	138	0.259
37	0.210	0.500	0.414E-05	-1.10	4.37	7.41	-6.67	140	0.263
42	0.270	0.060	0.444E-04	-0.01	1.87	6.83	-3.82	100	0.241
43	0.270	0.150	0.178E-04	-0.09	1.63	5.62	-4.22	108	0.259
44	0.270	0.250	0.107E-04	-0.28	2.18	5.24	-5.48	123	0.297
45	0.270	0.340	0.783E-05	-0.57	3.60	5.60	-6.90	125	0.302
46	0.270	0.420	0.634E-05	-0.94	5.99	9.40	-11.22	136	0.326
52	0.350	0.060	0.575E-04	-0.02	2.20	5.26	-5.12	84	0.261
53	0.350	0.150	0.230E-04	-0.12	2.24	4.11	-6.07	104	0.323
54	0.350	0.250	0.138E-04	-0.36	4.07	9.16	-8.71	113	0.352

Table 7.3: *Results on the measurement of F_2 and $\sigma_{tot}^{\gamma^* p}$. The first four columns represent the bin number and the kinematic values of the bin centers in Q^2, y and x. $\Delta_{\mathrm{R}=0}$ gives the relative change of the F_2 value when R is set to 0. The statistical, the total positive and the total negative error are given in the next three columns. $\sigma_{tot}^{\gamma^* p}$ and $F_2(x,Q^2)$ are shown in the last two columns.*

the electromagnetic cluster is a consequence of the restricted spatial resolution of the VLQ calorimeters in comparison to the spatial resolution of a tracking device. The preliminary low Q^2 result from H1 (H1 SVTX 2000) determined with data from a run period with the interaction vertex shifted by +70 cm is given [60]. Additionally the preliminary result of an ISR analysis of 1997 data by the H1 collaboration is shown [61]. The prediction from the ALLM parameterization [21] and from the fractal fit to low Q^2 data (FRACT) [24] are overlaid.

In order to allow comparison with earlier structure function measurements in DIS and photoproduction, the (scaled) total cross section $\sigma_{tot}^{\gamma^* p}$ as a function of Q^2 for different values of W^2 measured in this analysis is shown in figure 7.16. The data span the transition region between perturbative QCD ($Q^2 > 1.5$ GeV) and the non-perturbative regime of

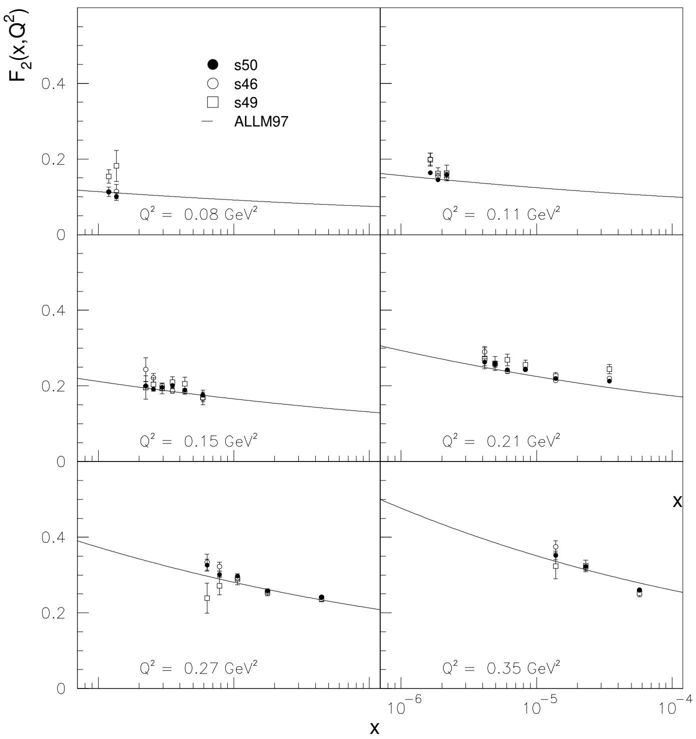

Figure 7.14: *The structure function $F_2(x,Q^2)$ as a function of x for different values of Q^2 measured with the main subtrigger s50 (full circles) in comparison to the measurement based on the inclusive subtriggers s46 (empty circles) and s49 (empty squares) The solid curve shows the parameterization ALLM97 used in the* `PHOJET` *Monte Carlo.*

photoproduction. The new data points are compared to the ZEUS BPT measurement from 1997 [5]. Also shown are the preliminary results of H1 from the shifted vertex run 2000, the preliminary result of H1 from the ISR analysis 1997, the H1 low Q^2 measurement from 96/97 [2] and the measurement of the total photon proton cross section $\sigma_{tot}^{\gamma p} = 165 \pm 11.1\mu$b at $W = 200$ GeV by the H1 collaboration [3]. All data sets are in good agreement both for the low Q^2 domain and the pQCD regime. The theoretical prediction from the ALLM parameterization [21] and from the fractal fit to low Q^2 data [24] are overlaid and both models give a good description of the measurement.

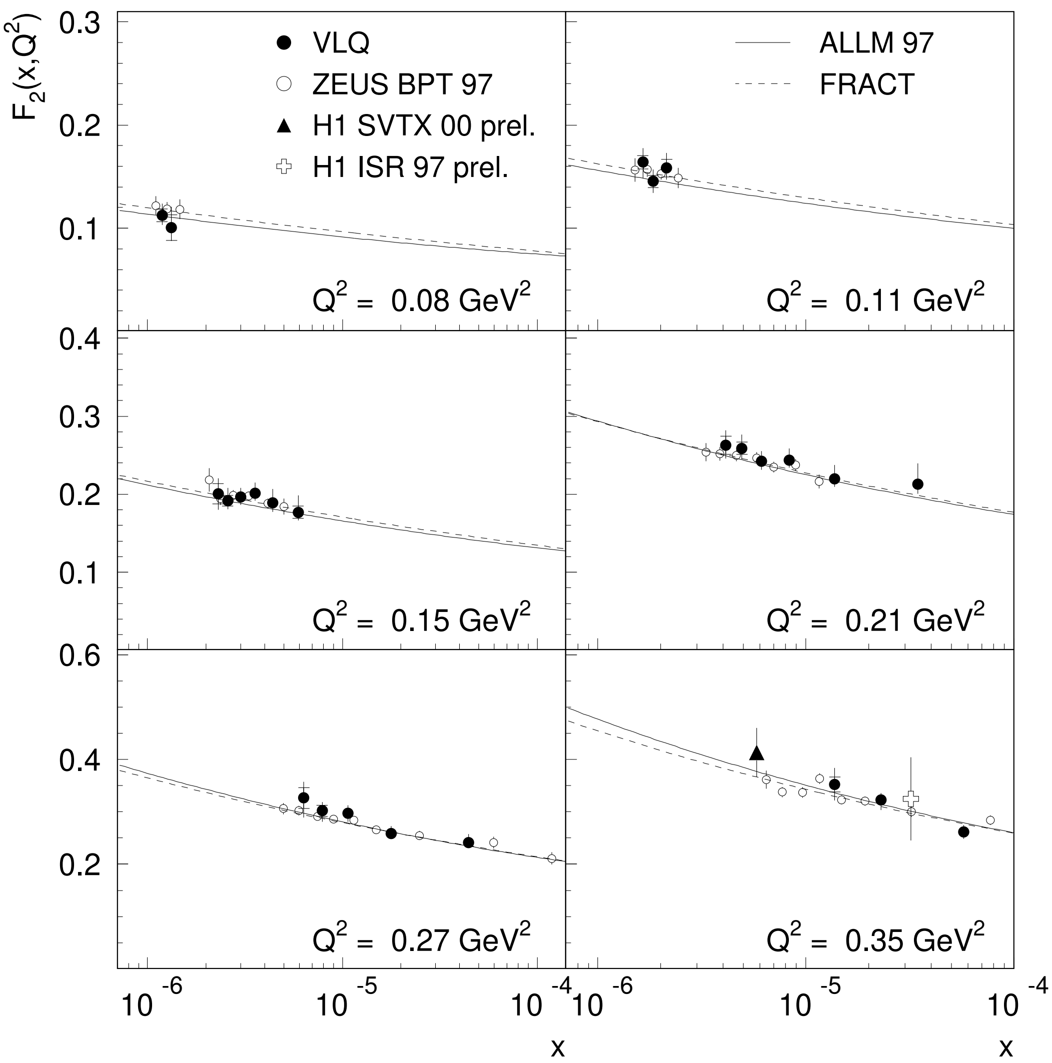

Figure 7.15: *The structure function $F_2(x,Q^2)$ as a function of x for different values of Q^2 (full circles) compared to results from ZEUS BPT 1997 (open circles), H1 shifted vertex 2000 (full triangle) and H1 ISR 97 (open cross). Overlaid are the predictions from ALLM97 (solid line), and the fractal fit (dashed line).*

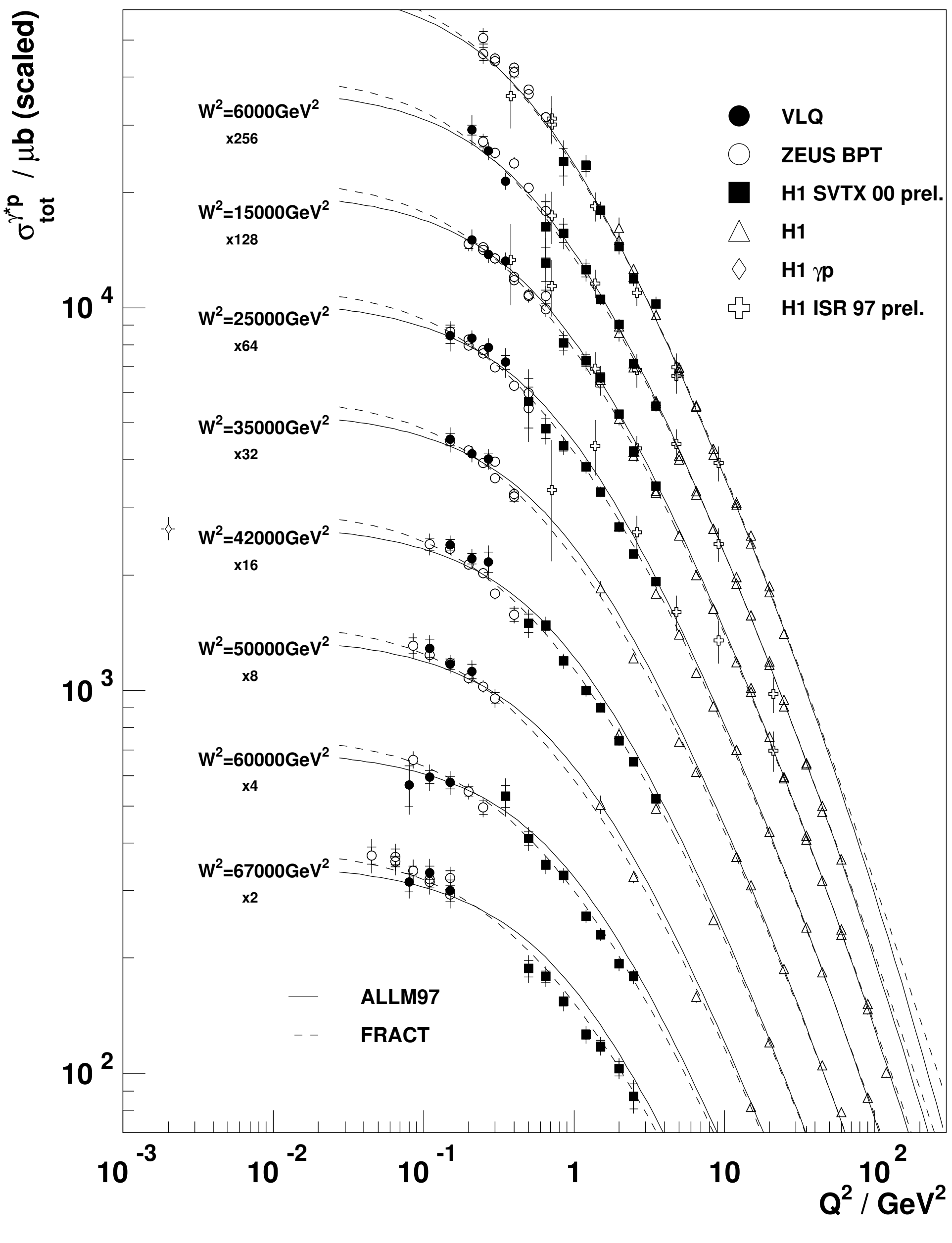

Figure 7.16: *The (scaled) total cross section $\sigma_{tot}^{\gamma^* p}$ as a function of Q^2 for different values of W^2 measured in this analysis (full circles). The results from ZEUS BPT 1997 (open circles), H1 2000 shifted vertex (full squares), H1 ISR 97 (open cross), H1 low Q^2 96/97 (open triangles) and from the total photoproduction cross section measurement (open diamond) are also shown. Overlaid are the predictions from ALLM97 (solid line) and from the fractal fit (dashed line).*

Summary

In this thesis a measurement of the proton structure function $F_2(x,Q^2)$ with the VLQ spectrometer of the H1 experiment in the region of low x and low Q^2 is presented.

In 1998 the insertion of the VLQ spectrometer extended the geometrical acceptance of the H1 experiment in the backward region. The VLQ spectrometer consists of two modules situated above and below the beampipe at approximatively 3m from the nominal interaction point in electron flight direction. Each module contains a silicon tracking device and an energy projection calorimeter mounted on a hydraulic moving mechanism.

Extensive studies on the performance of the VLQ detector components are carried out in this analysis. The VLQ tracker showed a reduced efficiency due to five damaged silicon microstrip detectors. Moreover interferences of the control signals on the Front End electronics prohibited a stable operation of the tracking device in the end of 1999. Hence the information of the VLQ tracker was not used which results in a deteriorated spatial resolution, which restricts the resolution of the kinematic variables in the measurement of the inclusive *ep* cross section.

The calibration procedure of the VLQ calorimeters consists of two steps. A channel-to-channel calibration by which a uniform response of the calorimeter channels is established and a kinematic peak calibration which determines the absolute energy scale of the calorimetric response. The energy resolution of the VLQ calorimeters is found to be 5.5% at 27.5 GeV. The spatial resolution amounts to 0.2 mm. The absolute electromagnetic scale has been cross-checked with a sample of ρ^0 events to an accuracy of 0.5% at the kinematic peak. The linearity of the electromagnetic energy measurement has been verified at medium energies within a level of 1% using Wide Angle Bremsstrahlung events. Furthermore the position of the calorimeter modules relative to the HERA laboratory frame was determined in an alignment procedure based on Wide Angle Bremsstrahlung events to an accuracy of 0.5 mm.

The efficiency of the low threshold VLQ trigger element was determined as a function of the reconstructed energy and of the impact position of the cluster. The efficiency for both modules was found to be above 97% for energies higher than 12 GeV. The efficiency showed a stable behaviour over the whole surface of the calorimeters.

The detector studies and the measurement of the inclusive double differential cross section are based on a large data sample with an integrated luminosity of ≈ 1 pb^{-1} recorded by the H1 experiment at HERA in the end of 1999 at a center-of-mass energy $\sqrt{s} = 318\text{GeV}^2$.

In this thesis the measurement of the proton structure function $F_2(x,Q^2)$ in the region of $0.08\ \mathrm{GeV}^2 < Q^2 < 0.35\ \mathrm{GeV}^2$ and $1.2 \cdot 10^{-6} < x < 5.8 \cdot 10^{-5}$ with the VLQ spectrometer was presented. This result extends the coverage of inclusive cross section measurements by the H1 collaboration to low Q^2 and very low x and spans the transition region between DIS, where perturbative QCD is applicable, and photoproduction. The total uncertainty of the 25 data points is within 5-12% while the statistical uncertainty is below 5%. Hence the precision of the measurement is restricted by the systematic uncertainty of the cross section determination. The main contribution to the systematic uncertainties for most of the bins arises from the restricted spatial resolution of the VLQ calorimeters.

The results presented in this thesis are consistent with previous structure function measurements at larger Q^2. Good agreement within one standard deviation is found with the structure function measurement from the ZEUS collaboration in the kinematic region of overlap at low Q^2. Model predictions by the ALLM collaboration and the fractal fit give a good description of the measured proton structure function F_2.

List of Figures

List of Tables

Bibliography

[1] H1 Collab., C. Adloff et al., Eur. Phys. J. C19 (2001) 269-288.

[2] H1 Collab., C. Adloff et al., Eur. Phys. J. C21 (2001) 33-61.

[3] H1 Collab., S. Aid et al., Z. Phys. C69 (1995) 27.

[4] ZEUS Collaboration, J.Breitweg et al., Phys. Lett. B407 (1997) 432-448.

[5] ZEUS Collaboration, J.Breitweg et al., Phys. Lett. B487 (2000) 53-73.

[6] Th. Gehrmann, talk given at the DESY academic training lectures, Hamburg, October 2001.

[7] Ch. Berger, Elementarteilchenphysik, Springer Verlag, (2001).

[8] C.G. Callan, D.J. Gross, Phys. Rev. Lett. 22 (1969) 23.

[9] CDHS Collaboration, H. Abramowicz et al., Z. Phys. C 17 (1983) 283.

[10] V.N. Gribov and L.N. Lipatov, Sov. J. Nucl. Phys. 15 (1972) 438 and 675;
Yu.L. Dokshitzer, Sov. Phys. JETP 46 (1977) 641.

[11] G. Altarelli and G. Parisi, Nucl. Phys. B 126 (1977) 298.

[12] B. Heinemann, PhD Thesis, University Hamburg, Germany (1999).

[13] T.H. Bauer et al., Rev. Mod. Phys. 50 (1978) 261.

[14] G.A. Schuler, T. Sjöstrand, CERN-TH 7193/94 (1994).

[15] G.A. Schuler, T. Sjöstrand, Phys. Lett. B407 (1993) 539.

[16] T. Sjöstrand, CERN-TH 7112/93 (1993).

[17] A Donnachie and P. V. Landshoff, Total Cross Sections, Phys. Lett. B296 (1992) 227.

[18] P.D.B. Collins, Introduction to Regge Theory and High Energy Physics, Cambridge University Press, (1977).

[19] A Donnachie and P. V. Landshoff, Z Physik C61 (1994) 139.

[20] A Donnachie and P. V. Landshoff, Small x: Two Pomerons!, hep-ph/9806344 (1998).

[21] H. Abramowicz and A. Levy, The ALLM parametrization of $\sigma_{tot}(\gamma^* p)$ an update, hep-ph/9712415 (1997).

[22] A. Capella, A.B. Kaidalov, C. Merino and J. Tran than Van, Phys. Lett. B 337, 358 (1994).

[23] A.B. Kaidalov and C. Merino, Theoretical Description of the HERA Data on F_2 at Low Q^2, hep-ph/9806367 (1998).

[24] T. Laštovička, Self-similar Properties of the Proton Structure at low x, Eur. Phys. J. C, to appear, hep-ph/0203260 (2002).

[25] H1 Collaboration, I. Abt et al., Nucl. Instr. Meth. A386 (1997) 310 and 348.

[26] H1 Collaboration, Technical Proposal to build a Special Spectrometer covering Very Small Momentum Transfers, (1996).

[27] A. Stellberger, Entwicklung und Bau eines kompakten elektromagnetischen Kalorimeters, Ph. D. Thesis, Heidelberg, Germany (1998).

[28] O. Nix, Suche nach odderoninduzierten Beiträgen in exklusiver π^0-Produktion mit dem Detektor H1 bei HERA, Ph.D. Thesis, Heidelberg, Germany (2001) HD-KIP-01-05.

[29] C. Krauss, Untersuchungen an einem Halbleiterdetektor für das H1 Experiment, Diploma Thesis, RWTH Aachen, Germany (1998).

[30] R. Horisberger, D. Pitzl, A novel readout chip for silicon strip detectors with analog pipeline and digitally controlled analog signal processing, Nucl. Instr. and Meth., A326 (1993) 92-88.

[31] J. Bürger et al., Online Readout and Control Unit for High-speed / High Resolution Readout of Silicon Tracking Detectors, DESY 96-200 (1996).

[32] S. Prell, Entwicklung des Steuer- und Auslesemoduls für die Siliziumstreifendetektoren des H1-Detektors, Ph. D. Thesis, Hamburg, Germany (1996).

[33] G. Noyes, P. Burch, RAL-PC3050 RIO2 FADC PMC, RAL Technology (1997).

[34] C. Duprel, Untersuchungen an Halbleiterstreifendetektoren für das VLQ-Spektrometer im Rahmen des H1-Experimentes mit einem Diodenlaser, Diploma Thesis, RWTH Aachen, Germany (1998) PITHA 98/39.

[35] P.-O. Meyer, Messung der Strukturfunktion F_2 bei kleinen Bjorken-x und kleinen Impulsüberträgen mit dem VLQ-Spektrometer des H1 Detektors, Ph.D. Thesis, RWTH Aachen, Germany (2000) PITHA 00/27.

[36] S. Hurling, Der VLQ-Detektor bei H1: Inbetriebnahme, Spurrekonstruktion und Messung der elastisch diffraktiven J/ψ-Produktion bei kleinen Q^2, Ph.D. Thesis, Hamburg, Germany (2000).

[37] S. Bentvelsen, J. Engelen and P. Kooijman, proceedings of the Workshop Physics at HERA, vol. 1, DESY, Hamburg, Germany (1991) 23.

[38] F. Jacquet and A. Blondel, proceedings of the study of an *ep* facility for Europe 97/48, ed. U. Amaldi, DESY, Hamburg (1979) 391.

[39] R. Engel, Z. Phys. C 66 (1995) 203; R. Engel and J. Ranft, Phys. Rev. D 54 (1996) 4244.

[40] M. Wessels, Untersuchungen zur Elektron-Proton-Streuung mit Hilfe des VLQ-Spektrometers, Diploma Thesis, RWTH Aachen, Germany (2000).

[41] T. Sjöstrand, Phys. Lett. B 157 (1985) 321.

[42] T. Gottschalk, Nucl. Phys. B277 (1986) 700.

[43] B. Andersson et al., Phys. Rep. 97 (1983) 31.

[44] T. Sjöstrand, Comp. Phys. Comm. 39 (1986) 347;
T. Sjöstrand and M. Bengtsson, ibid. 43 (1987) 367.

[45] L. Lönnblad, Comp. Phys. Comm. 71 (1992) 15.

[46] A. Kwiatkowski, H. Spiesberger and H.-J. Möhring, Comp. Phys. Comm. 69 (1992) 155.

[47] G. Ingelman, A. Edin and J. Rathsman, Comp. Phys. Comm. 101 (1997) 108.

[48] A. Courau et al., Quasi-Real QED Compton Monte Carlo for HERA, Internal Note H1-01/92-207, (1992).

[49] Th. Kluge, Untersuchung des QED-Bremsstrahlungsprozesses bei kleinen Impulsüberträgen mit dem H1-Detektor bei HERA, Diploma Thesis, RWTH Aachen, Germany (2000) PITHA 00/08.

[50] CERN, GEANT, detector description an simulation tool, CERN Program Library Long Writeup W 5013 (1994).

[51] K. Sedlak et al., Simulation of the VLQ detector, Internal Note H1-03/00-581, (2000).

[52] M. Rudowicz, Ph. D. Thesis, Hamburg, MPI-PhE/92-14(1992).

[53] S. Peters, Ph. D. Thesis, Hamburg, MPI-PhE/92-13(1992).

[54] H1 Collaboration, C. Adloff et al., DESY 99-010, Hamburg, Germany (1999), subm. to Eur. Phys. J. C.

[55] F. James and M. Roos, Comp. Phys. Comm. 10 (1975) 343.

[56] S. Levonian, A. Panitch, H1 Internal Note H1-09/95-454, (1995).

[57] Hanspeter Beck, Principles and Operation of the z-Vertex Trigger, Internal Note H1-05/96-479 (1996).

[58] B. Badelek et al., Z. Phys. C74 (1997) 297.

[59] A. Arbuzov et al., HECTOR 1.00, hep-ph/9511434 (1995).

[60] H1 Collaboration, preliminary result presented by T. Laštovička at the 10th International Workshop on Deep Inelastic Scattering DIS 2002, to appear in Acta Phys. Polonica B.

[61] H1 Collaboration, preliminary result presented by C. Issever at the 9th International Workshop on Deep Inelastic Scattering DIS 2001.

Acknowledgments

First of all I would like to thank Prof. Dr. Günter Flügge for the support and the opportunity to work on my Ph.D. during all the years at the III Physikalische Institut of the RWTH Aachen. I wish also to thank Prof. Dr. Christoph Berger for his guidance throughout the analysis.

I want to thank Dr. Herbert Gräßler whose support and advice were very helpful to me.

I am thankful to the whole H1 collaboration for the enthusiastic environment as well as the technical and scientific support. Especially i wish to thank all the people involved in the construction and commissioning of the VLQ spectrometer such as Dr. Peer-Oliver Meyer, Thomas Kluge and Dr. Carsten Krauss. Linus Lindfeld and Martin Wessels were great collaborators who contributed to the success of this analysis.

Furthermore i would like to thank the members of the ELAN working group for their help and stimulating discussions.

My room mates Lars Finke, Thomas Kluge, Linus Lindfeld, Dr. Peer-Oliver Meyer, Martin Wessels, Dr. Markus Wobisch and Anja Vest made my years in Hamburg a wonderful experience. Special thanks to all who participated in the proofreading of this thesis.

I am grateful to my family for their loving care and support throughout my life.

Lebenslauf von Carlo Duprel

Geburtstag und -ort:	08.06.1974 in Luxemburg
Nationalität:	Luxemburger
September 1980 - Juli 1981	Besuch der Grundschule Centre Gloden Hostert
September 1981 - Juli 1986	Besuch der Grundschule Centre Scolaire “Am Sand”
September 1986 - Juli 1993	Besuch des Gymnasiums Lycée Robert Schuman Luxembourg
Juli 1993	Abitur
Oktober 1993 - Oktober 1995	Grundstudium Physik an der RWTH Aachen
02.10.1995	Ablegen der Vordiplomprüfung in Physik
November 1995 - September 1998	Hauptstudium Physik an der RWTH Aachen
Juli 1997 - August 1998	Erstellung einer Diplomarbeit am III. Physikalischen Institut B der RWTH Aachen bei Prof. Dr. G. Flügge im Rahmen der H1 Kollaboration mit dem Titel: “Untersuchungen an Halbleiterstreifendetektoren für das VLQ-Spektrometer im Rahmen des H1-Experimentes mit einem Diodenlaser”, PITHA-98/39
7.9.1998	Ablegung der Diplomprüfung in Physik
1.3.1999	Beginn der Promotionsarbeit am III. Physikalischen Institut B der RWTH Aachen bei Prof. Dr. G. Flügge
17.12.2002	Abgabe dieser Arbeit
7.3.2003	Ablegung der mündlichen Prüfung und Abschluss der Promotion